

1-1-2017

Azimuthally-Differential Pion Femtoscopy Relative To The Second And Third Harmonic In Pb-Pb Collisions

Mohammad Saleh
Wayne State University,

Follow this and additional works at: https://digitalcommons.wayne.edu/oa_dissertations

 Part of the [Elementary Particles and Fields and String Theory Commons](#), and the [Nuclear Commons](#)

Recommended Citation

Saleh, Mohammad, "Azimuthally-Differential Pion Femtoscopy Relative To The Second And Third Harmonic In Pb-Pb Collisions" (2017). *Wayne State University Dissertations*. 1868.
https://digitalcommons.wayne.edu/oa_dissertations/1868

This Open Access Dissertation is brought to you for free and open access by DigitalCommons@WayneState. It has been accepted for inclusion in Wayne State University Dissertations by an authorized administrator of DigitalCommons@WayneState.

**AZIMUTHALLY-DIFFERENTIAL PION FEMTOSCOPY RELATIVE
TO THE SECOND AND THIRD HARMONICS IN Pb–Pb COLLISIONS**

by

MOHAMMAD SALEH

DISSERTATION

Submitted to the Graduate School

of Wayne State University,

Detroit, Michigan

in partial fulfillment of the requirements

for the degree of

DOCTOR OF PHILOSOPHY

2017

MAJOR: Physics

Approved By:

Advisor

DEDICATION

Every challenging and hard work need self efforts as well as guidance of olders especially those who were very close to our heart. I would like to dedicate my thesis to my beloved parents. The reason of what I became today.

ACKNOWLEDGMENTS

I consider myself fortunate to have had the opportunity to pursue research work toward my Ph.D. with Professor Sergei Voloshin. Without his continuous optimism, enthusiasm, encouragement, and support this research would have not been completed. His scientific approach and experience have helped to great extent to accomplish this task. I would like to thank my Ph.D. committee: Professor Claude Prunea, Professor Sean Gavin, and Professor Wen Li for all the support through my Ph.D. research.

I would like to thank my parents, siblings, wife, and daughter who have been supportive in every way possible, and who have shown the patience over the years this thesis has taken. Their constant support and encouragement has made me push myself in every way possible. For me it is a proud privilege and a matter of honor to offer my overwhelming gratitude to them.

“All truths are easy to understand once they are discovered; the point is to discover them.”

— Galileo Galilei

TABLE OF CONTENTS

Dedication	ii
Acknowledgments	iii
List of Figures	vii
Chapter 1 Introduction	1
1.0.1 Early Universe	1
1.0.2 Quantum Chromodynamics	1
1.0.3 Heavy Ion Collisions	3
1.0.4 Femtoscopy of nuclear collisions	6
Chapter 2 Experimental Setup	9
2.1 Large Hadron Collider	9
2.2 A Large Ion Collider Experiment (ALICE)	10
2.2.1 ALICE Detectors	10
2.2.1.1 The Time-Projection Chamber (TPC)	11
2.2.1.2 The Inner Tracking System (ITS)	13
2.2.1.3 The Time-Of-Flight Detector (TOF)	13
2.2.1.4 V0 Detector	14
2.2.1.5 Other Detectors	14
2.2.1.6 Detectors Upgrade	16
2.2.2 ALICE Software	17
2.2.2.1 ROOT	17
2.2.2.2 AliRoot and AliPhysics	17
2.2.2.3 AliFemto	17
Chapter 3 HBT	18
3.1 Hanbury Brown-Twiss (HBT) Interferometry	18
3.1.1 Theoretical Formalism	18
3.1.2 Coordinate System	20

3.1.3	Gaussian Parameterization	21
3.1.4	Final state interactions	23
3.2	Experimental Techniques	25
3.2.1	Experimental Correlation Function	25
3.2.2	Log-Likelihood Fitting	25
Chapter 4	Azimuthally-differential HBT	26
4.1	Anisotropic Flow	27
4.1.1	Event Plane Method	28
4.2	Data Analysis	31
4.2.1	Data Sample	31
4.2.2	Centrality flattening	33
4.2.3	Analysis Software	33
4.2.4	Filter Bits, Event Cuts, and Track Cuts	33
4.2.5	Pair Cuts Studies	36
4.2.5.1	Two-Track Studies	36
4.3	Azimuthal HBT Results w.r.t second harmonic	46
4.3.1	Pb-Pb 2.76 TeV Results	46
4.3.1.1	Radii Oscillation	46
4.3.1.2	HBT radii vs. Azimuthal Angle	47
4.3.1.3	Average Radii and Amplitudes of Oscillations	50
4.3.1.4	Comparison with the Non-azimuthally Results	53
4.3.1.5	Final Source Eccentricity	54
4.3.2	Pb-Pb 5.02 TeV Results	56
4.3.2.1	Average Radii Comparison between 2.76 TeV and 5.02 TeV	56
4.3.2.2	Amplitudes of Oscillations for Pb-Pb 5.02 TeV	58
4.3.3	Corrections	60
4.3.3.1	Coulomb Correction	60

4.3.3.2	Event Plane Resolution Correction	62
4.3.4	Systematic Uncertainty	65
4.3.4.1	q-fit Range	65
4.4	Azimuthal HBT for Third Harmonic Event Plane	69
4.4.1	Overview	69
4.4.2	Event Plane	69
4.4.2.1	Binning	69
4.4.3	Results	70
4.4.3.1	Centrality dependence	70
4.4.3.2	k_T dependence	71
4.4.3.3	Average Radii	71
4.4.4	Amplitudes of Oscillations	71
4.4.5	Final Source Shape from Blast-Wave Model	75
4.4.6	Systematic Studies	78
4.4.6.1	\vec{B} orientation	78
4.4.6.2	Charge	79
4.4.6.3	Fit range	79
4.4.6.4	Event plane	81
4.4.6.5	Systematics table	81
4.5	Event Shape Engineering	85
4.5.1	Effect of q_2 (q_3) selection on v_2 (v_3)	85
4.5.2	Relative Amplitude of HBT radii with Event Shape Engineering	85
Chapter 5 Conclusion		89
Bibliography		90
Abstract		97
Autobiographical Statement		99

LIST OF FIGURES

Figure 1.1: A time line for the Big Bang.....	2
Figure 1.2: The collision of two nuclei leave behind a medium of high energy density. After about 10^{-23} s, the medium thermalizes to a deconfined state of quarks and gluons. The medium cools down and hadronize into pions, kaons, and many other particles. These hadronized particles scatter off each other for a few more fm/ c , until the medium become so dilute that they free-stream to the experimental detectors.....	3
Figure 1.3: The QCD phase diagram.....	4
Figure 1.4: Space-time evolution of a heavy ion collision that undergoes a phase transition from hadrons to a QGP.....	5
Figure 2.1: A schematic view of the Large Hadron Collider [14]. Proton and/or Pb ion beams go through a series of accelerators before being injected into the collider. Beams travel in both directions, clockwise and counterclockwise, around the LHC, and the two beams are only allowed to collide at the four main detectors: ALICE, ATLAS, LHC-b, and CMS.....	10
Figure 2.2: Schematic view of the ALICE detector.....	11
Figure 2.3: Layout of the The Time Projection Chamber layout. Figure from [1].....	12
Figure 2.4: An example of a Pb-Pb collision measured at the ALICE detector.....	13
Figure 2.5: Layout of the Inner Tracking System. Figure from [2].....	14
Figure 2.6: Schematic view of the V0 detector. Figure from [3].....	15
Figure 3.1: LCMS frame	21
Figure 3.2: $R_{out}, R_{side}, R_{long}$ of the homogeneity region. Figure taken from [4].....	23
Figure 4.1: Schematic of the collision zone between two incoming nuclei where x-z plane is the reaction plane.....	27
Figure 4.2: Schematic of the directed and elliptic flow.....	28
Figure 4.3: Cartoon representation of the collision centrality percentile.....	33
Figure 4.4: Cartoon illustration of $\Delta\phi^*$	36
Figure 4.5: DCA_{xy} distribution	37
Figure 4.6: DCA_z distribution. Figure from [5].....	38
Figure 4.7: $DCA_{xy} < 0.2$ cm, $DCA_z < 0.15$ cm: Two dim. ratio $\Delta\eta\Delta\phi^*$ for k_T range 0.2-0.5 GeV/ c . Figure from [5].....	39
Figure 4.8: $DCA_{xy} < 0.2$ cm, $DCA_z < 0.15$ cm: Two dim. ratio $\Delta\eta\Delta\phi^*$ for k_T range 0.5-1.0 GeV/ c	39

Figure 4.9: $DCA_{xy} < 0.2$ cm, $DCA_z < 0.15$ cm: $\Delta\phi^*$ projection for k_T range 0.2-0.5 GeV/c	39
Figure 4.10: $DCA_{xy} < 0.2$ cm, $DCA_z < 0.15$ cm: $\Delta\varphi^*$ projection for k_T range 0.5-1.0 GeV/c. Figure from [5]	39
Figure 4.11: $DCA_{xy} < 0.2$ cm, $DCA_z < 0.15$ cm: $\Delta\eta$ projection for k_T range 0.2-0.5 GeV/c. Figure from [5]	40
Figure 4.12: $DCA_{xy} < 0.2$ cm, $DCA_z < 0.15$ cm: $\Delta\eta$ projection for k_T range 0.5-1.0 GeV/c. Figure from [5]	40
Figure 4.13: $DCA_{xy} < 0.4$ cm, $DCA_z < 0.3$ cm: Two dim. ratio $\Delta\eta\Delta\phi^*$ for k_T range 0.2-0.5 GeV/c. Figure from [5]	40
Figure 4.14: $DCA_{xy} < 0.4$ cm, $DCA_z < 0.3$ cm: Two dim. ratio $\Delta\eta\Delta\phi^*$ for k_T range 0.5-1.0 GeV/c. Figure from [5]	40
Figure 4.15: $DCA_{xy} < 0.4$ cm, $DCA_z < 0.3$ cm: $\Delta\phi^*$ projection for k_T range 0.2-0.5 GeV/c. Figure from [5]	41
Figure 4.16: $DCA_{xy} < 0.4$ cm, $DCA_z < 0.3$ cm: $\Delta\phi^*$ projection for k_T range 0.5-1.0 GeV/c. Figure from [5]	41
Figure 4.17: $DCA_{xy} < 0.4$ cm, $DCA_z < 0.3$ cm: $\Delta\eta$ projection for k_T range 0.2-0.5 GeV/c. Figure from [5]	41
Figure 4.18: $DCA_{xy} < 0.4$ cm, $DCA_z < 0.3$ cm: $\Delta\eta$ projection for k_T range 0.5-1.0 GeV/c. Figure from [5]	41
Figure 4.19: $DCA_{xy} < 2.4$ cm, $DCA_z < 3.0$ cm: Two dim. ratio $\Delta\eta\Delta\phi^*$ for k_T range 0.2-0.5 GeV/c. Figure from [5]	42
Figure 4.20: $DCA_{xy} < 2.4$ cm, $DCA_z < 3.0$ cm: Two dim. ratio $\Delta\eta\Delta\phi^*$ for k_T range 0.5-1.0 GeV/c. Figure from [5]	42
Figure 4.21: $DCA_{xy} < 2.4$ cm, $DCA_z < 3.0$ cm: $\Delta\phi^*$ projection for k_T range 0.2-0.5 GeV/c. Figure from [5]	42
Figure 4.22: $DCA_{xy} < 2.4$ cm, $DCA_z < 3.0$ cm: $\Delta\phi^*$ projection for k_T range 0.5-1.0 GeV/c. Figure from [5]	42
Figure 4.23: $DCA_{xy} < 2.4$ cm, $DCA_z < 3.0$ cm: $\Delta\eta$ projection for k_T range 0.2-0.5 GeV/c. Figure from [5]	43
Figure 4.24: $DCA_{xy} < 2.4$ cm, $DCA_z < 3.0$ cm: $\Delta\eta$ projection for k_T range 0.5-1.0 GeV/c. Figure from [5]	43
Figure 4.25: $DCA_{xy} < 0.2$ cm, $DCA_z < 0.15$ cm: $C(q_{inv})$ for k_T range 0.2-0.5 GeV/c. Figure from [5]	44
Figure 4.26: $DCA_{xy} < 0.2$ cm, $DCA_z < 0.15$ cm: $C(q_{inv})$ for k_T range 0.5-1.0 GeV/c. Figure from [5]	44

Figure 4.27: $DCA_{xy} < 0.4$ cm, $DCA_z < 0.3$ cm: $C(q_{inv})$ for k_T range 0.2-0.5 GeV/ c . Figure from [5]	44
Figure 4.28: $DCA_{xy} < 0.4$ cm, $DCA_z < 0.3$ cm: $C(q_{inv})$ for k_T range 0.5-1.0 GeV/ c . Figure from [5]	44
Figure 4.29: $DCA_{xy} < 2.4$ cm, $DCA_z < 3.0$ cm: $C(q_{inv})$ for k_T range 0.2-0.5 GeV/ c . Figure from [5]	45
Figure 4.30: $DCA_{xy} < 2.4$ cm, $DCA_z < 3.0$ cm: $C(q_{inv})$ for k_T range 0.5-1.0 GeV/ c . Figure from [5]	45
Figure 4.31: Centrality dependence of radii vs. pair emission angle at k_T range of 0.3-0.4 GeV/ c	48
Figure 4.32: The azimuthal dependence of R_{out}^2 , R_{side}^2 , R_{long}^2 , R_{os}^2 , and λ as a function of $\Delta\varphi = \varphi_{pair} - \Psi_{EP,2}$	49
Figure 4.33: The average radii $R_{out,0}^2$, $R_{side,0}^2$, $R_{long,0}^2$, and $R_{os,0}^2$ as a function of central- ity for different k_T ranges compared to hydrodynamical calculations [6]. Square brackets indicate the systematic errors.....	51
Figure 4.34: Amplitudes of the relative radius oscillations versus centrality for the k_T ranges 0.2–0.3, 0.3–0.4, 0.4–0.5, and 0.5–0.7 GeV/ c . The error bars indicate the statistical uncertainties and the square brackets show the sys- tematic errors.	52
Figure 4.35: Centrality and k_T dependence of R_{out} , R_{side} and R_{long} for azimuthally- differential and non-azimuthal pion femtoscopy in Pb-Pb collisions at 2.76 TeV vs non-azimuthal HBT analysis [7]. Points are shifted slightly in the x-direction for visibility. Closed symbols show the azimuthally-differential HBT results and open symbols show the non-azimuthal results. The square brackets and error bars are systematic errors.....	53
Figure 4.36: An estimate of freeze-out eccentricity $2R_{side,2}^2/R_{side,0}^2$ for different k_T ranges vs. initial state eccentricity from Monte Carlo Glauber model [8] for six centrality ranges, 0–5%, 5–10%, 10–20%, 20–30 %, 30–40 %, and 40–50%. The dashed line indicates $\varepsilon_{final} = \varepsilon_{init}$. Square brackets indicate systematic errors.....	55
Figure 4.37: Comparison between the average radii from two different energies. The open markers are for 2.76 TeV energy, whereas the closed symbol are for 5.02 TeV energy.	57
Figure 4.38: Amplitudes of the relative radius oscillations versus centrality for the k_T ranges 0.2–0.3, 0.3–0.4, 0.4–0.5, and 0.5–0.7 GeV/ c . The error bars indicate the statistical uncertainties.....	59
Figure 4.39: Squared Coulomb wave function integrated over a source of centrality class 0-5%.	61

Figure 4.40: Event plane resolution using the TPC dependence on centrality.	63
Figure 4.41: HBT radii of charged pions as a function of azimuthal pair angle. Comparison before and after the event plane resolution correction.	64
Figure 4.42: STAR bin-by-bin event plane resolution correction [9].	67
Figure 4.43: TPC third harmonic event plane resolution using two-subevent method ...	70
Figure 4.44: HBT radii oscillations in one k_T range $0.2 < k_T < 0.3$ for six centrality ranges.	71
Figure 4.45: HBT radii oscillations for one centrality range in four k_T ranges.	72
Figure 4.46: Average radii R_0^2 for four k_T ranges: $0.2 < k_T < 0.3$ GeV/ c (black markers), $0.3 < k_T < 0.4$ GeV/ c (red markers), $0.4 < k_T < 0.5$ GeV/ c (blue markers), $0.5 < k_T < 0.7$ GeV/ c (magenta markers). Closed symbols for third harmonic event plane results while the open symbols are for second harmonic event plane results.	73
Figure 4.47: The amplitudes of radii oscillations $R_{out,3}^2$, $R_{side,3}^2$, $R_{long,3}^2$, and $R_{os,3}^2$ versus centrality for four k_T ranges. Square brackets indicate systematic errors. ..	74
Figure 4.48: The relative amplitudes of the radius oscillations $R_{out,3}^2/R_{out,0}^2$, and $R_{side,3}^2/R_{side,0}^2$ dependence on third-order anisotropies in space (a_3) and transverse flow (ρ_3) for the centrality range 5–10% and $k_T = 0.6$ GeV from the Blast-Wave model [10]. The dashed lines are the ALICE data.	76
Figure 4.49: The predicted final source anisotropy a_3 and transverse flow (ρ_3) for different centrality ranges using the Blast-Wave model [10].	77
Figure 4.50: Systematic study for different field orientation data set. The green box represents the systematic percentage on the radii oscillation parameter while the magenta box represents the systematic percentage on the average radii parameter. Those results are for centrality class 0–5% and k_T range $0.2 < k_T < 0.3$ GeV/ c	78
Figure 4.51: Systematic study for different pion pair charges. The green box represents the systematic percentage on the radii oscillation parameter while the magenta box represents the systematic percentage on the average radii parameter.	79
Figure 4.52: Systematic study for different fit ranges. The green box represents the systematic percentage on the radii oscillation parameter while the magenta box represents the systematic percentage on the average radii parameter. ...	80
Figure 4.53: Centrality dependence of v_2 ratio.	86
Figure 4.54: Centrality dependence of v_3 ratio.	87

Figure 4.55: Amplitudes of the relative radius oscillations versus centrality with and without large q_2 (q_3) selection..... 88

CHAPTER 1 INTRODUCTION

1.0.1 Early Universe

According to the Big Bang theory, the Big Bang occurred about 13.8 billion years ago. The theory states that initially the universe was in a very high density state and then expanded. During the first few microseconds of the initial expansion, the universe was so dense that hadrons could not exist. The matter then existed in the form of deconfined quarks, antiquarks, and gluons were deconfined in a thermalized state known as **quark-gluon plasma** (QGP). As the universe expanded, it becomes less dense and cools. By the first second, the universe was made up of fundamental particles: quarks, electrons, photons and neutrinos. When the temperature dropped below 170 MeV, the first hadron formed. After three seconds, protons and neutrons came together to form the nuclei of simple elements: hydrogen, helium and lithium. After 300,000 years, electrons and atomic nuclei were able to combine to form neutral atoms, where the universe temperature was about 3000 K. After several million years, the chemical composition of the universe started to change again. Giant clouds of the produced elements merged through gravity to form stars and galaxies and heavier elements were produced within stars or supernovae, see Fig.1.1.

1.0.2 Quantum Chromodynamics

Quantum Chromodynamics (QCD) is the theory of the strong interaction between quarks and gluons. Quarks are never seen in isolation, but only in confined state forming hadrons, which are either baryons (formed by three quarks) or mesons (formed by a quark-antiquark pair). The strong force is carried by gluons, just as the photon that carries the electromagnetic force. However, whereas photons carry no electric charge, gluons carry color charge so they can interact between each other. QCD predicts that at relatively high density and temperature it is possible to have free quarks and gluons, and their collective behavior exhibits fluidlike properties [11]. This state is called the Quark Gluon Plasma (QGP) [12], and is believed to be the one in which the early universe existed in a time-scale $\sim 10^{-5}$ s right after the Big Bang.

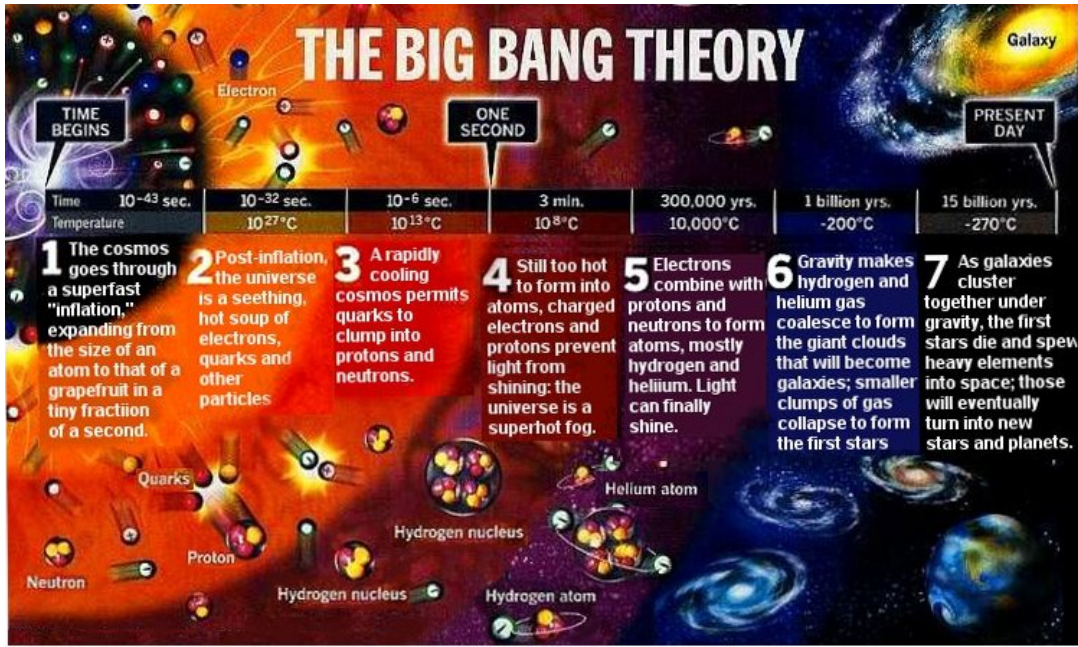


Figure 1.1: A time line for the Big Bang.

High energy heavy ion and proton-proton collisions are the tool to study matter at extreme high temperatures and low baryon density, and determine its properties on different regions of the phase diagram of nuclear matter (also referred to as the QCD phase diagram because Quantum Chromo-Dynamics describes the interactions among nucleons). Figure 1.3 shows the QCD phase diagram. At a very low temperature and chemical potential, or baryon density, the state of matter is simply vacuum. Above $\mu \sim 922$ MeV there is nuclear matter. As baryon density increases matter will be eventually in a super fluidlike and superconducting phase, that what is believed to be found in neutron stars. To reach a relatively high temperatures, we collide two beams of particles traveling in opposite directions, or by colliding a beam of particles with a fixed target. When nuclear matter is heated by collision, it can reach a hadronic uid phase and for higher energies the quark gluon plasma (QGP) phase, where quarks and gluons are not bound together and the chiral symmetry is restored. Results from RHIC experiments [13] and from lattice models [14] calculations estimate the critical point at a temperature of $T \sim 170$ MeV. Increasing the collision energy allows to follow different paths along the diagram: SPS energies get close to the phase transition and

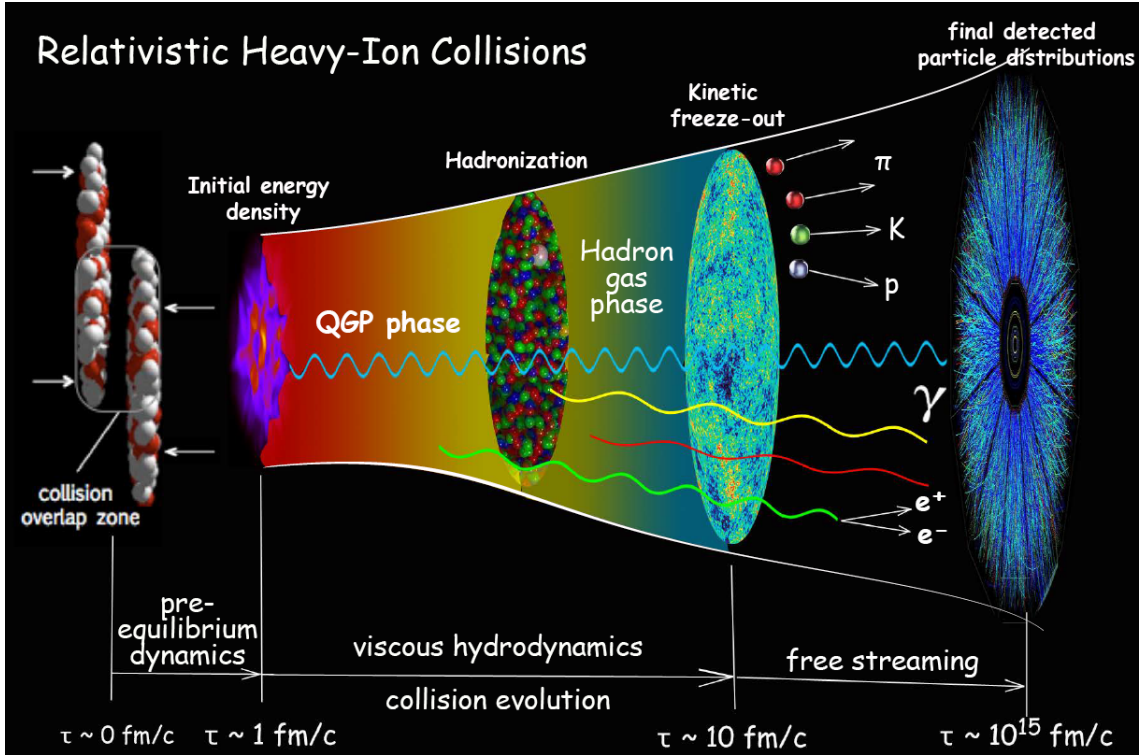


Figure 1.2: The collision of two nuclei leave behind a medium of high energy density. After about 10^{-23} s, the medium thermalizes to a deconfined state of quarks and gluons. The medium cools down and hadronize into pions, kaons, and many other particles. These hadronized particles scatter off each other for a few more fm/c, until the medium become so dilute that they free-stream to the experimental detectors.

RHIC energies are relatively large enough to make a phase transition. It is still not finalized if it is a first order phase transition with an associated latent heat, or a second order phase transition with a smooth cross over. LHC energies are believed to allow for a second order phase transition into the QGP phase.

1.0.3 Heavy Ion Collisions

The different stages of the collision of two heavy ions at sufficient high energy to create a state of deconfined quarks and gluons is shown in Fig. 1.4. After the two nuclei collide, there is a pre-equilibrium stage in which each nucleon scatters several times and partons (quarks and gluons) are liberated. At some point these quarks and gluons thermalize by re-scattering, resulting in a thermalized QGP. The system expands and cools down to temperatures around T_c , reaching hadronization temperature in which hadrons are

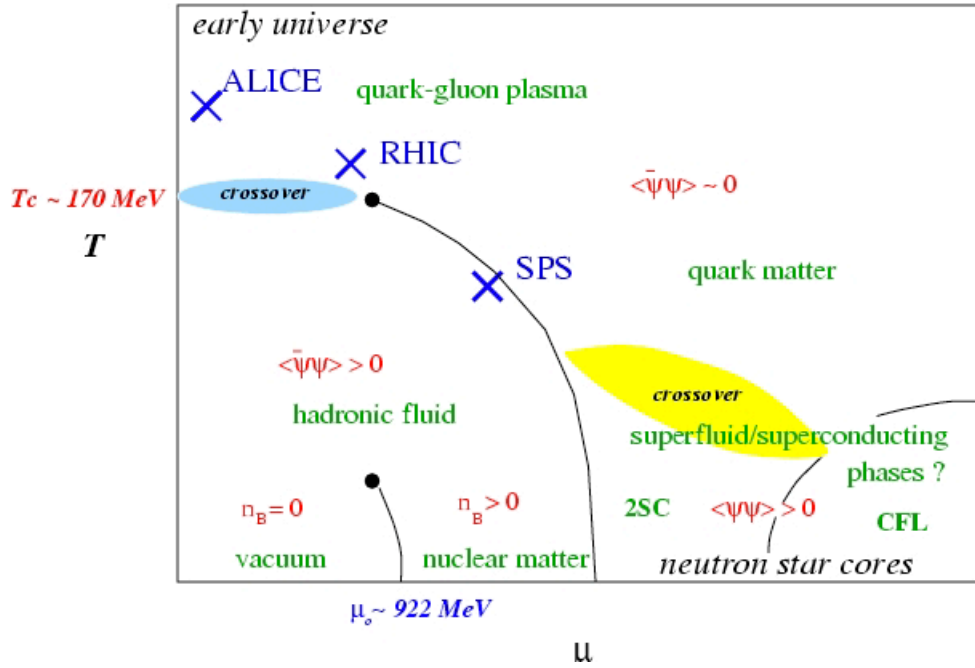


Figure 1.3: The QCD phase diagram.

formed from the free quarks and gluons. The hadrons then interact inelastically until the system reaches chemical freeze out and no more inelastic interactions occur. At that point there is not enough energy to change the different species, however these hadrons are still interacting elastically. Eventually, the system is diluted enough that the interaction between hadrons stops, at this point the system undergoes a chemical freeze-out and hadrons

fly off to the detectors. The first heavy ion collisions conducted at relativistic conditions

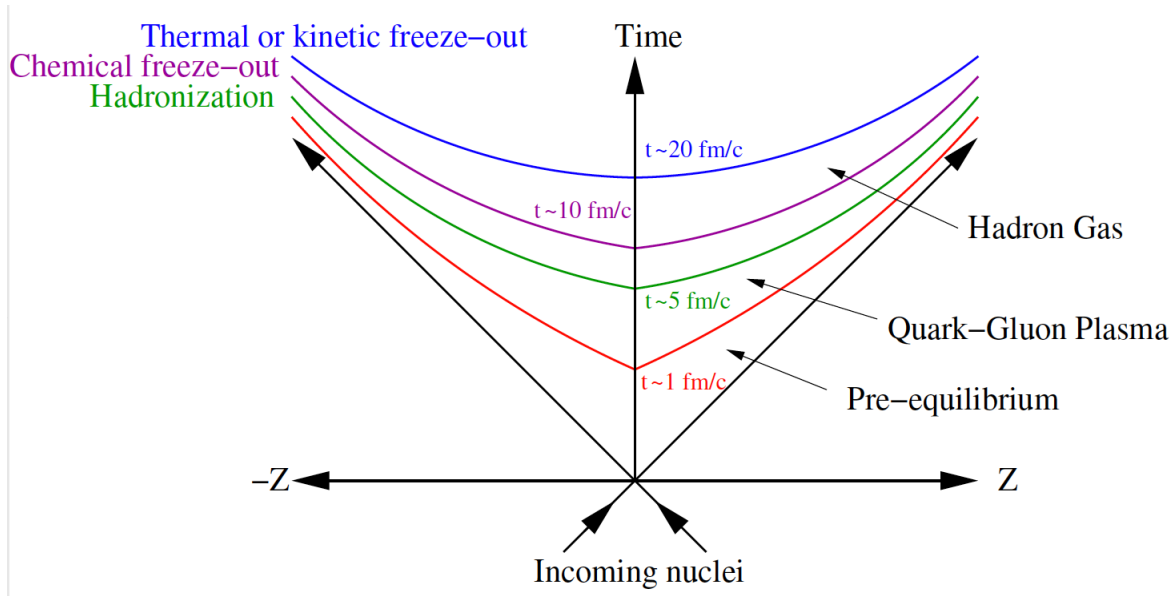


Figure 1.4: Space-time evolution of a heavy ion collision that undergoes a phase transition from hadrons to a QGP.

were undertaken at Bevalac, Lawrence Berkeley National laboratory (LBNL), at $\sqrt{s_{\text{NN}}} = 1$ GeV/nucleon [15]. From 1986 to 1995 Brookhaven National Laboratory (BNL) conducted experiments using Alternating Gradient Synchrotron (AGS). It accelerated silicon ions up to $\sqrt{s_{\text{NN}}} = 5$ GeV/nucleon and gold ions up to $\sqrt{s_{\text{NN}}} = 4$ GeV/nucleon. In Europe, the Super Proton Synchrotron (SPS, CERN) produced a $\sqrt{s_{\text{NN}}} = 10$ GeV/nucleon beam of oxygen and then increased the energy to $\sqrt{s_{\text{NN}}} = 19$ GeV/nucleon and accelerated different nuclei as heavy as lead. Nowadays, at Brookhaven National Laboratory (BNL), two experiments STAR and PHENIX use the Relativistic Heavy Ion Collider (RHIC) beam. RHIC accelerates gold nuclei at $\sqrt{s_{\text{NN}}} = 200$ GeV/c. In 2010, Pb-Pb collisions at $\sqrt{s_{\text{NN}}} = 2.76$ TeV marked the start of the Large Hadron Collider (LHC) Heavy-Ion program by the ALICE experiment. Questions of interest include: “When does hadronization occur (lifetime)?”, “What is the equation of state that describe the evolution of the interaction?”, “What is the size and shape of the medium at kinetic freezeout?”. A number of models have been developed to probe these questions and many others [16–18]. Where experimental results

are helping refine these models.

1.0.4 Femtoscopy of nuclear collisions

HBT interferometry is a measurement technique widely used in particle physics since Goldhaber, Goldhaber, Lee and Pais first used it in 1967 at the Bevatron to measure the radii of particle emission sources in proton-antiproton collisions. Light was used in the original measurements of stellar sizes but in heavy ions, one uses hadrons. Over the years, this method became a precise tool for measuring the space-time extension of particle source at freeze-out (homogeneity regions) in heavy ion collisions. This method is also often called Femtoscopy, referring to the femtometer length scale of the studied system. It provides us with a picture of the freezeout configuration for particles with different momenta, as well as information about the initial source shape, which together with the measured final source shape in momentum-space allows to study the evolution of the system. The lifetime of the system can also be extracted from a full three dimensional analysis.

It was first shown in 1960 that the distribution of pions emitted in $p\bar{p}$ collisions at small relative angles is affected by quantum statistical effects and is sensitive to the size of the emitting source [19]. Since then, the correlation technique with two identical particles at small relative momentum, often called intensity, or Hanbury Brown–Twiss (HBT), interferometry [20–24], has been used to study the space-time structure of the pion-emitting source from hadron-hadron and electron-positron to heavy-ion collisions (for a review, see [4]). The so-called HBT radii, obtained in these analyses, characterize the spatial and temporal extent of the source emitting pions of a given momentum, the extensions of the so-called homogeneity regions. Due to the space-momentum correlations in particle emission, the HBT radii become sensitive to the collective velocity fields, and as such provide information on the dynamics of the system evolution [4]. Recent measurements of the centrality dependence of HBT radii in Pb–Pb collisions at LHC energies [25] further confirm the scaling of the effective source volume with the particle rapidity density as well as stronger radial flow at higher energies.

Pion interferometry of anisotropic sources (azimuthally differential femtoscopy) was suggested in [26, 27], and the corresponding measurements [28] appeared shortly after strong directed and in-plane elliptic flow were measured in Au–Au collisions at the Alternating Gradient Synchrotron (AGS) [29, 30]. Anisotropic flow, the response of the system to the initial geometry, is usually characterized by the Fourier decomposition of the particle azimuthal distribution and quantified by the harmonic strength and orientation of the corresponding flow plane. Azimuthally differential femtoscopic measurements can be performed relative to different harmonic flow planes, providing important complementary information on the particle source. For example, the measurements of HBT radii with respect to the first harmonic (directed) flow at the AGS [31] revealed that the source was tilted relative to the beam direction [32]. Azimuthal dependence of the HBT radii relative to the higher harmonic ($n > 2$) flow planes can originate only from the anisotropies in collective flow gradients [33, 34] and the observation [35] of such a modulation unambiguously signals a collective expansion and anisotropy in the flow fields. In particular, measurements of HBT radii with respect to the second harmonic (elliptic) flow provide information on the evolution of the system shape, which is expected to become more spherical at freeze-out compared to the initial state due to stronger in-plane expansion. In the recent RHIC beam energy scan, it was found that the eccentricity at freeze-out decreases continuously with increasing beam energy [36], a trend consistent with predictions by hydrodynamic and hadronic transport models [37, 38]. Earlier measurements [9, 39] showed that even at the highest RHIC energies the source at freeze-out remains out-of-plane extended, albeit with eccentricities significantly lower than the initial ones. Hydrodynamical calculations [37] predicted that at the Large Hadron Collider (LHC) energies, about an order of magnitude higher than the top RHIC energy, the pion source should eventually become isotropic, or even in-plane extended.

ALICE experiment is optimized to study high-energy heavy-ion collisions in detail to get an idea about the state of matter shortly after the big bang (QGP). The life time of this state of matter is too short to allow a direct measurement of position and size. Whereas,

two particles correlation can be used to study the space-time extension of the QGP. Bose-Einstein correlation of two identical (pions) used to extract the size of the freeze-out source in different directions to measure the shape of this region.

In the following chapters, we will give a short overview of the LHC and the ALICE detector. We will then give a short overview of some of the previous HBT results. Finally, we will move on to the main topic of this thesis: azimuthally-differential HBT analysis.

CHAPTER 2 EXPERIMENTAL SETUP

2.1 Large Hadron Collider

The Large Hadron Collider (LHC) [40] is currently the biggest particle accelerator in the world. It is the result of more than 20 years of planning and construction by a collaboration of around 10,000 physicists and engineers from all over the world. It was built from 1998 to 2008 at the European Organisation for Nuclear Research (CERN) at the French-Swiss border in the vicinity of Geneva. It is formed of a circular tunnel of 26.7 km in circumference, 45 to 170 meters underground. LHC is a synchrotron which uses two separate beam pipes. The machine was fully constructed in 2008 and started its operation in the summer of that year. However, on 19th September 2008 during the commissioning phase, a massive magnet quench happened which caused an extensive leakage of liquid helium, used for the cooling of the superconducting magnets, as well as major damage to some parts of the LHC. In the next year, 2009, repair and upgrade works were carried on in order to prevent similar incidents in the future. Finally, on the 23rd of November 2009, the machine successfully delivered the first p-p collisions at $\sqrt{s_{\text{NN}}} = 900$ GeV. Since that time the LHC has delivered hundreds of millions of collisions. At the end of 2010 and 2011, there were dedicated heavy-ion Pb-Pb runs with collision energy $\sqrt{s_{\text{NN}}} = 2.76$ TeV. In 2015, the energy has been increased to $\sqrt{s_{\text{NN}}} = 5.02$ TeV for Pb-Pb ion collisions.

Figure 2.1 shows a diagram of the LHC accelerators and four major experiments. Protons and ions are injected into the LHC ring in bunches of up to 10^{11} particles, with bunches traveling in both directions, clockwise and counterclockwise, around the ring. The bunches are spaced a few nanoseconds apart. There are around thousands of bunches per beam in proton-proton mode, while hundreds in Pb-Pb mode. Those bunches are steered around the ring with very strong magnets (8 Tesla). The two beams are only allowed to collide at four points where the detectors reside. The four major LHC experiments are: ALICE, LHC-b, CMS, ATLAS. There can be millions or even hundreds of millions of proton-proton collisions per second. Whereas, ions have collision rates in the thousands.

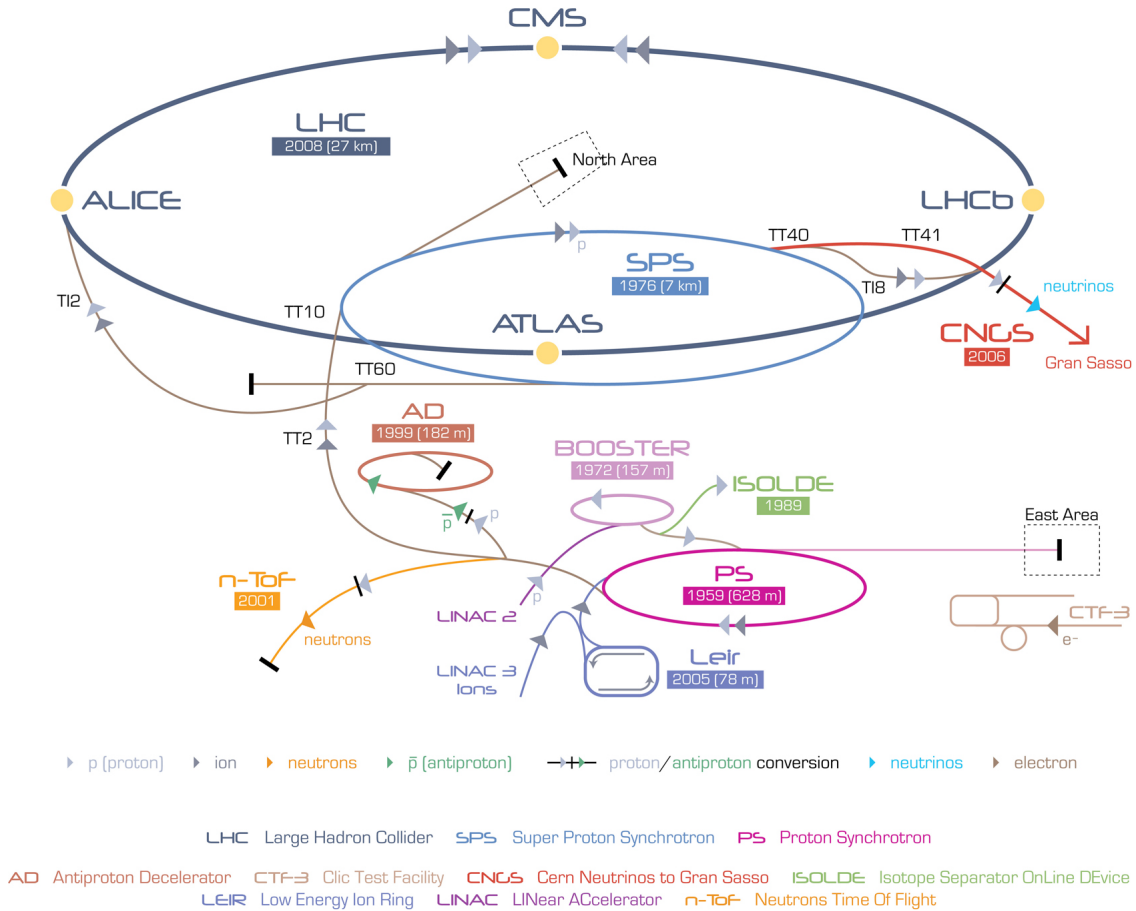


Figure 2.1: A schematic view of the Large Hadron Collider [14]. Proton and/or Pb ion beams go through a series of accelerators before being injected into the collider. Beams travel in both directions, clockwise and counterclockwise, around the LHC, and the two beams are only allowed to collide at the four main detectors: ALICE, ATLAS, LHC-b, and CMS.

2.2 A Large Ion Collider Experiment (ALICE)

In this section, we will describe two main parts required to perform a physics analysis at ALICE collaboration. The first part is the description of the hardware used to collect the data (ALICE detectors) and the second part is the software used to get a physical results from the collected data.

2.2.1 ALICE Detectors

ALICE, A Large Ion Collider Experiment, is one of the large experiments at the LHC. ALICE collaboration involves more than 1800 physicists, engineers and technicians from more than 60 countries across the world. The detector measures $16 \times 16 \times 26 \text{ m}^3$ and weights

about 10,000 tons [41]. It provides an excellent tracking quality and particle identification over a large range of momentum, and in high multiplicity region of central Pb-Pb collisions at the LHC. The layout of the ALICE detector is shown in Figure (2.2). The central portion of the detector covers pseudorapidity region $|\eta| < 0.9$ and maintain a magnetic field up to 0.5 T.

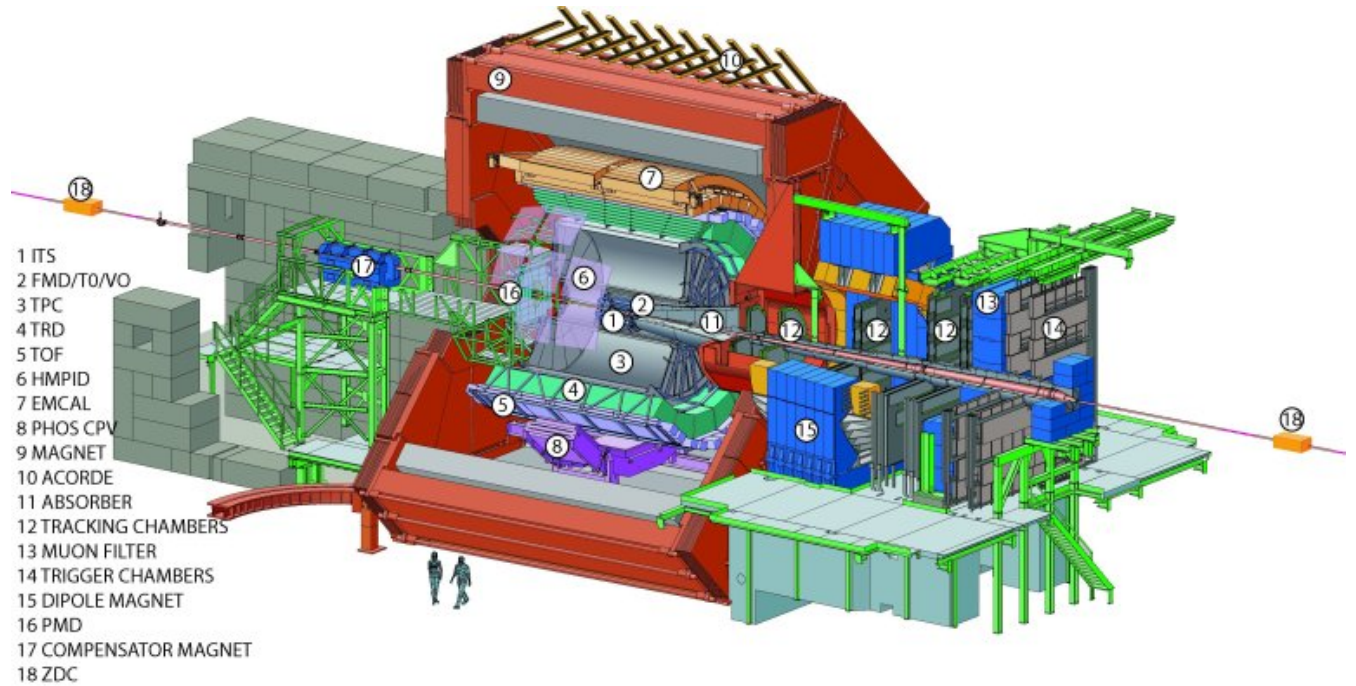


Figure 2.2: Schematic view of the ALICE detector.

2.2.1.1 The Time-Projection Chamber (TPC)

The TPC is the main tracking device [1]. It has a cylindrical shape with inner radius of 0.85 m, outer radius 2.5 m (sensitive volume), and has a length of 5 m. It provides information about charged particles (their momenta, positions of vertices and particle identification). Figure 2.3 shows a schematic picture of the TPC. It is a gas detector with a volume of 90 m^3 , filled with a $Ne - CO_2 - N_2$ gas mixture. A drift field of 100 kV stretches between the central electrode (which is located at $z = 0$) and the two readout planes at $z = 2.5 \text{ m}$ and $z = -2.5 \text{ m}$. The readout of the signal is performed by 570132 pads of 3 different sizes, which form the cathode of the Multi-Wire Proportional Chambers (MWPC) located at the TPC

end caps. The end caps are segmented into 18 trapezoidal sectors. These sectors are divided radially in two chambers with varying pad sizes, optimized for the radial dependence of track density. Pads are organized in 159 rows radially. The TPC is able to track particles in the pseudorapidity range of $|\eta| < 0.9$ for full radial length and up to $|\eta| < 1.5$ for 1/3 radial length. Particles with transverse momenta p_T from about 200 MeV/ c (at nominal magnetic field of 0.5 T) up to 100 GeV/ c can be measured. The momentum resolution of the tracks is better than 2.5% for tracks with a momentum below 4 GeV/ c . The TPC allows up to 8,000 tracks per unit of rapidity in one collision event to be reconstructed and identified.

Figure 2.4 shows a Pb-Pb collision recorded in the first run of the LHC. The tracking by the ITS is shown in white, while tracking from the TPC is yellow. The TPC can provide quality tracking information for ion events with thousands of charged particles, but it has the drawback of being a slow detector compared to the ITS. The maximum drift time of a track is about 90 s, so if two or more events occur within that window their tracking information can overlap. This is called event pile-up. Due to this limitation, the TPC can isolate and record central Pb-Pb events (events with head-on collisions) at a rate of 300 Hz and p-p events at a rate of 1 kHz.

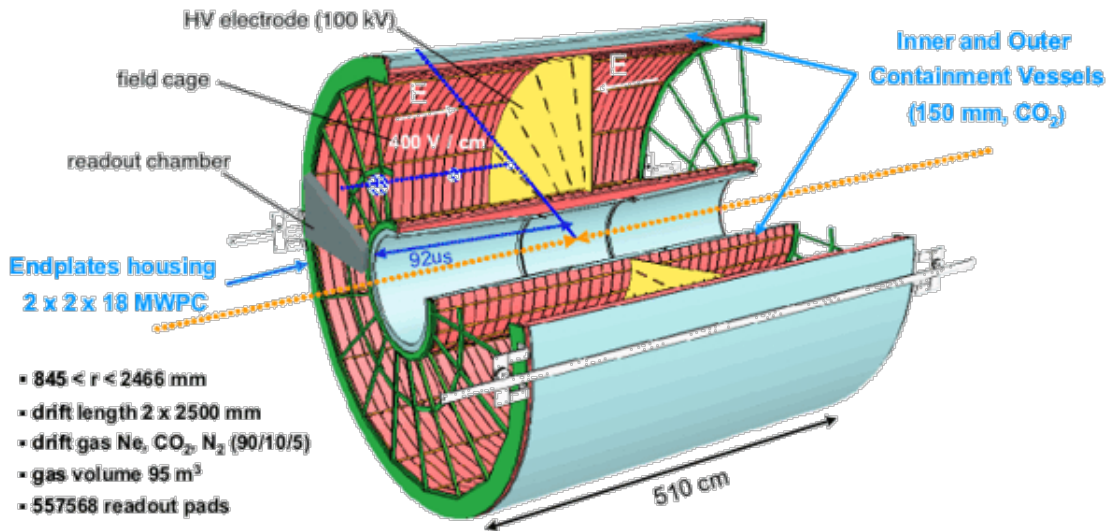


Figure 2.3: Layout of the The Time Projection Chamber layout. Figure from [1].



Figure 2.4: An example of a Pb-Pb collision measured at the ALICE detector. Charged particles traveling through the detector leave behind tracks that the detector can measure, each of which is depicted by a colored line. The white region in the center of the detector is the Inner Tracking System, while the surrounding grey region is the Time Projection Chamber. Tracks measured by the ITS are grey, while tracks found by the TPC are yellow. Combined tracking information from both detectors is used to improve the momentum resolution of each track.

2.2.1.2 The Inner Tracking System (ITS)

The ITS is the closest detector to the interaction point [2]. It is made from silicon and consist of three different subsystems: the Silicon Pixel Detector (SPD), the Silicon Drift Detector (SDD), and the Silicon Strip Detector (SSD). It is 97.6 cm long and ranges from a radius $R = 3.9$ cm to a radius $R = 43.6$ cm. The ITS is responsible for the determination of the primary and secondary vertices with a resolution $\sim 100\mu\text{m}$. It is also used for tracking and identifying particles with momentum less than $200 \text{ MeV}/c$ that do not interact with other detectors. It contributes to the global tracking as well as to PID via a dE/dx measurement in the SDD and SSD. The detector layout is shown in Fig.2.5 [2].

2.2.1.3 The Time-Of-Flight Detector (TOF)

The TOF covers pseudo-rapidity range $|\eta| < 0.9$, it has a length of 7.5 m, an inner radius of 3.7 m and outer radius 3.9 m. It is designed to identify particles from the difference in the time of flight (t). The main task of TOF is to improve particle identification. The

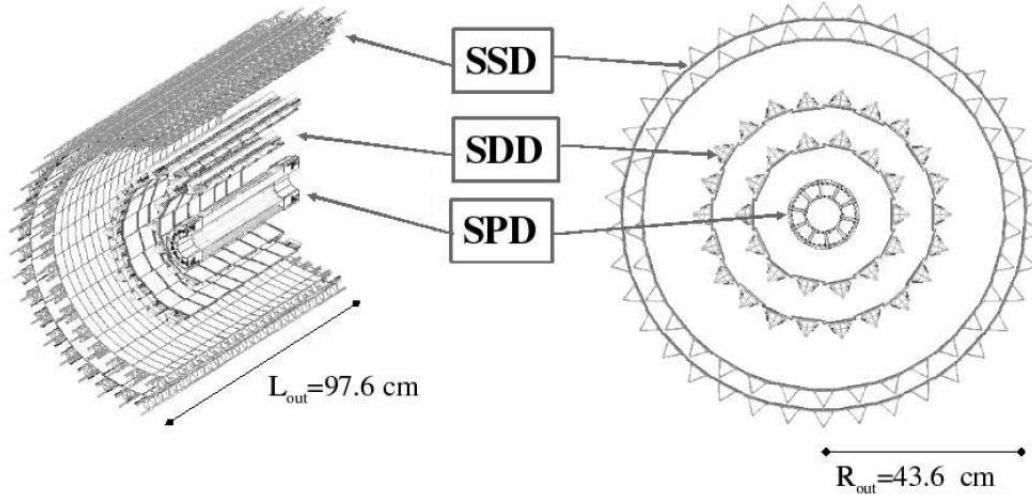


Figure 2.5: Layout of the Inner Tracking System. Figure from [2].

measurement of the time of flight of particles can distinguish between protons, kaons, and pions at intermediate p_T of 0.5–3.0 GeV/ c for pions and kaons and 0.5–6.0 GeV/ c for protons [41].

2.2.1.4 V0 Detector

The V0 detector (also referred to as VZERO) [161] is a pair of forward scintillator arrays located on each side, A ($\eta > 0$) and C ($\eta < 0$), of the interaction point [3]. They are called V0A and V0C, respectively. The detector records the amplitude as well as the arrival time of signals produced by charged particles. It also serves as the main interaction trigger. V0C and V0A are located 90 cm and 340 cm from the TPC center on opposite sides of ALICE, respectively. They consist of four rings covering pseudorapidity ranges of $3.7 < \eta < 1.7$ for V0C and $2.8 < \eta < 5.1$ for V0A. Each ring has 8 sections in the azimuthal directions. The thickness of the V0-A and V0-C scintillators is 2.5 cm and 2 cm, respectively. Each ring covers the full azimuth and is segmented into 8 sectors that are read independently. The schematic picture of the V0 arrays is presented in Fig.2.6.

2.2.1.5 Other Detectors

The Transition-Radiation Detector (TRD) is mainly used to distinguish between electrons and pions at high p_T , which is not possible with the dE/dx measurement [42]. It is located

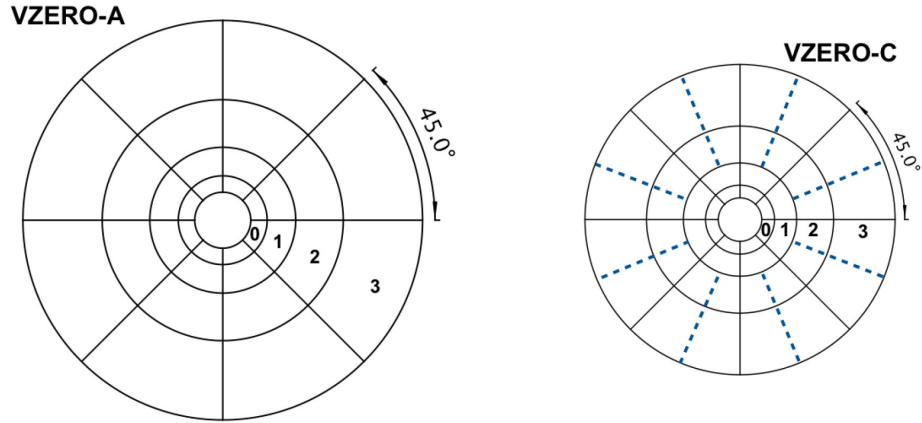


Figure 2.6: Schematic view of the V0 detector. Figure from [3].

at radii from 2.9 m to 3.7 m. The TRD is based on measuring the transition radiation which occurs when a charged particle propagates between two materials with different dielectric constants. Since the amount of transition radiation is proportional to $\gamma = v/c$, electrons and pions can be distinguished up to p_T of several GeV/c .

The High Momentum Particle Identification (HMPID) extends the range of momentum for which the separation power is high enough to discriminate between pions and kaons even to $3 \text{ GeV}/c$, and kaons and protons to $5 \text{ GeV}/c$. The detector uses the ring-imaging Cherenkov counters.

The ElectroMagnetic CALorimeter (EMCAL) is a Pb-scintillator sampling calorimeter with the cylindrical geometry covering the phase-space: $|\eta| < 0.7$, $\varphi = 107^\circ$. The main application is the analysis of jet physics.

The PHOton Spectrometer (PHOS) is an electromagnetic calorimeter consisting of lead-tungstate crystals. It enables the study of the initial state of the system produced in the heavy-ion collision by the measurement of the direct photons. In addition it is used to analyze the jet quenching using 0 with high p_T .

The ALICE COsmic Ray DEtector (ACORDE) is an array of plastic scintillator counters. The detectors purpose is to provide a trigger signal for the calibration and the alignment of the tracking detectors. ACORDE may also be used to study the atmospheric muons together

with TPC, TRD and TOF.

The muon spectrometer is optimized to analyze the heavy quark resonances, such as J/ψ , using their decay pattern into $\mu_-\mu_+$ pair. The acceptance of the spectrometer is $4 < \eta < 2.5$. The detector is built of the front absorber, the tracking and the trigger system

The Zero Degree Calorimeter (ZDC) is composed of two neutron and two proton calorimeters located symmetrically on both sides of the interaction point. It is used for the measurement of the spectator nucleons and serves mainly for the triggering. In addition there is an electromagnetic calorimeter which helps to distinguish between most central and most peripheral events since in both cases the number of nucleons registered by the nucleon calorimeters is small: in former there are few spectator nucleons, in latter they are bound in nuclear fragments.

2.2.1.6 Detectors Upgrade

The LHC will be increasing luminosity of the lead ions in 2018, hence the ALICE collaboration plans to upgrade the detector to fully utilize the potential of the collider and some of the upgrades is happening these days. The main objectives of the upgrade are the enhancement of the vertexing and the tracking at low-momentum as well as the ability to collect data at significantly higher rates (higher energy). It will require the improvement of the Inner Tracking System which will have 3 times better resolution of the distance of closest approach between the primary vertex and the track. Moreover, the new Time Projection Chamber will use the Gas Electron Multiplier detectors instead of the multi-wire proportional chambers to be able to operate with the higher collision rate. The upgrade will also cover, amongst others, the readout electronics of TRD, TOF and PHOS as well as DAQ system and offline data processing framework to handle the increased rate and number of events coming from the detector.

2.2.2 ALICE Software

2.2.2.1 ROOT

ROOT is a modular scientific software framework [43]. It provides all the functionalities needed to deal with big data processing, data analysis, visualization, and storage. It is mainly written in object-oriented C++ but integrated with other languages such as Python and R. Nowadays, ROOT is the most common software across the high-energy physics community around the World. In addition it has gained users from other fields of science. In the ALICE collaboration, we mainly use AliRoot. AliRoot uses the ROOT system as a foundation for ALICE-specific framework and applications.

2.2.2.2 AliRoot and AliPhysics

AliRoot, ALICE Off-line framework, is used for simulation, reconstruction, and analysis. AliRoot contains full representation of ALICE detector geometry as well as full simulation and reconstruction environment. It also includes full reconstruction chain and the analysis code. AliRoot, except for large existing libraries, such as GEANT3, GEANT, FLUKA, JET-SET, and some remaining legacy code, is fully based on the Object-Oriented programming paradigm and is written in C++. AliPhysics used to be a part of the AliRoot. Back in 2016, the ALICE collaboration decided to split part of the AliRoot into AliPhysics. AliPhysics includes the main C++ classes for the physics working groups. The main reason for the split is to have the C++ code that is in progress in the AliPhysics with daily tags (GitHub).

2.2.2.3 AliFemto

AliFemto package is one the AliRoot packages. It provides all the functionality for the femtoscopic analyses. The user can set all the required analysis parameter values such as particle types, masses, momentum, and many other parameters. All previous classes written by users, femtoscopists, are stored in the package which make it easier for new femtoscopists to start with. Many developments of AliFemto were needed to perform the analysis presented in this thesis. The main code used for the current analysis is accessible in the AliPhysics directory: `$ALICE_PHYSICS/src/PWGCF/FEMTOSCOPY/Train/MS`.

CHAPTER 3 HBT

3.1 Hanbury Brown-Twiss (HBT) Interferometry

Hanbury Brown and Twiss (HBT) showed, in 1950's, that the angular size of astronomical radio sources and stars could be measured from correlations of signal intensities in independent detectors [44]. The method uses two detectors to measure the light arriving from two separate emission points. The original application was to measure the diameters of the stars. This technique was developed and applied in particle physics by Goldhaber, to study angular distribution of pion pairs in $\bar{p}p$ annihilations. Over the years, this method has become a precise tool for measuring the space-time properties of the homogeneity regions at freeze-out in heavy ion collisions. Nowadays, this method is also called Femtoscopy, referring to the femtometer length scale of the studied system.

3.1.1 Theoretical Formalism

The emission of particles is characterized by a single particle spectrum as:

$$P_1(\vec{p}) = E \frac{dN}{d^3p}, \quad (3.1)$$

where E is the particle energy, N is the number of particles, \vec{p} is the three-momentum of the particle. The two particle spectrum is given by:

$$P_2(\vec{p}_1, \vec{p}_2) = E_1 E_2 \frac{dN_{pair}}{d^3p_1 d^3p_2}, \quad (3.2)$$

where E_1 is the energy of particle 1 and E_2 is the energy of particle 2, N_{pair} is the number particle pairs, \vec{p}_1 and \vec{p}_2 are the three-momentum of particle 1 and 2.

The two particle correlation function is defined as the ratio:

$$C(\vec{p}_1, \vec{p}_2) = \frac{P_2(\vec{p}_1, \vec{p}_2)}{P_1(\vec{p}_1)P_1(\vec{p}_2)}. \quad (3.3)$$

We now describe the correlation function in terms of the probability for the creation of a particle with momentum p and space-time point x . It will be described in terms of an

emission function $S(x, p)$.

The emission function $S(x, p)$ is described by the following Wigner function:

$$S(x, p) = \int \frac{d^4 y}{2(2\pi)^3} e^{-py} \langle J^*(x + \frac{y}{2}) J(x - \frac{y}{2}) \rangle, \quad (3.4)$$

where $J(x)$ is the classical source in terms of the spatial parameter x , $J^*(x)$ is the complex conjugate of $J(x)$. A single particle spectra in terms of the emission function is given as:

$$E \frac{dN}{d^3 p} = \int d^4 x S(x, p). \quad (3.5)$$

In order to describe the identical particle pair production, we have to account for the symmeterization of the wave function of the pair. Neglecting the Coulomb and strong interactions :

$$\phi(x_1, x_2, p_1, p_2) = \frac{1}{\sqrt{2}} [\phi(x_1, p_1) \phi(x_2, p_2) + \phi(x_1, p_2) \phi(x_2, p_1)] \quad (3.6)$$

Assuming that the wave function is a plain wave:

$$|\phi(x_1, x_2, p_1, p_2)|^2 = \left| \frac{1}{\sqrt{2}} (e^{ip_1 x_1} e^{ip_2 x_2} + e^{ip_2 x_1} e^{ip_1 x_2}) \right|^2 = 1 + \cos(q \cdot r), \quad (3.7)$$

where $q = p_1 - p_2$. Then the emission function of the particle pair can be written as:

$$P_2(\vec{p}_1 \vec{p}_2) = E_1 E_2 \frac{dN}{d^3 p_1 d^3 p_2} \approx \int d^4 x_1 d^4 x_2 S(x_1, p_1) S(x_2, p_2) |\phi(p_1, p_2, x_1, x_2)|^2. \quad (3.8)$$

We form the correlation function from the single and two-particle emission function by making a few assumptions. We assume that all particles with momentum p must have had their last interaction with the source at some point x . We assume that the emission process is initially uncorrelated. We use the *smoothness approximation*. In this approximation, the emission function has a smooth momentum dependence. Therefore the value of the function evaluated at the average momentum of the pair k , defined as $k = (p_1 + p_2)/2$, is the same

as the function evaluated at each momentum p_i . Another approximation is the *on-shell approximation*. Only three of the four relative momentum components are kinematically independent. This is due to the mass-shell constraint of the pions that implies that only three of the four relative momentum components are independent.

$$k \cdot q = p_1^2 - p_2^2 = m_1^2 - m_2^2 = 0 \quad (3.9)$$

$$q^0 = \frac{\vec{k}}{k^0} \cdot \vec{q} = \vec{\beta} \vec{q} \quad (3.10)$$

where m_i is the particle mass, $\vec{\beta}$ is the pair velocity, q^0 is the zeroth order of the pair momentum difference which corresponds to the energy, and k^0 is the zeroth order of the average pair momentum.

Then, the correlation function can be written as following:

$$C(\vec{q}, \vec{k}) = \frac{\int d^4x_1 d^4x_2 S(x_1, p_1) S(x_2, p_2) |\phi(x_1, x_2, p_1, p_2)|^2}{\int d^4x_1 S(x_1, p_1) \int d^4x_2 S(x_2, p_2)} \quad (3.11)$$

$$\approx 1 + \frac{|\int d^4x S(x, k) e^{iqx}|^2}{|\int d^4x S(x, k)|^2} = 1 + |\tilde{s}(q)|^2 \quad (3.12)$$

where $\tilde{s}(q)$ is the Fourier transform of the normalized source function $S(x, k)$. The q -dependence of the correlation function $C(\vec{q}, \vec{k})$ cannot test all of the x -directions of the emission function independently, and has a model dependence for the reconstruction of $s(x, k)$ that is unavoidable. The correlator combines spatial and temporal information depending on the pair velocity $\vec{\beta}$.

3.1.2 Coordinate System

We use the longitudinally co-moving system (LCMS), a rest frame moving along the longitudinal (beam) direction such that the momentum of the pair along the z axis is zero [4]. There are three axes perpendicular to each other and are defined in the following manner. *Long*, is the direction parallel to the beam, *out* is the direction that is parallel to the transverse momentum of the pair, and *side* is perpendicular to the other two axes, see Fig. 3.1.

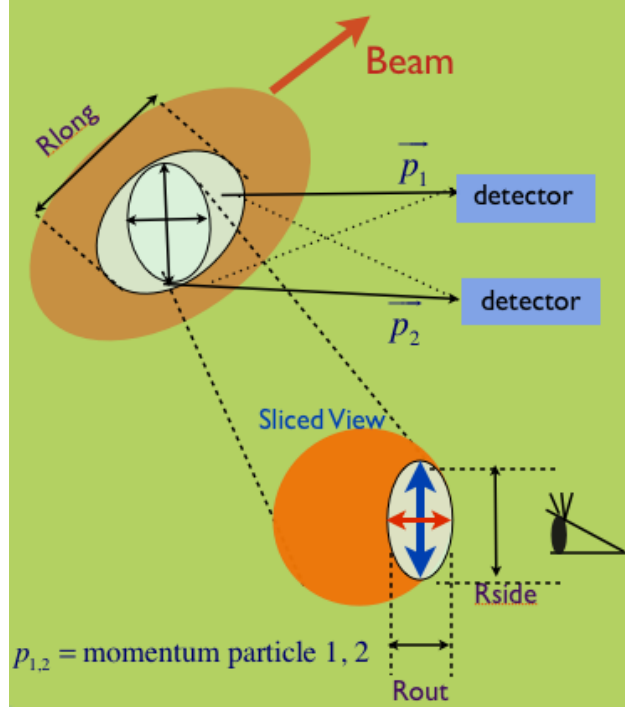


Figure 3.1: LCMS frame

Starting with any four vector V , we can project out the out-side-long components using the four-momentum P .

$$V_{long} = \frac{(P_0 V_z - P_z V_0)}{M_T} \quad (3.13)$$

$$V_{out} = \frac{(P_x V_x + P_y V_y)}{P_T} \quad (3.14)$$

$$V_{side} = \frac{(P_x V_x - P_y V_y)}{P_T} \quad (3.15)$$

where $P_T^2 = P_x^2 + P_y^2$, and $M_T^2 = P_0^2 - P_z^2$

In order to obtain any physical information from the measured correlation function, we generalize the source function and extract parameters.

3.1.3 Gaussian Parameterization

To compute the correlation function $C(\vec{q}, \vec{k})$, we approximate the source function $S(x, p)$ by a Gaussian. The space-time average point \bar{x} is a point corresponding to the maximum probability of emitting a pair particle with momentum k . The approximation of $S(x, k)$ at \bar{x}

is:

$$S(x, k) = N(k)S(\bar{x}(k), k) \exp \left[-\frac{1}{2} \tilde{x}^\mu(k) B_{\mu\nu}(k) \tilde{x}^\nu(k) \right] + \delta S(x, k), \quad (3.16)$$

where

$$\bar{x}^\mu(k) = \langle x \rangle, \tilde{x}^\mu(k) = x^\mu - \bar{x}^\mu(k), (B^{-1})_{\mu\nu}(k) = \langle \tilde{x}_\mu \tilde{x}_\nu \rangle. \quad (3.17)$$

We define the values as space-time averages over the source function:

$$\langle f(x) \rangle = \frac{\int d^4x f(x) S(x, k)}{\int d^4x S(x, k)} \quad (3.18)$$

The extra term $\delta S(x, k)$ can be neglected because it has a weak contribution in $C(\vec{q}, \vec{k})$. The two-particle correlation function is:

$$C(\vec{k}, \vec{q}) = 1 + \exp[-q^\mu q^\nu \langle \tilde{x}_\mu \tilde{x}_\nu \rangle(\vec{k})]. \quad (3.19)$$

The symmetric spatial correlation tensor $B_{\mu\nu}(k) \tilde{x}^\nu(k)$ has 10 independent components, but due to the mass-shell constraint this reduces to 6 parameters, the *HBT radii*.

We can obtain the Cartesian parameterization by eliminating q^0 from the previous equation:

$$C(\vec{k}, \vec{q}) = 1 + \exp \left[- \sum_{i,j=o,s,l} R_{i,j}^2(k) q_i q_j \right]. \quad (3.20)$$

The HBT radii are given by the covariances:

$$R_{i,j}^2 = \langle (\tilde{x}_i - \beta_i \tilde{t})(\tilde{x}_j - \beta_j \tilde{t}) \rangle \quad (3.21)$$

The three HBT radii, out, side, and long are:

$$R_o^2 = \langle (\tilde{x}_i - \beta_T \tilde{t})^2 \rangle \quad (3.22)$$

$$R_s^2 = \langle \tilde{y}^2 \rangle \quad (3.23)$$

$$R_l^2 = \langle (\tilde{z}_i - \beta_L \tilde{t})^2 \rangle \quad (3.24)$$

β_L is the pair longitudinal velocity and β_T is the transverse pair velocity. We see from the radii definitions that there is a mixture of spatial and temporal information on R_o and R_l , and R_s only has spatial dependence. Figure 3.2 shows a cartoon representation of the HBT radii.

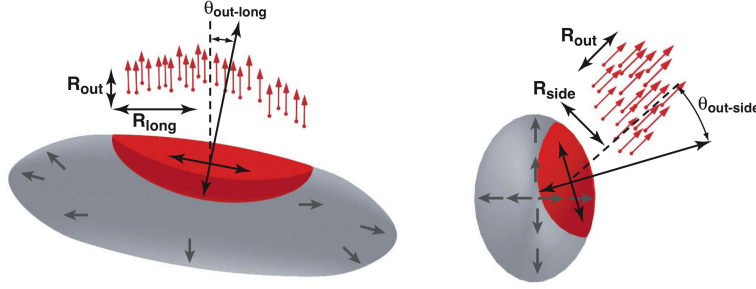


Figure 3.2: $R_{out}, R_{side}, R_{long}$ of the homogeneity region. Figure taken from [4]

3.1.4 Final state interactions

When charged particles are used in the femtoscopic analysis, strong and Coulomb interaction can have an effect on the wave function. There is a strong interaction between outgoing particles. The range of this interaction is estimated to be 0.2 fm [45]. However, the characteristic separation between pions, which will be the studied particles, is greater than 5 fm. Therefore the strong interaction is very weak and will be neglected. Particles that are traveling very close in phase-space feel a Coulomb interaction with the emission source and the other emitted particles. This interaction affects mostly particles with low q . The solution of the Schrödinger equation of coulombs effect is:

$$\psi_c(\vec{q}, \vec{r}) = \Gamma(1 + i\eta)e^{-\frac{1}{2}\pi\eta}e^{-\frac{1}{2}\vec{q}\vec{r}}[1 + \sum_{n=-1}^{+\infty} h_n(\frac{r}{a_0})^n], \quad (3.25)$$

where $\eta = \mu e^2/\hbar q$, μ is the reduced mass, e is the elementary charge, a_0 is the two-pion Bohr radius, $h_1=1$, and $h_n = \frac{n-1-i\eta}{-in\eta}h_{n-1}$. The integrated wave coulomb function over a Gaussian source function given by:

$$K_{coul}(\vec{q}) = \int d^3r \rho(\vec{r}) |\psi_c(\vec{r}, \vec{q})|^2 \quad (3.26)$$

The Coulomb interaction between the outgoing particle and the central source potential was found to be very small and decreases as the collision energy become ultra-relativistic [46].

3.2 Experimental Techniques

3.2.1 Experimental Correlation Function

The correlation function $C(\mathbf{q})$ was calculated as

$$C(\mathbf{q}) = \frac{A(\mathbf{q})}{B(\mathbf{q})}, \quad (3.27)$$

where $\mathbf{q} = \mathbf{p}_1 - \mathbf{p}_2$ is the relative momentum of two pions, $A(\mathbf{q})$ is the same-event distribution of particle pairs, and $B(\mathbf{q})$ is the background distribution of uncorrelated particle. The background distribution is built by using the mixed-event technique [22] in which pairs are made out of particles from two different events with similar centrality (less than 2% difference), event-plane angle (less than 10° difference), and event vertex position along the beam direction (less than 4 cm difference).

3.2.2 Log-Likelihood Fitting

We assume the following Gaussian fitting function:

$$G(q) = 1 + \exp(-R_o^2 q_o^2 - R_s^2 q_s^2 - R_l^2 q_l^2 - 2R_{os}^2 q_o q_s - 2R_{ol}^2 q_o q_l - 2R_{sl}^2 q_s q_l) \quad (3.28)$$

We fit the correlation function according to Bowler and Sinyukov equation [47]:

$$C(q) = N[\lambda G(q)F(q) + (1 - \lambda)]. \quad (3.29)$$

where N is the normalization, $G(q)$ is the Gaussian source function, and $F(q)$ is the Coulomb source. In order to fit the correlation function, a loglikelihood χ_{PML}^2 minimization [48] were used:

$$\chi_{PML}^2 = -2 \left[A \ln \left(\frac{C(A+B)}{A(C+1)} \right) + B \ln \left(\frac{(A+B)}{B(C+1)} \right) \right] \quad (3.30)$$

where A is the signal distribution, B is the background distribution, and C is the correlation function.

CHAPTER 4 AZIMUTHALLY-DIFFERENTIAL HBT

Pion interferometry of anisotropic sources (azimuthally differential femtoscopy) was suggested in [26, 27], and the corresponding measurements [28] appeared shortly after strong directed and in-plane elliptic flow were measured in Au–Au collisions at the Alternating Gradient Synchrotron (AGS) [29, 30]. Anisotropic flow, the response of the system to the initial geometry, is usually characterized by the Fourier decomposition of the particle azimuthal distribution and quantified by the harmonic strength and orientation of the corresponding flow plane. Azimuthally differential femtoscopic measurements can be performed relative to different harmonic flow planes, providing important complementary information on the particle source. For example, the measurements of HBT radii with respect to the first harmonic (directed) flow at the AGS [31] revealed that the source was tilted relative to the beam direction [32]. Azimuthal dependence of the HBT radii relative to the higher harmonic ($n > 2$) flow planes can originate only from the anisotropies in collective flow gradients [33, 34] and the observation [35] of such a modulation unambiguously signals a collective expansion and anisotropy in the velocity fields. In particular, measurements of HBT radii with respect to the second harmonic (elliptic) flow provide information on the evolution of the system shape, which is expected to become more spherical at freeze-out compared to the initial state due to stronger in-plane expansion. In the recent RHIC beam energy scan, it was found that the eccentricity at freeze-out decreases continuously with increasing beam energy [36], a trend consistent with predictions by hydrodynamic and hadronic transport models [37, 38]. Earlier measurements [9, 39] showed that even at the highest RHIC energies the source at freeze-out remains out-of-plane extended, albeit with eccentricities significantly lower than the initial ones. Hydrodynamical calculations [37] predicted that at the Large Hadron Collider (LHC) energies, about an order of magnitude higher than the top RHIC energy, the pion source should eventually become isotropic, or even in-plane extended. In contrast, hydrodynamics model studies have shown that the azimuthal dependence of the HBT radii relative to the third harmonic event plane angle (Ψ_3) can originate from the the anisotropies in collective

velocity gradients or the initial spatial anisotropy (triangular) [34]. The signs of the HBT radii relative to the third harmonic event plane angle oscillations constrain the origin of these oscillation [34]. In the previous section, we presented the non-azimuthal HBT results. In this section, we will introduce the event plane, an estimation of the reaction plane, show the HBT analysis procedure with respect to the second and third harmonic then show how the azimuthally-differential HBT analysis. was done.

4.1 Anisotropic Flow

Flow refers to a collective expansion of matter, resulting from the density gradient of the created fireball in nuclear collisions. The anisotropies in the initial shape of the fireball (figure 4.1) and the pressure gradients lead to anisotropic expansion of the system.

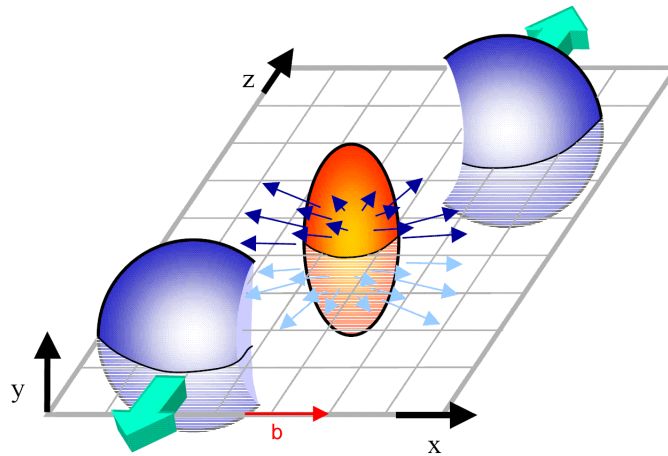


Figure 4.1: Schematic of the collision zone between two incoming nuclei where x-z plane is the reaction plane.

In a non central collision, the impact parameter \mathbf{b} together with the z axis (the beam line) define the **Reaction Plane** (figure 4.1).

The evolution of the system follows an isotropic expansion. Most particles radiated along the direction of the reaction plane. The asymmetry observed in the final momentum distribution of the radiated particles is called **anisotropic flow**.

In general, anisotropies in the azimuthal particle distribution are studied in terms of the Fourier decomposition [49].

$$E \frac{d^3N}{d^3p} = \frac{1}{2\pi} \frac{d^2N}{p_T dp_T dy} \left(1 + \sum_{n=1}^{\infty} 2v_n \cos(n(\phi - \Psi_R)) \right), \quad (4.1)$$

where E is the energy of the particle, p_T its transverse momentum, y the rapidity, ϕ the azimuthal angle, ψ_R the reaction plane angle and n is a positive integer which correspond to the n^{th} order harmonics.

The Fourier coefficients are given by:

$$v_n = \langle \cos[n(\phi - \psi_R)] \rangle \quad (4.2)$$

The first coefficient, v_1 , is called directed flow, v_2 is called elliptic flow, v_3 triangular flow and so on.

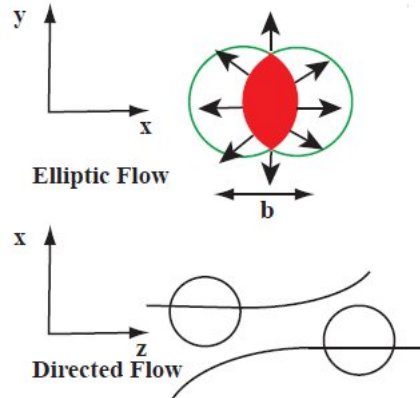


Figure 4.2: Schematic of the directed and elliptic flow.

4.1.1 Event Plane Method

The event plane method is the same as eq.(4.2), where the true reaction plane is replaced by the experimentally reconstructed event plane.

First, we have to reconstruct, on event-by-event basis, the event plane ψ from the anisotropy of the event itself. The procedure starts with the reconstruction of the **flow**

vector, \vec{Q} , defined as [49]:

$$\vec{Q}_n = \begin{pmatrix} \sum_i w_i \cos(n\phi(i)) \\ \sum_i w_i \sin(n\phi(i)) \end{pmatrix} = Q_n \begin{pmatrix} \cos(n\psi_n) \\ \sin(n\psi_n) \end{pmatrix}, \quad (4.3)$$

where the sum includes all the detected particles and w_i are the weights to enhance the contribution of particles with different flow contribution.

Therefore the reconstructed event plane angle of the n^{th} harmonic is given by the orientation of \vec{Q}_n :

$$\psi_n = \frac{1}{n} \arctan \left(\frac{Q_n^y}{Q_n^x} \right). \quad (4.4)$$

Experimentally, there is no access to the direction of the impact parameter and therefore neither to the reaction plane. However when performing azimuthally sensitive HBT interferometry, which will be discussed later on, the reconstructed event plane will act as the reference in the azimuthal direction.

The event plane resolution, will be used in the analysis later, is defined as:

$$R_n = \langle \cos [n(\Psi_n - \Psi_{RP})] \rangle. \quad (4.5)$$

In the above equation, the resolution factor depends on the number of particles N used in the Q-vector and the average flow of the event. Larger N will ensure better precision of the event plane and less sensitive to statistical fluctuations.

The estimation of the event plane resolution is given by [50]- [51]:

$$R(\chi) = \frac{\sqrt{\pi}}{2} \chi \exp(-\chi^2/2) \left[I_0 \left(\frac{\chi^2}{2} \right) + I_1 \left(\frac{\chi^2}{2} \right) \right] \quad (4.6)$$

where I_0 and I_1 are the modified Bessel function and χ is defined as:

$$\chi = v_n \sqrt{N}. \quad (4.7)$$

Experimentally, the resolution can be evaluated by applying the event plane method on each of the two sub-events A and B and comparing the obtained results. The two sub-events are obtained by dividing each event into two samples with equal multiplicities or different η range. The two sub-events are positively correlated since each is correlated with the reaction plane. Taking the square root of this correlation gives the event plane resolution:

$$R_{n,sub} = \sqrt{\langle \cos [n (\Psi_n^A - \Psi_n^B)] \rangle}. \quad (4.8)$$

The full event plane resolution is obtained using $R(\chi)$ from the resolution of the sub-events:

$$R_{full} = R\left(\sqrt{2}\chi_{sub}\right) \quad (4.9)$$

4.2 Data Analysis

4.2.1 Data Sample

In this analysis, we used two datasets. The first dataset was recorded in 2011 (LHC11h) during the second Pb–Pb running period of the LHC. Below is the list of runs for LHC11h chosen. “Run” refers to the data taken during a continuous recording session of the ALICE detector, as well as to the duration of the recording session lasted. Runs can include anything from minutes to few days of data collection. Not all the runs recorded are used in this analysis. For example, a particular run might only exist for detector calibration purposes, or a subdetector essential for this analysis might have been offline during the data recording session. Runs were selected if they were listed as “Good Run” in the ALICE Run Condition Table.

-

167915, 167920, 167985, 167987, 167988, 168069, 168076, 168107,
 168108, 168115, 168310, 168311, 168322, 168325, 168341, 168342,
 168361, 168362, 168458, 168460, 168464, 168467, 168511, 168512,
 168514, 168777, 168826, 168992, 169035, 169040, 169044, 169045,
 169091, 169094, 169099, 169138, 169144, 169145, 169148, 169156,
 169160, 169167, 169238, 169411, 169415, 169417, 169418, 169419,
 169420, 169475, 169498, 169504, 169506, 169512, 169515, 169550,
 169553, 169554, 169555, 169557, 169586, 169587, 169588, 169590,
 169835, 169837, 169838, 169846, 169855, 169858, 169859, 169965,
 170027, 170040, 170081, 170083, 170084, 170085, 170088, 170089,
 170091, 170155, 170159, 170163, 170193, 170203, 170204, 170207,
 170228, 170230, 170268, 170269, 170270, 170306, 170308, 170309,
 170311, 170312, 170313, 170387, 170388, 170572, 170593;

The second dataset recorded in 2015 (LHC15o). Below is the list of runs chosen.

•

246487, 246808, 246930, 246675, 246676, 246805, 246807, 246424,
 246809, 246428, 246942, 246431, 246945, 246434, 246948, 246949,
 246751, 246844, 246845, 246846, 246847, 246851, 246980, 246982,
 246855, 246984, 246859, 246989, 246991, 246864, 246865, 246994,
 246867, 246871, 246488, 246493, 246750, 246495, 246757, 246758,
 246759, 246760, 246937, 246763, 246765, 246804, 246272, 246275,
 246276, 245766, 246151, 246152, 246153, 246148, 245775, 245705,
 246036, 246037, 245785, 246042, 246089, 245731, 246048, 245793,
 246178, 246053, 246182, 246087, 245683, 246217, 245692, 245949,
 245952, 245954, 245700, 245829, 245831, 245833, 245963, 246222,
 246225, 246115, 246181, 246113, 245729, 245738, 246049, 246001,
 246003, 245752, 246012, 245759;

The main difference between the two datasets is the collision energy. In 2015, the Pb–Pb collision energy has increased from 2.76 TeV (2011) to 5.02 TeV. For the 2011 datasets, approximately 2 million minimum bias events, 29.2 million central trigger events, and 34.1 million semi-central trigger events were used in this analysis. Whereas, for 2015 datasets approximately 20 million minimum bias events were used.

Approximately two-thirds of these runs were taken with the magnetic field of the ALICE detector in the negative configuration, and one third had the magnetic field in the positive configuration. Having data from both configurations allows for consistency checks; one can see if physics results have any dependence on the detector’s magnetic field polarity. In this analysis, the correlation functions were constructed separately among the the two field configuration found the results to be consistent with each other and the difference in the results was considered in the systematic uncertainties.

4.2.2 Centrality flattening

Each event is characterized by the so-called centrality percentile. There are 100 centrality bins ranging from 0% (head-on collisions) to 99% (glancing collisions). Figure 4.3 shows an illustration of collision centrality. The centrality bin would be sampled equally using the minimum bias trigger. The LHC11h dataset had three main triggers; central and semi-central triggers in addition to the minimum bias trigger, so the centrality bins are not equally filled. There are approximately as many events in the 0–10% centrality class as there are in the 10–50% centrality class. While the events in the 10–50% show almost an even sampling, the number of events in each of the 0–10% centrality class differ by a few percent. In this analysis, we used a technique called centrality flattening to ensure that each of the 0–10% bins are sampled evenly. For each magnetic field configuration, each centrality bin is assigned a weight that brings that bin match with the bin with the smallest overall content, which is the 9% bin in our analysis. We use those weights and a random number generator (to prevent bias) to determine whether to throw away any given event or not.

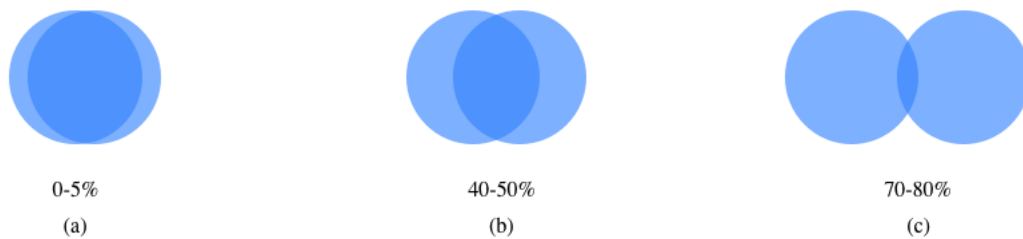


Figure 4.3: Cartoon representation of the collision centrality percentile.

4.2.3 Analysis Software

The analysis was performed using the AliFemto package which is part of the AliPhysics framework (vAN-20160726-1).

4.2.4 Filter Bits, Event Cuts, and Track Cuts

ALICE collaboration has a standardized definition called filter bit. The filter bit 7 is used in this analysis. The information about the track cuts using this filter bit is presented in Table 4.1.

Table 4.1: Filter bit 7 information
Filter bit 7: GetStandardTPCOnlyTrackCuts():
SetMinNClustersTPC(50)
SetMaxChi2PerClusterTPC(4)
SetAcceptKinkDaughters(kFALSE)
SetMaxDCAToVertexZ(3.2)
SetMaxDCAToVertexXY(2.4)
SetDCAToVertex2D(kTRUE)

More information on filter bit 7 and description of the cuts introduced Tabel 4.1 can be found at the following website: <https://twiki.cern.ch/twiki/bin/viewauth/ALICE/AddTaskInfoAOD145>

The position of the primary event vertex along the beam direction V_z was determined for each event. Events with $|V_z| < 8$ cm were used in this analysis to ensure a uniform pseudorapidity acceptance. Tracks used are the TPC only tracks as recommended by the femto group in order to avoid bias due to fake hits in the ITS. The TPC has 18 sectors covering full azimuth with 159 pad rows radially placed in each sector. Tracks with at least 80 space points in the TPC have been used in this analysis. Tracks compatible with a decay in flight (kink topology) were rejected. The track quality was determined by the χ^2 of the Kalman filter fit to the reconstructed TPC clusters. The χ^2 per degrees of freedom was required to be less than 4. For primary track selection, only trajectories passing within 3.2 cm from the primary vertex in the longitudinal direction and 2.4 cm in the transverse direction were used. Based on the specific ionization energy loss in the TPC gas compared with the corresponding Bethe-Bloch curve, and the time of flight in TOF, a probability for each track to be a pion, kaon, proton, or electron was determined. Particles for which the pion probability was the largest were used in this analysis. Pions were selected in the pseudorapidity range $|\eta| < 0.8$ and $0.15 < p_T < 1.5$ GeV/ c .

Requiring a minimum value in the two-track separation parameters $\Delta\varphi^*$ and $\Delta\eta$ controls two-track reconstruction effects such as track splitting or track merging. The quantity φ^* is

defined in this analysis as the azimuthal angle of the track in the laboratory frame at the radial position of 1.6 m inside the TPC. Splitting is the effect when one track is reconstructed as two tracks, and merging is the effect of two tracks being reconstructed as one. Also, to reduce the splitting effect, pairs that share more than 5% of the TPC clusters were removed from the analysis. Further information about the pair cuts is presented in the next section.

4.2.5 Pair Cuts Studies

4.2.5.1 Two-Track Studies

In this section, we present a systematic study of pair cuts to remove track splitting and merging effects. We used the Monte Carlo Hijing for LHC11h to study the effect of the pair cuts without the Bose-Einstein correlations found in real collected data. This work is mainly done by my colleague Vera Loggins [5].

For this study, we varied $\Delta\eta = |\eta_1 - \eta_2|$ and $\Delta\varphi^*$, the angular distance between two tracks at a certain radius (1.6 m inside TPC) see fig 4.4, for systematic studies. We study the track splitting and merging as a function of angular distance $\Delta\varphi^*$ defined as:

$$\Delta\varphi^* = \varphi_1 - \varphi_2 + \arcsin\left(\frac{z \cdot e \cdot B_z \cdot R}{2p_{T1}}\right) - \arcsin\left(\frac{z \cdot e \cdot B_z \cdot R}{2p_{T2}}\right), \quad (4.10)$$

where φ_1 and φ_2 are the azimuthal angles of the tracks, B_z is the magnetic field in the z-direction, p_{T1} and p_{T2} are the transverse momenta, and e is the elementary charge of track. R is the radius inside the detector (TPC in our study). Different values of R can be used. In this study we fix the value of R to 1.6 m from the center of the TPC. The reconstructed

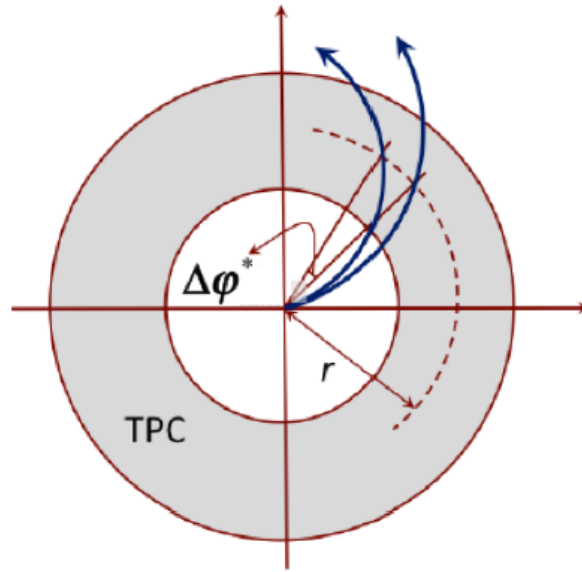


Figure 4.4: Cartoon illustration of $\Delta\varphi^*$

distance of closest approach (DCA) of the tracks to the primary vertex in the transverse direction DCA_{xy} and z-direction DCA_z were studied. The global DCA cuts were varied to decide the optimal values. $DCA_{xy} < 2.4$ cm and $DCA_z < 3.0$ cm are the standard cuts as shown in filter bit 7. Table 4.2 shows the three different DCA cuts. Figure 4.5 and 4.6 show the DCA_{xy} and DCA_z distributions along with the three different DCA cuts used.

Table 4.2: Three DCA values

DCA_{xy}	DCA_z
0.2 cm	0.15 cm
0.4 cm	0.3 cm
2.4 cm	3.0 cm

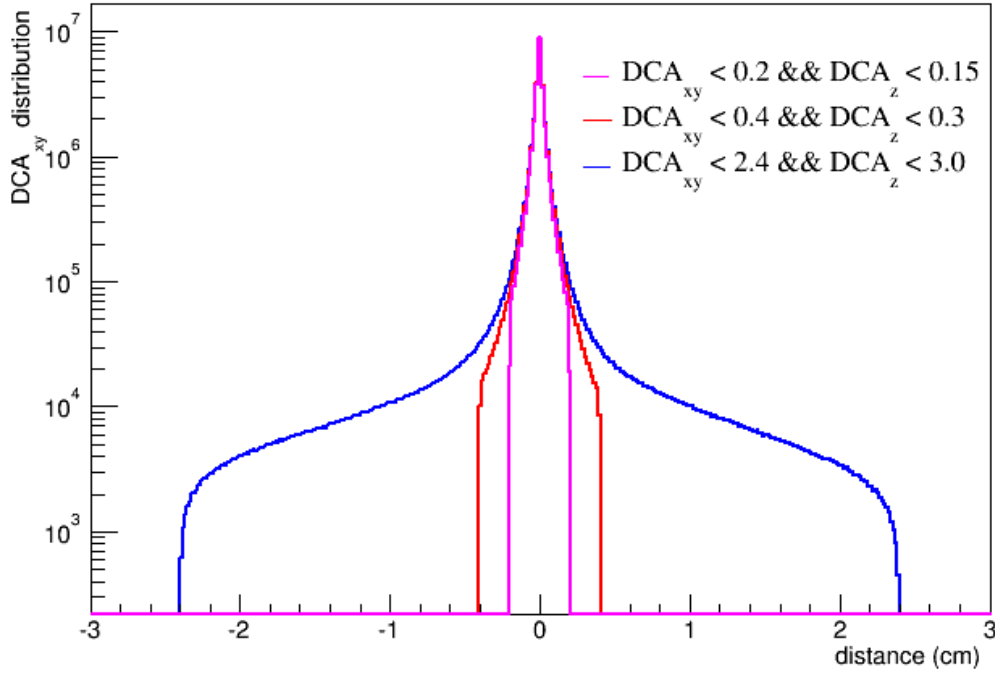
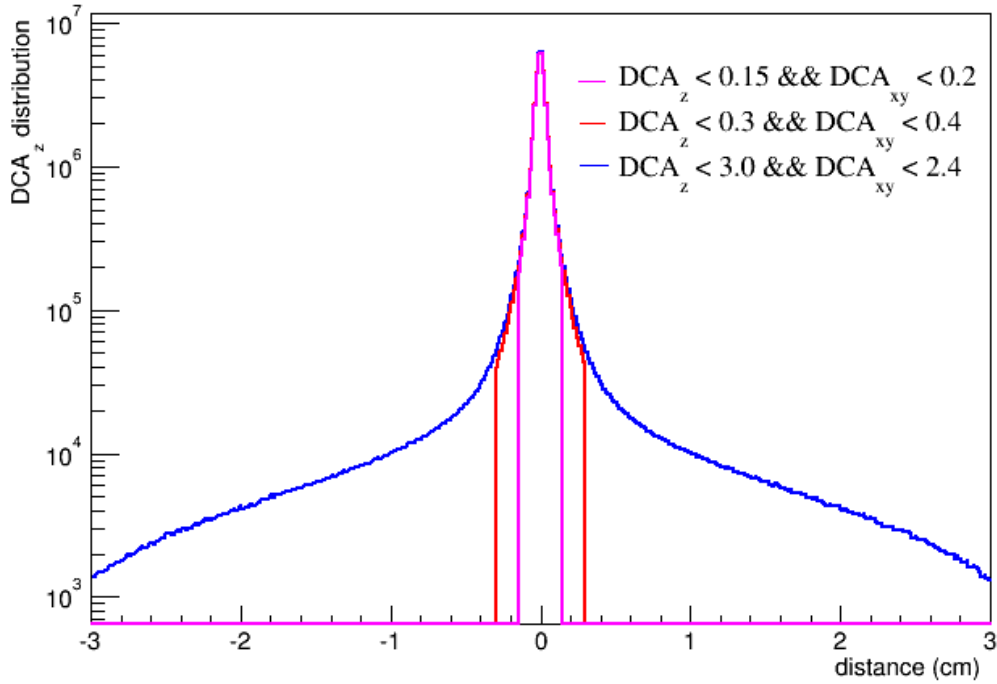


Figure 4.5: DCA_{xy} distribution. Figure from [5].

Different $\Delta\eta$ and $\Delta\phi^*$ cuts can be used. To apply a reasonable cuts, we studied the two dimensional correlation function of $\Delta\eta\Delta\phi^*$ using the Hijing MC for LHC11h (LHC12a17a_fix)

Figure 4.6: DCA_z distribution

where no Bose-Einstein correlation is presented. We used two different k_T ranges and three sets of DCA values. Figure 4.7, 4.9, 4.13, 4.14, 4.19, and 4.20 shows a depletion in the ratio near $\Delta\eta = 0$ and $\Delta\phi^* = 0$. In order to estimate the optimal values to use for the pair cut on $\Delta\eta$ and $\Delta\phi^*$, we did a 1-D projections presented in figures 4.9, 4.10, 4.11, 4.12, 4.15, 4.16, 4.17, 4.18, 4.21, 4.22, 4.23, and 4.24 for the k_T range 0.2-0.5 GeV/ c , and then again for the higher k_T range 0.5-1.0 GeV/ c . The ratio should have a maximum value of 1.0, otherwise this is an evidence of undesirable track splitting and merging.

Looking at the plots where $DCA_{xy} < 2.4cm$ and $DCA_z < 3.0cm$ were used, we see that both the $\Delta\eta$ and $\Delta\phi^*$ projections show that the maximum value of the ratio is 1.0 as expected. For further investigation on the DCA cuts and to choose $\Delta\eta$ and $\Delta\phi^*$ cuts. We present the one-dimensional correlation function for the Hijing MC data and apply different $\Delta\eta$ and $\Delta\phi^*$ pair cuts.

The one-dimensional correlation function is given by

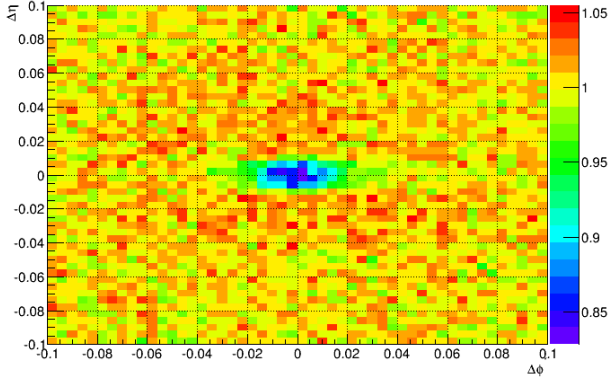


Figure 4.7: $DCA_{xy} < 0.2$ cm, $DCA_z < 0.15$ cm: Two dim. ratio $\Delta\eta\Delta\phi^*$ for k_T range 0.2-0.5 GeV/c. Figure from [5]

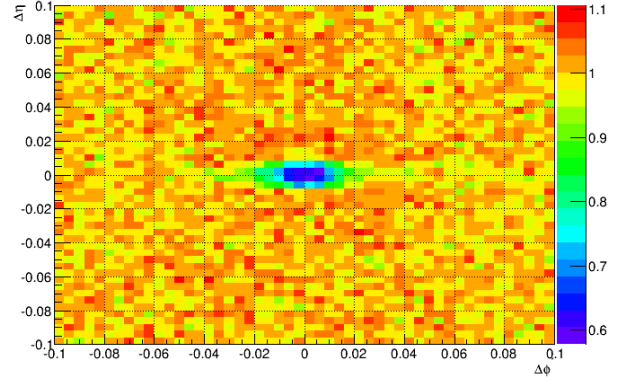


Figure 4.8: $DCA_{xy} < 0.2$ cm, $DCA_z < 0.15$ cm: Two dim. ratio $\Delta\eta\Delta\phi^*$ for k_T range 0.5-1.0 GeV/c. Figure from [5]

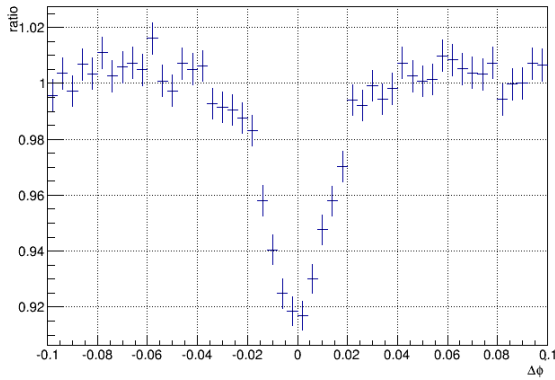


Figure 4.9: $DCA_{xy} < 0.2$ cm, $DCA_z < 0.15$ cm: $\Delta\phi^*$ projection for k_T range 0.2-0.5 GeV/c. Figure from [5]

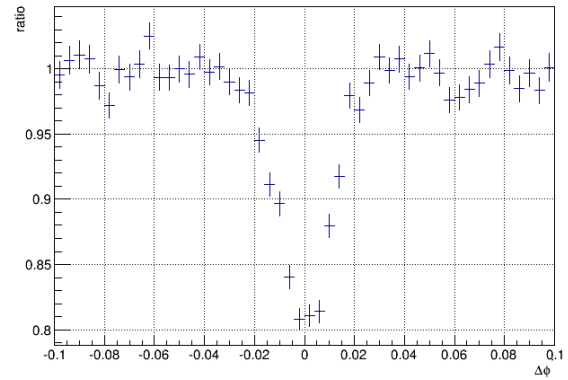


Figure 4.10: $DCA_{xy} < 0.2$ cm, $DCA_z < 0.15$ cm: $\Delta\phi^*$ projection for k_T range 0.5-1.0 GeV/c. Figure from [5]

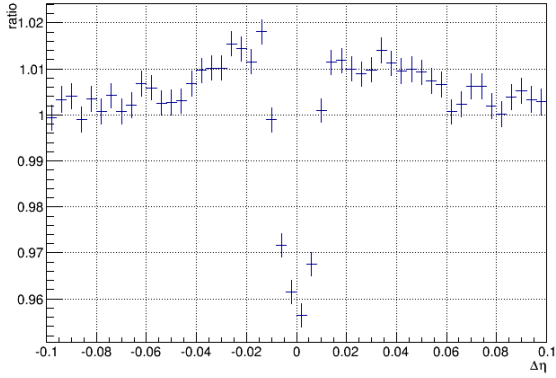


Figure 4.11: $DCA_{xy} < 0.2$ cm, $DCA_z < 0.15$ cm: $\Delta\eta$ projection for k_T range 0.2-0.5 GeV/ c . Figure from [5]

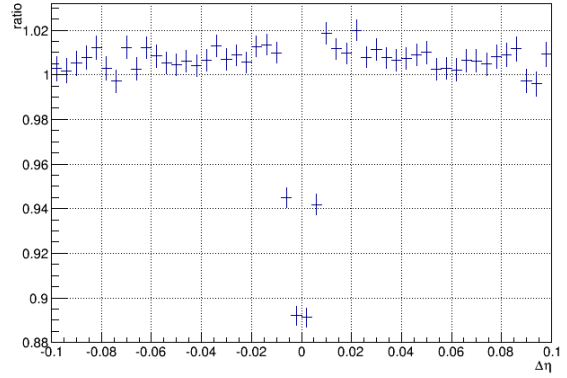


Figure 4.12: $DCA_{xy} < 0.2$ cm, $DCA_z < 0.15$ cm: $\Delta\eta$ projection for k_T range 0.5-1.0 GeV/ c . Figure from [5]

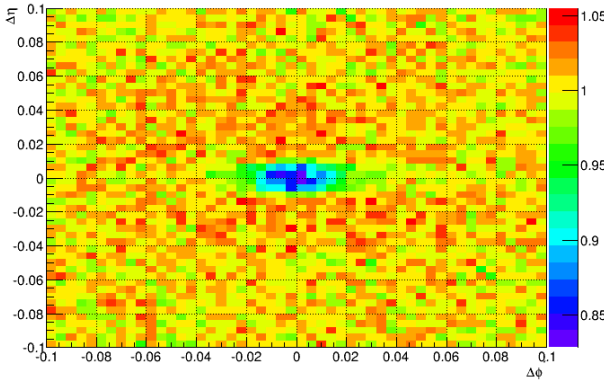


Figure 4.13: $DCA_{xy} < 0.4$ cm, $DCA_z < 0.3$ cm: Two dim. ratio $\Delta\eta\Delta\phi^*$ for k_T range 0.2-0.5 GeV/ c . Figure from [5]

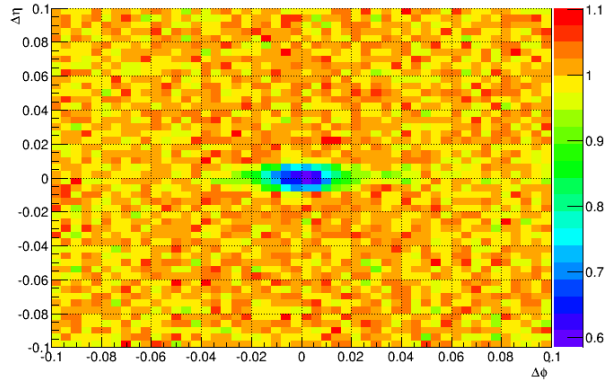


Figure 4.14: $DCA_{xy} < 0.4$ cm, $DCA_z < 0.3$ cm: Two dim. ratio $\Delta\eta\Delta\phi^*$ for k_T range 0.5-1.0 GeV/ c . Figure from [5]

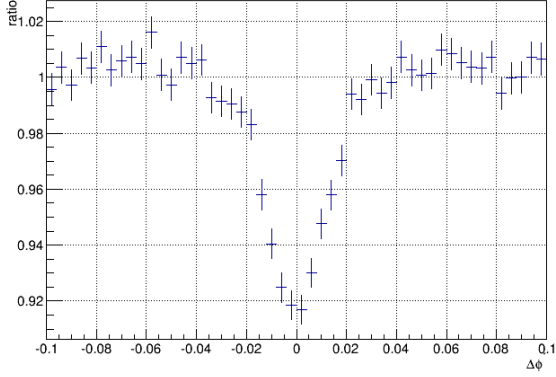


Figure 4.15: $DCA_{xy} < 0.4$ cm, $DCA_z < 0.3$ cm: $\Delta\phi^*$ projection for k_T range 0.2-0.5 GeV/ c . Figure from [5]

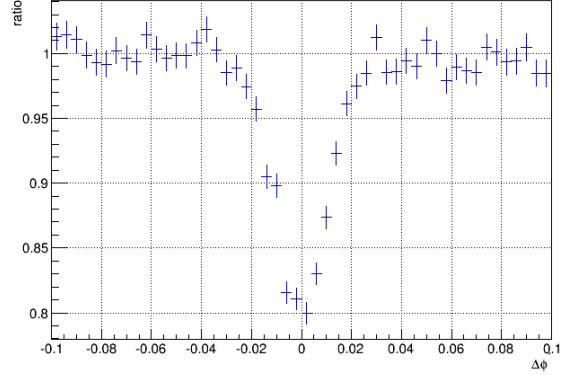


Figure 4.16: $DCA_{xy} < 0.4$ cm, $DCA_z < 0.3$ cm: $\Delta\phi^*$ projection for k_T range 0.5-1.0 GeV/ c . Figure from [5]

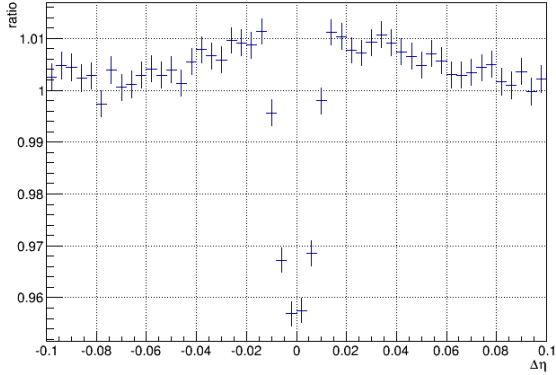


Figure 4.17: $DCA_{xy} < 0.4$ cm, $DCA_z < 0.3$ cm: $\Delta\eta$ projection for k_T range 0.2-0.5 GeV/ c . Figure from [5]

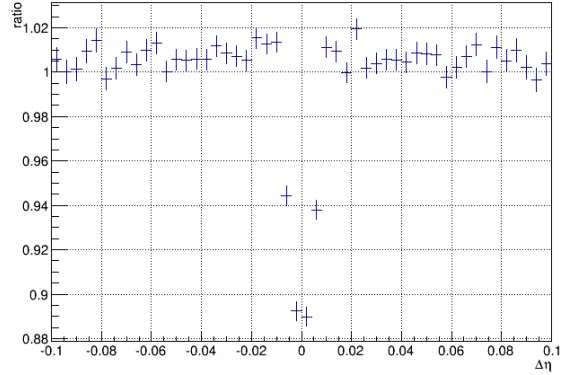


Figure 4.18: $DCA_{xy} < 0.4$ cm, $DCA_z < 0.3$ cm: $\Delta\eta$ projection for k_T range 0.5-1.0 GeV/ c . Figure from [5]

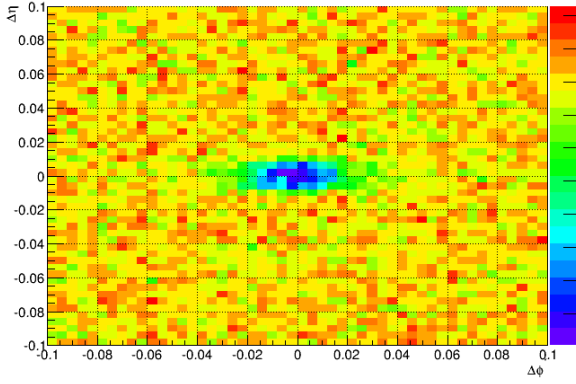


Figure 4.19: $DCA_{xy} < 2.4$ cm, $DCA_z < 3.0$ cm: Two dim. ratio $\Delta\eta\Delta\phi^*$ for k_T range 0.2-0.5 GeV/ c . Figure from [5]

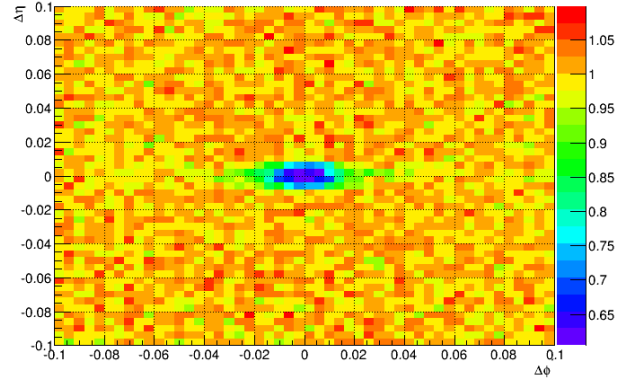


Figure 4.20: $DCA_{xy} < 2.4$ cm, $DCA_z < 3.0$ cm: Two dim. ratio $\Delta\eta\Delta\phi^*$ for k_T range 0.5-1.0 GeV/ c . Figure from [5]

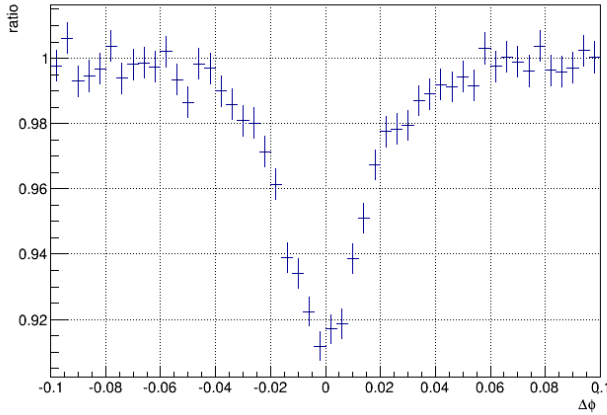


Figure 4.21: $DCA_{xy} < 2.4$ cm, $DCA_z < 3.0$ cm: $\Delta\phi^*$ projection for k_T range 0.2-0.5 GeV/ c . Figure from [5]

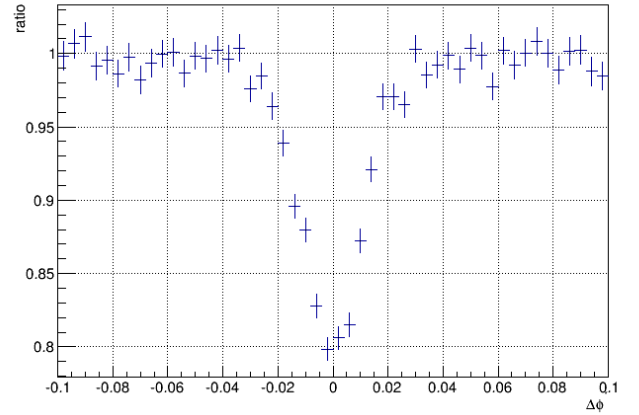


Figure 4.22: $DCA_{xy} < 2.4$ cm, $DCA_z < 3.0$ cm: $\Delta\phi^*$ projection for k_T range 0.5-1.0 GeV/ c . Figure from [5]

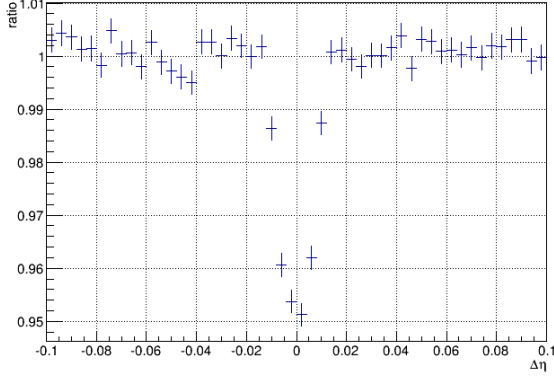


Figure 4.23: $DCA_{xy} < 2.4$ cm, $DCA_z < 3.0$ cm: $\Delta\eta$ projection for k_T range 0.2-0.5 GeV/c. Figure from [5]

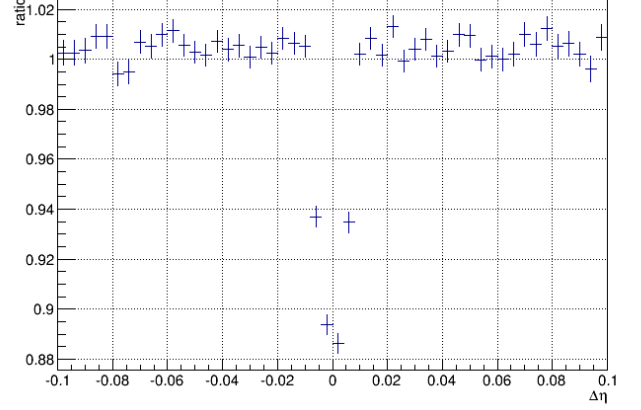


Figure 4.24: $DCA_{xy} < 2.4$ cm, $DCA_z < 3.0$ cm: $\Delta\eta$ projection for k_T range 0.5-1.0 GeV/c. Figure from [5]

$$C(q, k) = 1 + \lambda(k) \exp(-q_{inv}^2 R_{inv}^2(k)) \quad (4.11)$$

where $q_{inv}^2 = q^2 - q_0^2$ is the square of the spatial relative momentum in the pair rest frame $q_0 = 0$.

We used the three DCA_{xy} & DCA_z values from Table 4.2 and vary the $\Delta\eta$ & $\Delta\phi^*$ values (table 4.3). Figure 4.25 - 4.30 show the correlation function for different DCA cuts and pair cuts. The best cuts selections criteria are based on the assumption that the correlation function is unity (MC data). Any divergence from 1 is an indication of track splitting and merging effect. Based on this selection criteria, it is clear from figure 4.30 that the best cuts will be $\Delta\eta = 0.015$ & $\Delta\phi^* = 0.017$ for $DCA_{xy} = 2.4$ cm & $DCA_z = 3.0$ cm.

Table 4.3: $\Delta\eta$ and $\Delta\phi^*$ cuts

$\Delta\phi^*$	$\Delta\eta$
0	0
0.017	0.015
0.04	0.02
0.06	0.02

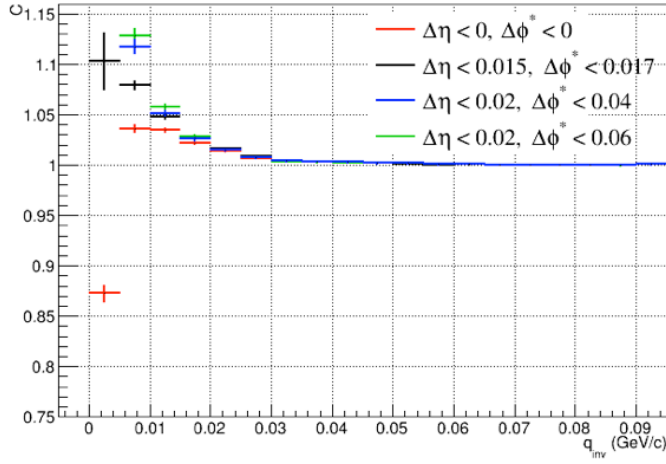


Figure 4.25: $DCA_{xy} < 0.2$ cm, $DCA_z < 0.15$ cm: $C(q_{inv})$ for k_T range 0.2-0.5 GeV/c. Figure from [5]

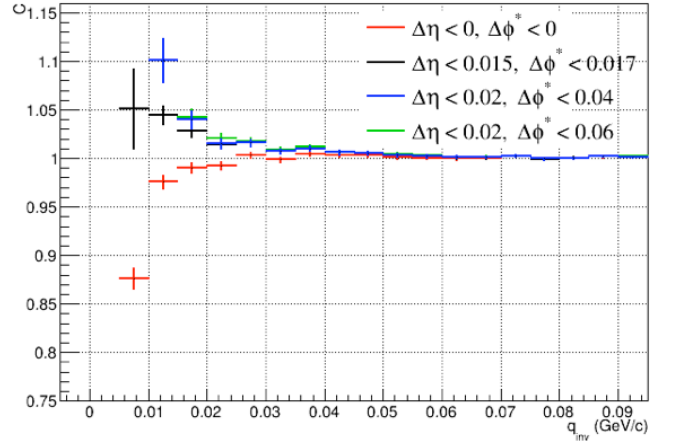


Figure 4.26: $DCA_{xy} < 0.2$ cm, $DCA_z < 0.15$ cm: $C(q_{inv})$ for k_T range 0.5-1.0 GeV/c. Figure from [5]

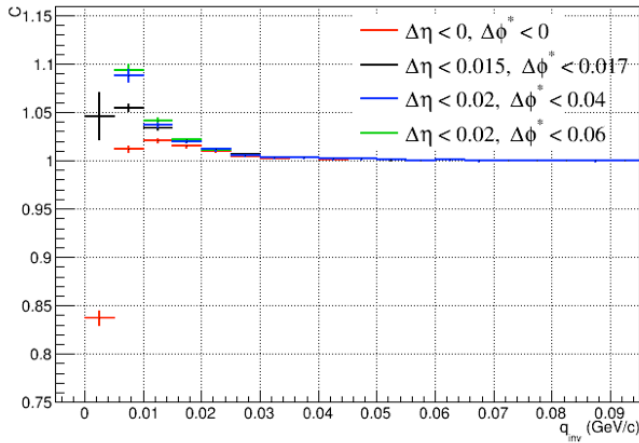


Figure 4.27: $DCA_{xy} < 0.4$ cm, $DCA_z < 0.3$ cm: $C(q_{inv})$ for k_T range 0.2-0.5 GeV/c. Figure from [5]

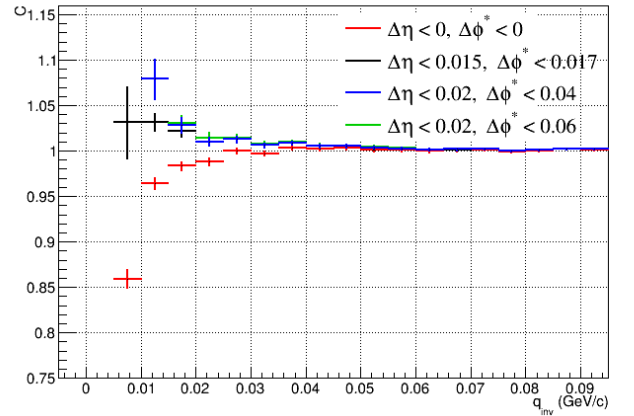


Figure 4.28: $DCA_{xy} < 0.4$ cm, $DCA_z < 0.3$ cm: $C(q_{inv})$ for k_T range 0.5-1.0 GeV/c. Figure from [5]

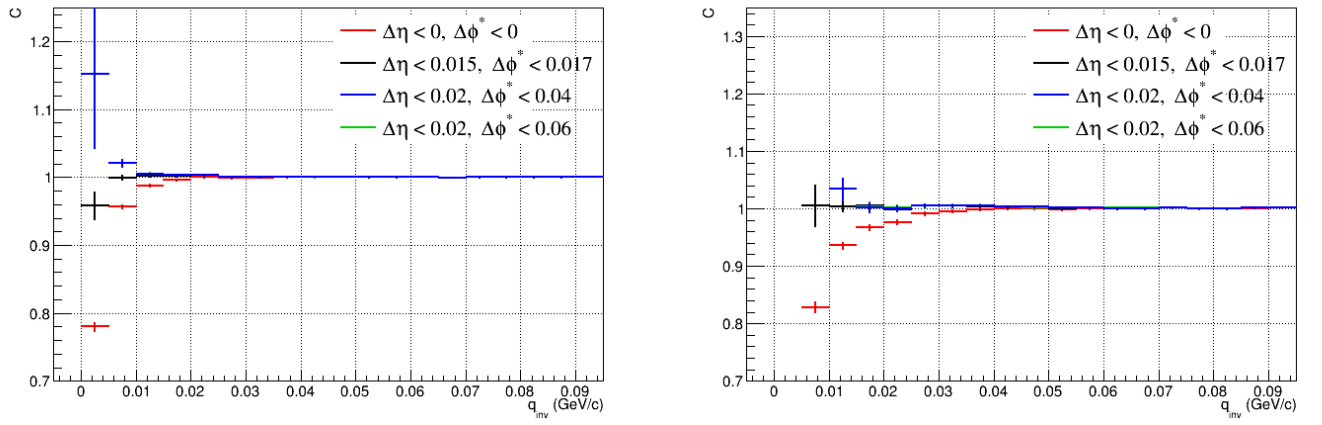


Figure 4.29: $DCA_{xy} < 2.4$ cm, $DCA_z < 3.0$ cm: $C(q_{inv})$ for k_T range 0.2-0.5 GeV/c. Figure from [5]

Figure 4.30: $DCA_{xy} < 2.4$ cm, $DCA_z < 3.0$ cm: $C(q_{inv})$ for k_T range 0.5-1.0 GeV/c. Figure from [5]

4.3 Azimuthal HBT Results w.r.t second harmonic

4.3.1 Pb-Pb 2.76 TeV Results

Once the event plane is determined, the HBT analysis is performed in 9 bins of the pair emission angle with respect to second harmonic event plane ($\Psi_{EP,2}$), where $\varphi_{pair} - \Psi_{EP,n}$ ranges are: $-9^\circ, 9^\circ, 27^\circ, 45^\circ, 63^\circ, 81^\circ, 99^\circ, 117^\circ, 135^\circ, 153^\circ, 171^\circ$. There are six centrality classes used in this analysis: 0 – 5%, 5 – 10%, 10 – 20%, 20 – 30%, 30 – 40%, and 40 – 50%, and four k_T ranges, 0.2–0.3 GeV/ c , 0.3–0.4 GeV/ c , 0.4–0.5 GeV/ c , and 0.5–0.7 GeV/ c .

4.3.1.1 Radii Oscillation

In case of an anisotropic source, the transverse radii oscillate relative to the pair emission angle. To investigate the angular dependence, we fit the radii with the following formulas [26]:

$$\begin{aligned}
 R_{out}^2(\varphi_{pair} - \Psi_{EP,n}) &= R_{out,0}^2 + 2R_{out,2}^2 \cos(n(\varphi_{pair} - \Psi_{EP,n})) \\
 R_{side}^2(\varphi_{pair} - \Psi_{EP,n}) &= R_{side,0}^2 + 2R_{side,2}^2 \cos(n(\varphi_{pair} - \Psi_{EP,n})) \\
 R_{long}^2(\varphi_{pair} - \Psi_{EP,n}) &= R_{long,0}^2 + 2R_{long,2}^2 \cos(n(\varphi_{pair} - \Psi_{EP,n})) \\
 R_{outside}^2(\varphi_{pair} - \Psi_{EP,n}) &= 2R_{outside,2}^2 \sin(n(\varphi_{pair} - \Psi_{EP,n}))
 \end{aligned} \tag{4.12}$$

where n represents the harmonic number.

4.3.1.2 HBT radii vs. Azimuthal Angle

Centrality dependence

Figure 4.31 presents the dependence of R_{out}^2 , R_{side}^2 , R_{long}^2 , R_{os}^2 , and λ on the pion emission angle relative to the second harmonic event plane. The results are shown for one k_T range 0.3–0.4 GeV/ c and six centrality classes 0–5%, 5–10%, 10–20%, 20–30%, 30–40%, and 40–50%. R_{out}^2 and R_{side}^2 exhibit clear out-of-phase oscillations. The three HBT radii (R_{out}^2 , R_{side}^2 , R_{long}^2 , R_{os}^2) decrease from central to peripheral events. No oscillations for R_{long}^2 and λ are observed within the uncertainties of the measurement. The parameter R_{os}^2 shows very similar oscillations for all centrality classes. R_{ol}^2 and R_{sl}^2 are found to be consistent with zero. The bands indicate the systematic errors. The systematic studies will be presented in the next sections.

k_T dependence

Figure 4.32 presents the dependence of R_{out}^2 , R_{side}^2 , R_{long}^2 , R_{os}^2 , and λ on the pion emission angle relative to the second harmonic event plane. The results are shown for the centrality classes 20–30% in four ranges of k_T : 0.2–0.3, 0.3–0.4, 0.4–0.5, and 0.5–0.7 GeV/ c . R_{out}^2 and R_{side}^2 exhibit clear out-of-phase oscillations. No oscillations for R_{long}^2 and λ are observed within the uncertainties of the measurement. The parameter R_{os}^2 shows very similar oscillations for all k_T bins. R_{ol}^2 and R_{sl}^2 are found to be consistent with zero, as expected due to symmetry, and are not further investigated in this analysis. A possible correlation between λ and the extracted radii was checked by fixing λ . No change in the radii has been observed.

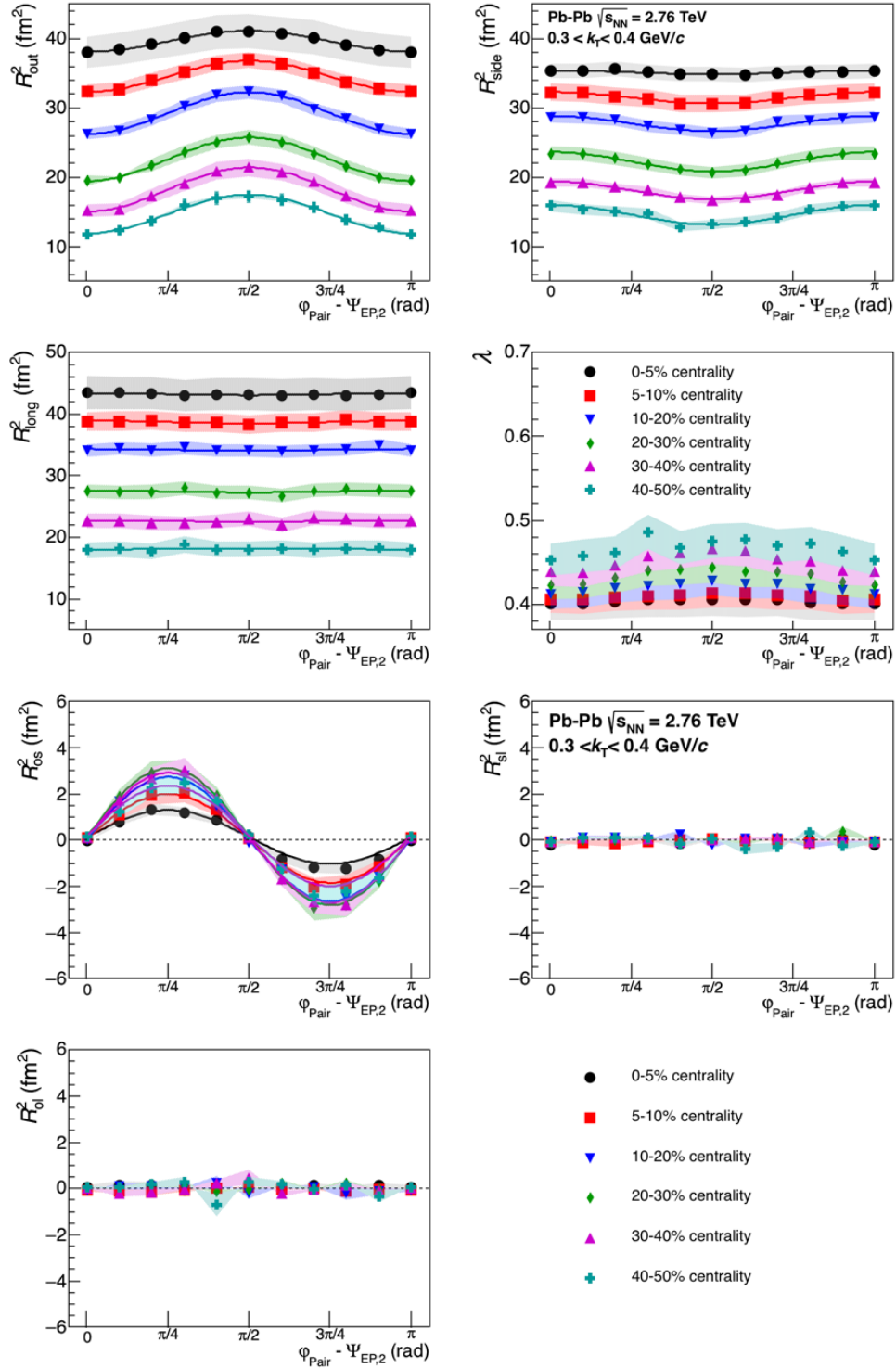


Figure 4.31: The azimuthal dependence of R_{out}^2 , R_{side}^2 , R_{long}^2 , R_{os}^2 , and λ as a function of $\Delta\varphi = \varphi_{\text{pair}} - \Psi_{\text{EP},2}$ for one k_T range 0.3–0.4 GeV/c and six centrality classes 0–5%, 5–10%, 10–20%, 20–30%, 30–40%, and 40–50%. Bands indicate the systematic errors. The results are not corrected for the event plane resolution of about 85–95%.

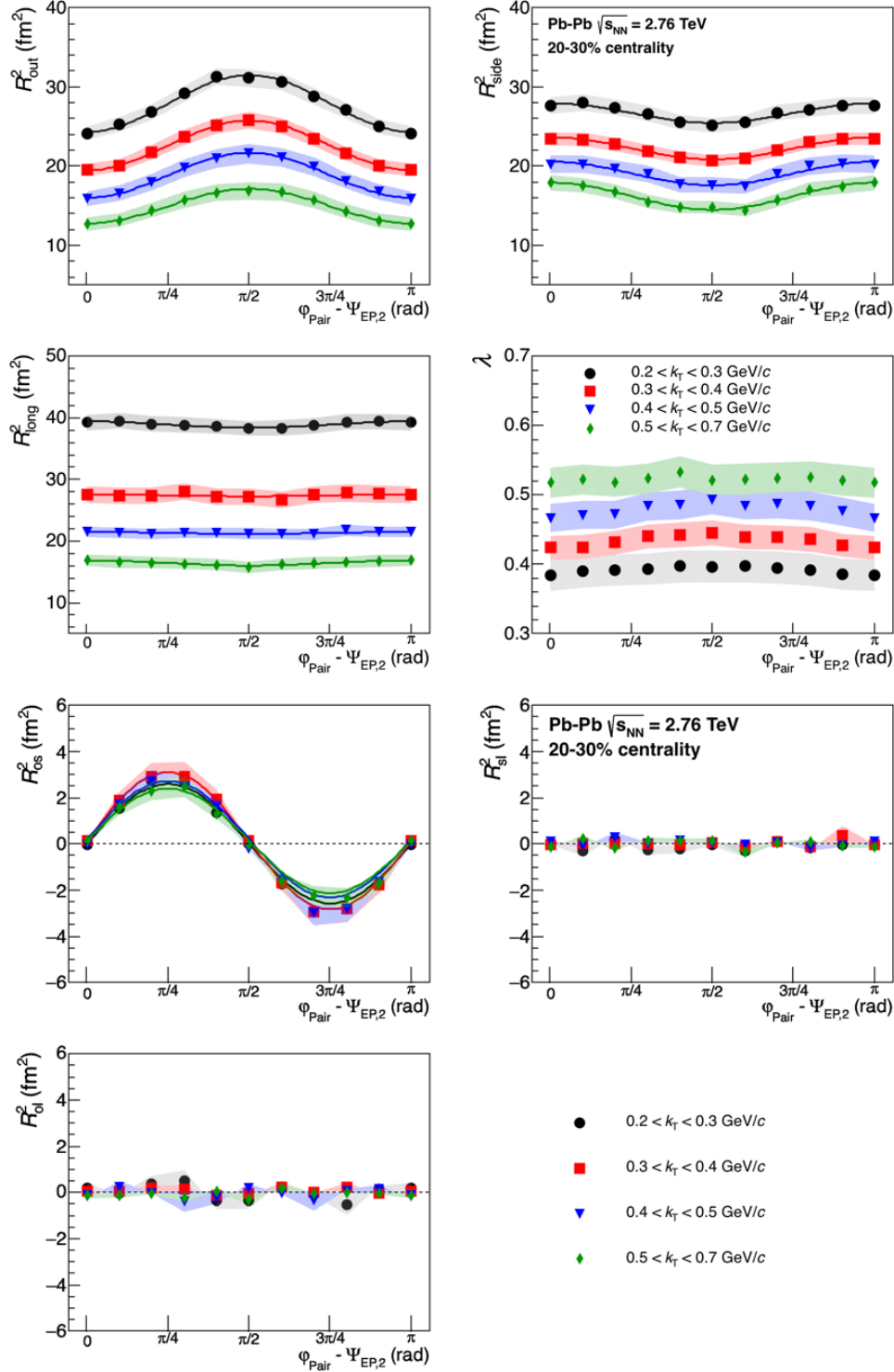


Figure 4.32: The azimuthal dependence of R_{out}^2 , R_{side}^2 , R_{long}^2 , R_{os}^2 , and λ as a function of $\Delta\varphi = \varphi_{\text{pair}} - \Psi_{\text{EP},2}$ for the centrality 20–30% and k_{T} ranges 0.2–0.3, 0.3–0.4, 0.4–0.5, and 0.5–0.7 GeV/c. Bands indicate the systematic errors. The results are not corrected for the event plane resolution of about 85–95%.

4.3.1.3 Average Radii and Amplitudes of Oscillations

Average Radii compared with 3+1D Hydro: $R_{i,0}^2$

Fitting the radii's azimuthal dependence with the functional form of Eq. 4.3.1.1 allows us to extract the average radii and the amplitudes of oscillations. The latter have to be corrected for the finite event plane resolution. There exist several methods for such a correction [4], which produce very similar results [36] well within errors of this analysis. The results shown below have been obtained with the simplest method first used by the E895 Collaboration [31], in which the amplitude of oscillation is divided by the event plane resolution factor. The correction is about 5–15%, depending on centrality. Figure 4.33 shows the average radii for different k_T values as a function of centrality. The average radii obtained in this analysis are consistent with the results reported in [7]. As expected, the radii are larger in more central collisions and at smaller k_T values, the latter reflecting the effect of radial flow [4, 52]. The cross-term $R_{os,0}^2$ is consistent with zero, as expected due to the symmetry of the system. The 3+1D hydrodynamic calculations [6], while correctly describing the qualitative features of the average radii dependence on centrality and k_T , fail to describe our results quantitatively.

Relative Amplitudes of Oscillations: $R_{i,2}^2/R_{i,0}^2$ Figure 4.34 shows the relative amplitudes of the radius oscillations $R_{out,2}^2/R_{side,0}^2$, $R_{side,2}^2/R_{side,0}^2$, $R_{long,2}^2/R_{long,0}^2$, and $R_{os,2}^2/R_{side,0}^2$. When comparing our results to the ones obtained by the STAR experiment, we observe similar relative oscillations, however STAR results [9, 39] show on average larger oscillations for $R_{side,2}^2$. Our relative amplitudes for $R_{out,2}^2/R_{side,0}^2$, $R_{side,2}^2/R_{side,0}^2$, and $R_{os,2}^2/R_{side,0}^2$ show a clear centrality dependence, that is an increase for more peripheral events, whereas the $R_{long,2}^2/R_{long,0}^2$ is very close to zero for all centralities, similarly to the results from RHIC [36, 39, 53].

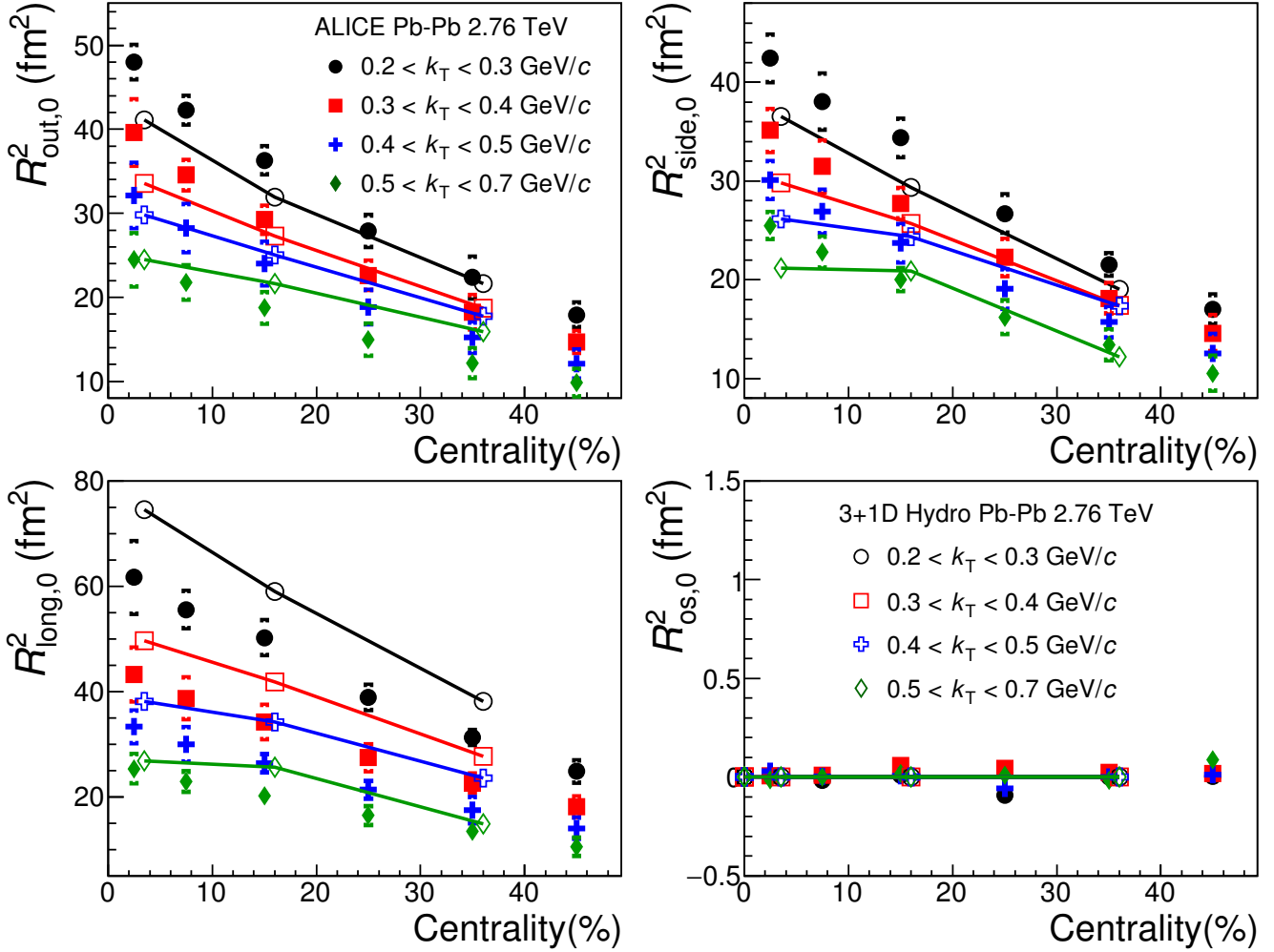


Figure 4.33: The average radii $R_{\text{out},0}^2$, $R_{\text{side},0}^2$, $R_{\text{long},0}^2$, and $R_{\text{os},0}^2$ as a function of centrality for different k_T ranges compared to hydrodynamical calculations [6]. Square brackets indicate the systematic errors.

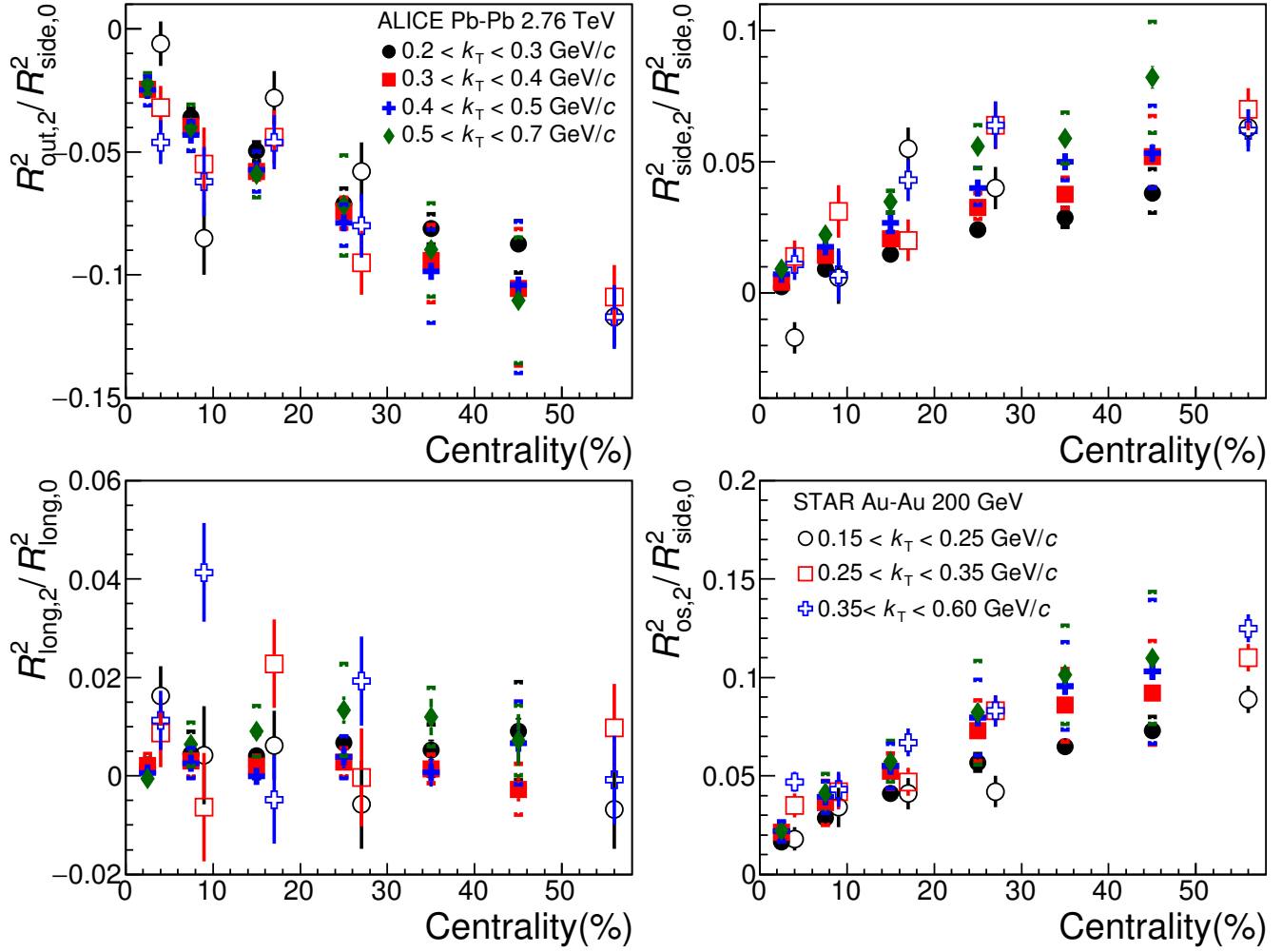


Figure 4.34: Amplitudes of the relative radius oscillations $R^2_{\text{out},2}/R^2_{\text{side},0}$, $R^2_{\text{side},2}/R^2_{\text{side},0}$, $R^2_{\text{long},2}/R^2_{\text{long},0}$, and $R^2_{\text{os},2}/R^2_{\text{side},0}$ versus centrality for the k_T ranges 0.2–0.3, 0.3–0.4, 0.4–0.5, and 0.5–0.7 GeV/ c . The error bars indicate the statistical uncertainties and the square brackets show the systematic errors. The STAR data points, for 0–5%, 5–10%, 10–20%, 20–30% and 30–80% Au–Au collisions, are slightly shifted for clarity.

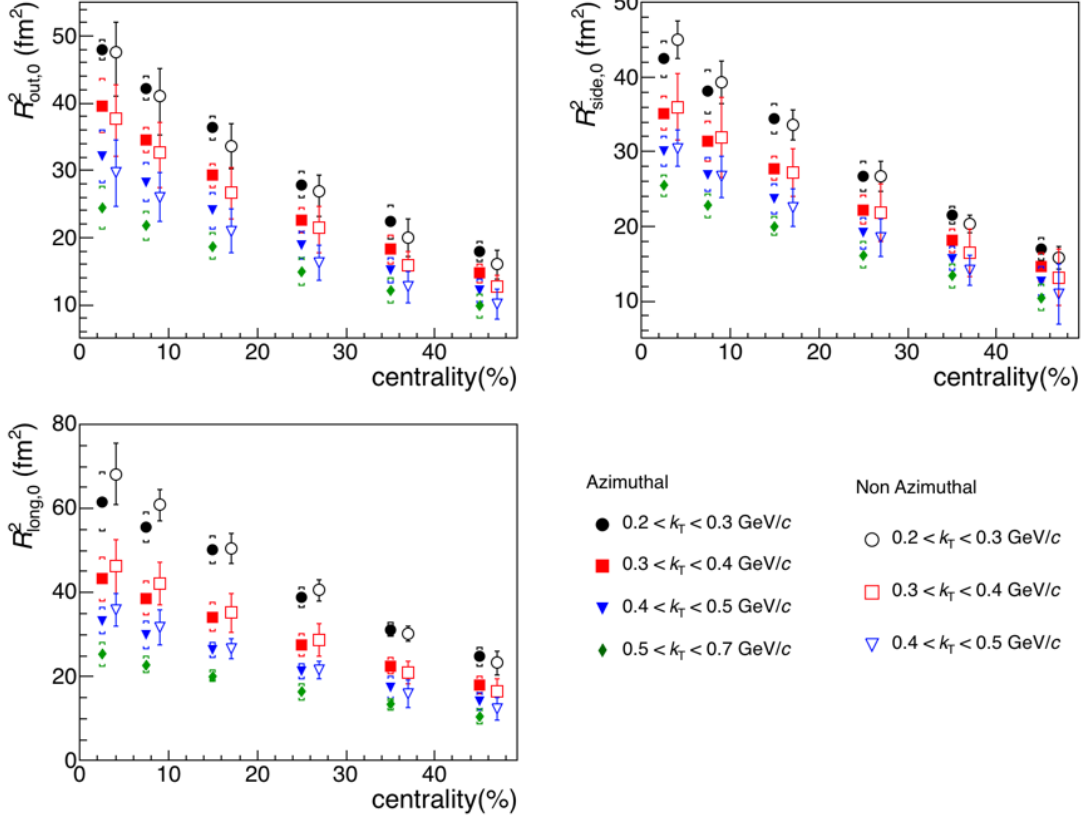


Figure 4.35: Centrality and k_T dependence of R_{out} , R_{side} and R_{long} for azimuthally-differential and non-azimuthal pion femtoscopy in Pb-Pb collisions at 2.76 TeV vs non-azimuthal HBT analysis [7]. Points are shifted slightly in the x-direction for visibility. Closed symbols show the azimuthally-differential HBT results and open symbols show the non-azimuthal results. The square brackets and error bars are systematic errors.

4.3.1.4 Comparison with the Non-azimuthally Results

We compare our results for the average radii ($R_{i,0}^2$) with those obtained using non-azimuthally differential HBT analysis [7]. We expect the azimuthal and non-azimuthal results to be in agreement since $R_{i,0}^2$ has no angular dependence. We compare the results for six centrality classes and four k_T bins. Figure 4.35 shows a very good agreement between the two results for the three HBT radii within systematic errors.

4.3.1.5 Final Source Eccentricity

The source eccentricity is usually defined as $\varepsilon = (R_y^2 - R_x^2)/(R_y^2 + R_x^2)$, where R_x is the in-plane radius of the (assumed) elliptical source and R_y is the out-of-plane radius. As shown in [52] the relative amplitudes of side radii oscillations are mostly determined by the spatial source anisotropy and are less affected by dynamical effects such as velocity gradients. The source eccentricity at freeze-out $\varepsilon_{\text{final}}$ can be estimated from R_{side}^2 oscillations at small pion momenta with an accuracy within 20–30% as $\varepsilon_{\text{final}} \approx 2R_{\text{side},2}^2/R_{\text{side},0}^2$ [52].

Figure 4.36 presents $2R_{\text{side},2}^2/R_{\text{side},0}^2$ for different k_T ranges as a function of the initial-state eccentricity for six different centralities and four k_T bins. For the initial eccentricity we have used the nucleon participant eccentricity from the Monte Carlo Glauber model for both, Au–Au collisions at $\sqrt{s_{\text{NN}}} = 200$ GeV [35] and Pb–Pb collision at $\sqrt{s_{\text{NN}}} = 2.76$ TeV [8]. Our results for all k_T bins are significantly below the values of the initial eccentricity indicating a more intense expansion in the in-plane direction. Due to relatively large uncertainties of the RHIC results for narrow k_T bins, we compare our results only to the average STAR data [39] in $0.15 < k_T < 0.6$ GeV/ c and to PHENIX results [35] corresponding to $0.2 < k_T < 2.0$ GeV/ c ($\langle k_T \rangle = 0.53$ GeV/ c). We find a smaller final-state anisotropy in the LHC regime compared to RHIC energies. This trend is qualitatively consistent with expectations from hydrodynamic and transport models [37,38]. The final-state eccentricity remains positive also at the LHC, evidence of an out-of-plane elongated source at freeze-out. In Fig. 4.36, we also compare our results to the 3+1D hydrodynamic calculations [6], which were performed for similar centralities and k_T ranges as in the experiment. This model slightly underestimates the final source eccentricity.

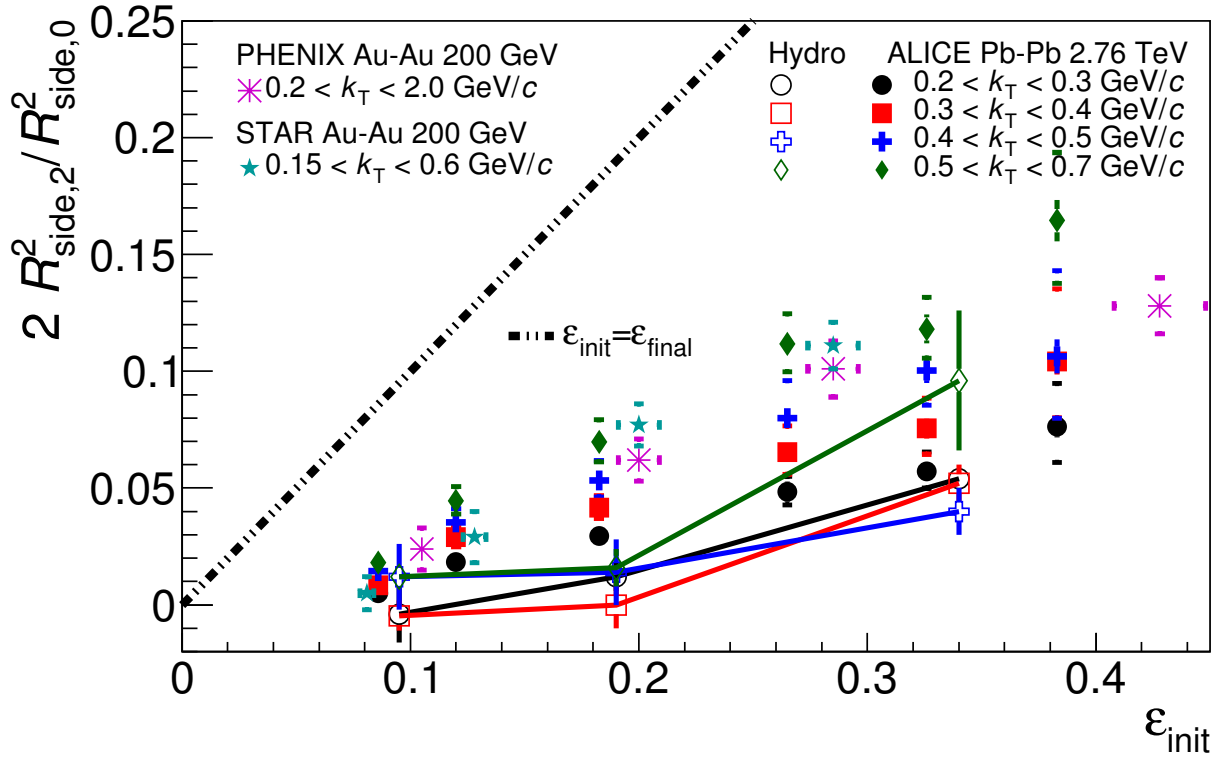


Figure 4.36: An estimate of freeze-out eccentricity $2R_{\text{side},2}^2/R_{\text{side},0}^2$ for different k_T ranges vs. initial state eccentricity from Monte Carlo Glauber model [8] for six centrality ranges, 0–5%, 5–10%, 10–20%, 20–30 %, 30–40 %, and 40–50%. The dashed line indicates $\epsilon_{\text{final}} = \epsilon_{\text{init}}$. Square brackets indicate systematic errors.

4.3.2 Pb-Pb 5.02 TeV Results

In the previous section, we showed the results for Pb-Pb at $\sqrt{s_{\text{NN}}} = 2.76$ TeV. In this section, we show a preliminary results for Pb-Pb at $\sqrt{s_{\text{NN}}} = 5.02$ TeV. We show the effect of using higher energy on the HBT radii.

4.3.2.1 Average Radii Comparison between 2.76 TeV and 5.02 TeV

Figure 4.37 shows the comparison between the results from different collision energies. The average radii $R_{\text{out},0}$ and $R_{\text{side},0}$ are similar for both energies, no significant difference was observed. The average radii for $R_{\text{long},0}$ is slightly larger for higher energy.

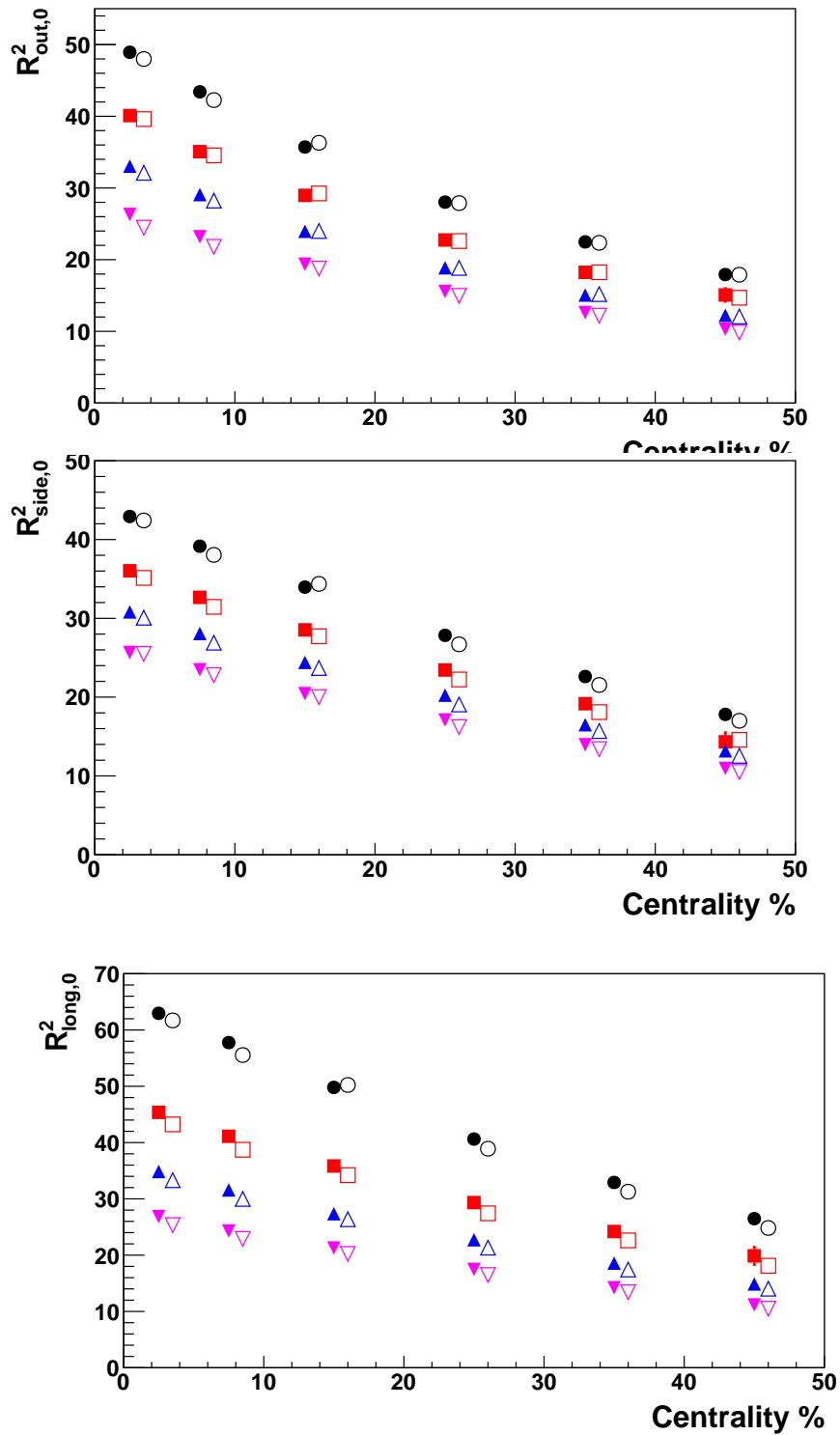


Figure 4.37: Comparison between the average radii from two different energies. The open markers are for 2.76 TeV energy, whereas the closed symbols are for 5.02 TeV energy.

4.3.2.2 Amplitudes of Oscillations for Pb-Pb 5.02 TeV

In figure 4.38, the relative amplitudes for $R_{\text{out},2}^2/R_{\text{side},0}^2$, $R_{\text{side},2}^2/R_{\text{side},0}^2$, and $R_{\text{os},2}^2/R_{\text{side},0}^2$ show a clear centrality dependence, that is an increase for more peripheral events, whereas the $R_{\text{long},2}^2/R_{\text{long},0}^2$ is very close to zero for all centralities. All the relative amplitudes show a weak dependence on k_T . This dependence is similar to the one observed in figure 4.34 for lower energy. This analysis is still in progress and a systematic studies is needed. At this point, based on the obtained results for $R_{\text{side},2}^2/R_{\text{side},0}^2$ amplitudes of oscillations, we infer that we don't have any difference in the final source shape (final eccentricity) for higher collision energy (5.02 TeV).

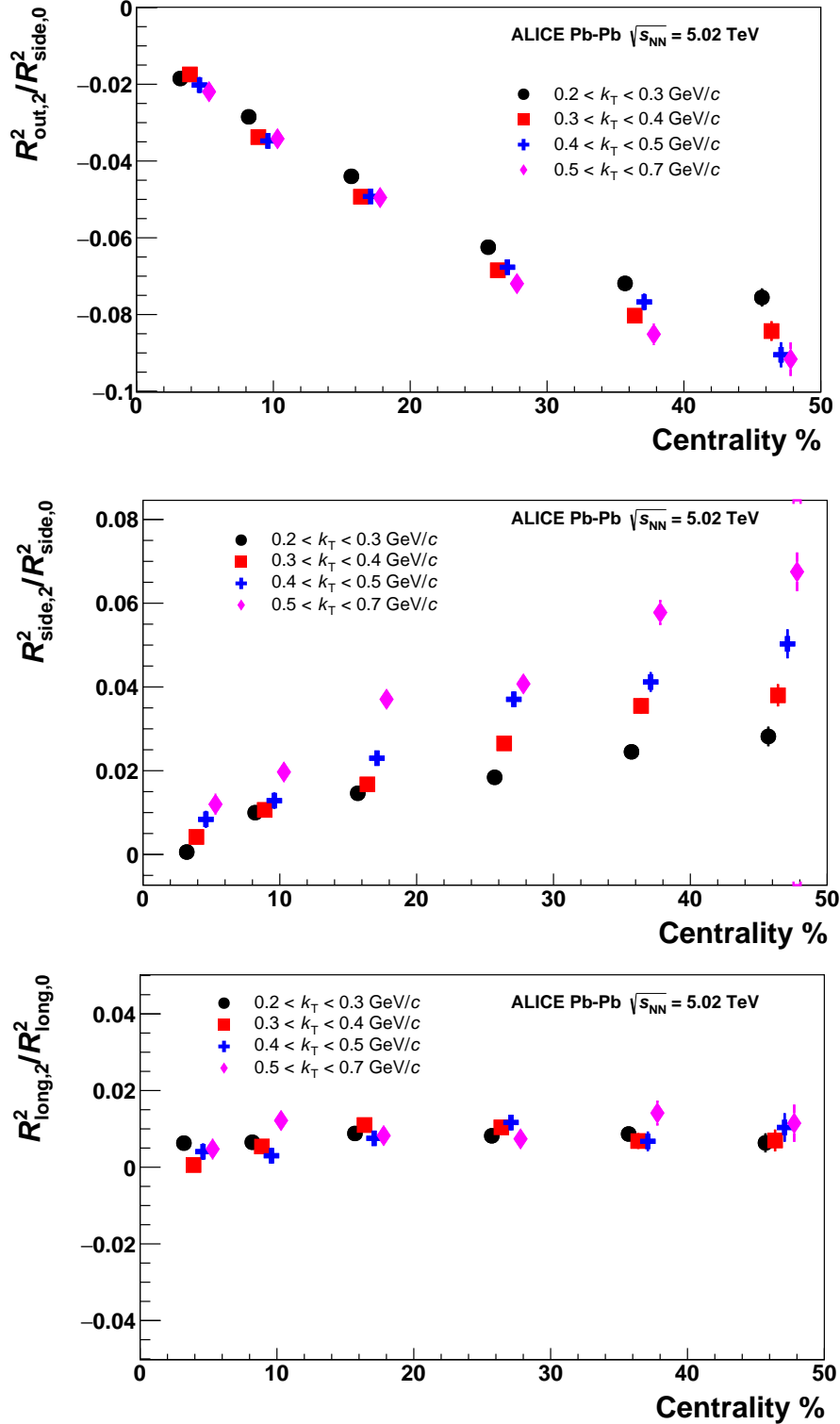


Figure 4.38: Amplitudes of the relative radius oscillations $R_{out,2}^2/R_{side,0}^2$, $R_{side,2}^2/R_{side,0}^2$, $R_{long,2}^2/R_{long,0}^2$, and $R_{os,2}^2/R_{side,0}^2$ versus centrality for the k_T ranges 0.2–0.3, 0.3–0.4, 0.4–0.5, and 0.5–0.7 GeV/c. The error bars indicate the statistical uncertainties.

4.3.3 Corrections

4.3.3.1 Coulomb Correction

To isolate the Bose-Einstein contribution in the correlation function, effects due to final-state Coulomb repulsion must be taken into account. For that, the Bowler-Sinyukov fitting procedure [46, 54] was used in which the Coulomb weight is only applied to the fraction of pairs (λ) that participate in the Bose-Einstein correlation. In this approach, the correlation function is fitted to

$$C(\mathbf{q}, \Delta\varphi) = N[(1 - \lambda) + \lambda K(\mathbf{q}_{inv})(1 + G(\mathbf{q}, \Delta\varphi))], \quad (4.13)$$

where N is the normalization factor. The function $G(\mathbf{q}, \Delta\varphi)$ describes the Bose-Einstein correlations and $K(\mathbf{q}_{inv})$ is the Coulomb part of the two-pion wave function integrated over a source function corresponding to $G(\mathbf{q})$. The Coulomb correction used in this analysis is obtained from the analytic solution of the wave function described in chapter 2. For different centrality classes, different $K(\mathbf{q}_{inv})$ values were used since the size of the Gaussian source depended on the centrality. Figure 4.39 shows the dependence of $K(\mathbf{q}_{inv})$ on q_{inv} used for the centrality class 0–5%.

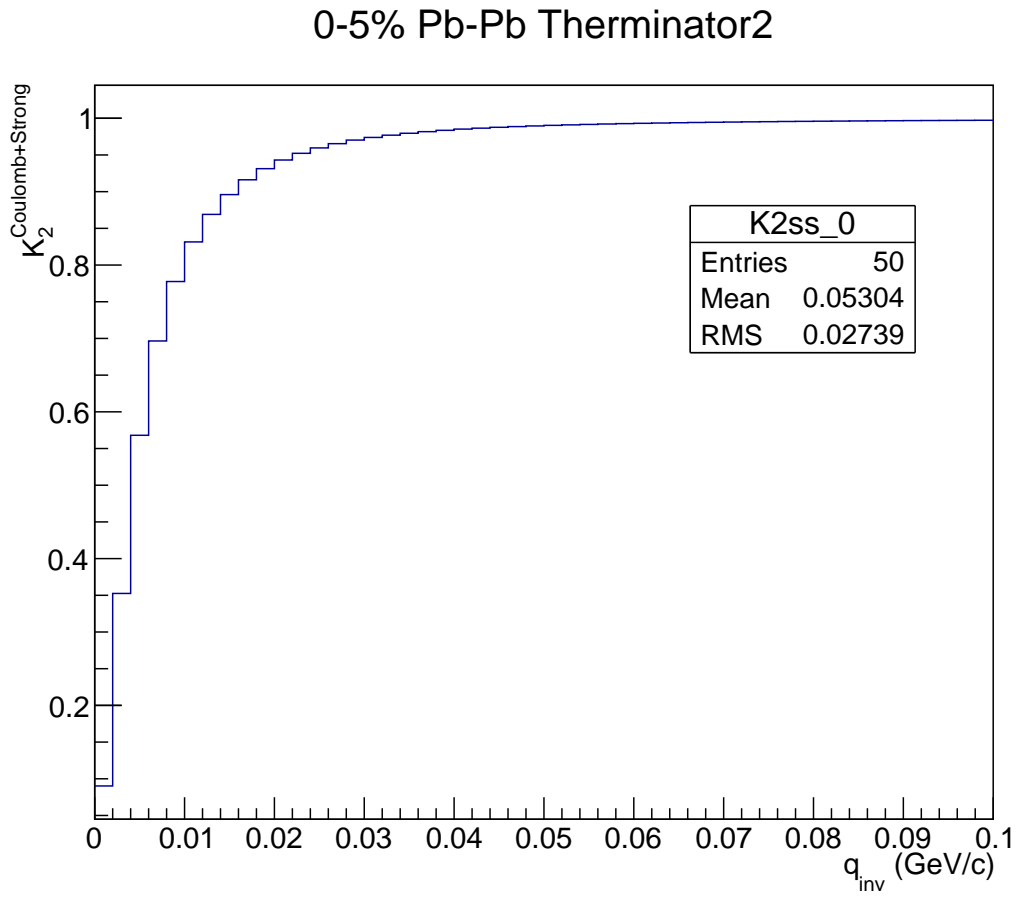


Figure 4.39: Squared Coulomb wave function integrated over a source of centrality class 0-5%.

4.3.3.2 Event Plane Resolution Correction

Finite event plane resolution smears the oscillation of azimuthally sensitive HBT with respect to the event plane. A model independent correction is applied in this analysis. Real and mixed q-distribution are corrected with the following equation. The correction for the numerator is the following:

$$N(q, \phi_j) = N_{exp}(q, \phi_j) + 2 \left(\sum_{n=1}^{n_{bins}} \xi_{n,m}(\Delta) [N_{c,n}^{exp}(q) \cos(n\phi_j) + N_{s,n}^{exp}(q) \sin(n\phi_j)] \right), \quad (4.14)$$

where N_{exp} is the experimentally distribution. The decompositions are:

$$N_{c,n}^{exp}(q) = \langle N_{exp}(q, \phi_j) \cos(n\phi) \rangle = \frac{1}{n_{bins}} \sum_{n=1}^{n_{bins}} N_{exp}(q, \phi_j) \cos(n\phi_j), \quad (4.15)$$

$$N_{s,n}^{exp}(q) = \langle N_{exp}(q, \phi_j) \sin(n\phi) \rangle = \frac{1}{n_{bins}} \sum_{n=1}^{n_{bins}} N_{exp}(q, \phi_j) \sin(n\phi_j). \quad (4.16)$$

The correction factor ξ is:

$$\xi_{n,m}(\Delta) = \frac{n\Delta/2}{\sin(n\Delta/2)R_{EP}}, \quad (4.17)$$

where Δ is the bin width used in the analysis and R_{EP} is the measured event plane resolution.

Figure 4.40 shows the measured event plane resolution, obtained using the TPC detector, dependence on centrality. However, figure 4.41 shows the comparison between event plane resolution corrected and uncorrected result of the extracted HBT radii. Event plane is determined using the TPC detector. Therefore event plane resolution in Figure 4.40 is used. Event plane resolution correction does not change the average HBT radii. The amplitudes of oscillations became a little larger due to the event plane resolution correction. Solid lines shows the fit function. There is another method to correct the amplitudes of

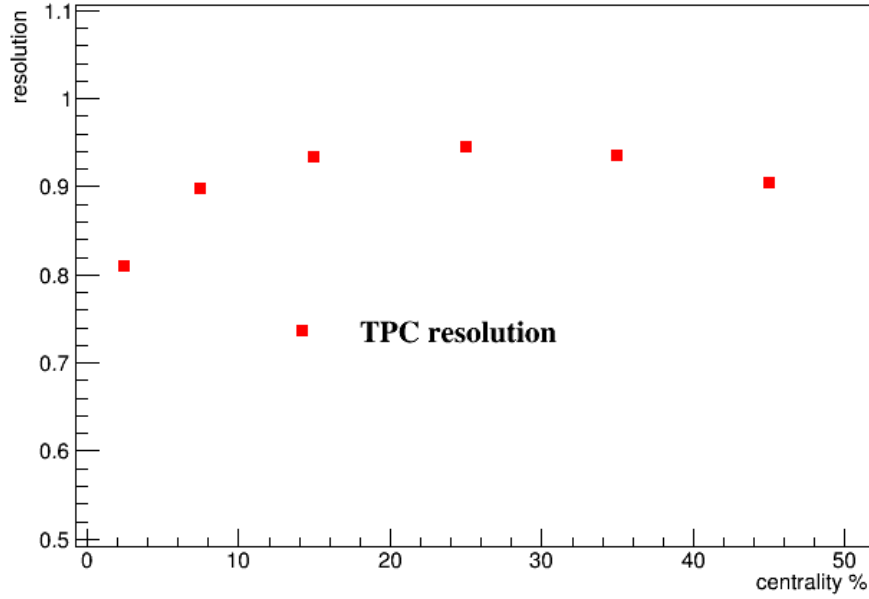


Figure 4.40: Event plane resolution using the TPC dependence on centrality.

oscillations of the HBT radii. This method is much more simple one and first used by the E895 Collaboration [31] which is expressed as:

$$R_{i,j,true}^2 = R_{i,j,measured}^2 / \rho \quad (4.18)$$

$$\rho = \langle \cos(n(\psi - \Phi_n)) \rangle,$$

where $R_{i,j,measured}^2$ denotes the measured oscillation amplitude of squared HBT radii, $R_{i,j,true}^2$ is the corrected amplitude of oscillation of the HBT radii, n is the harmonic number, and $\langle \cos(n - \Psi_n) \rangle$ is the event plane resolution.

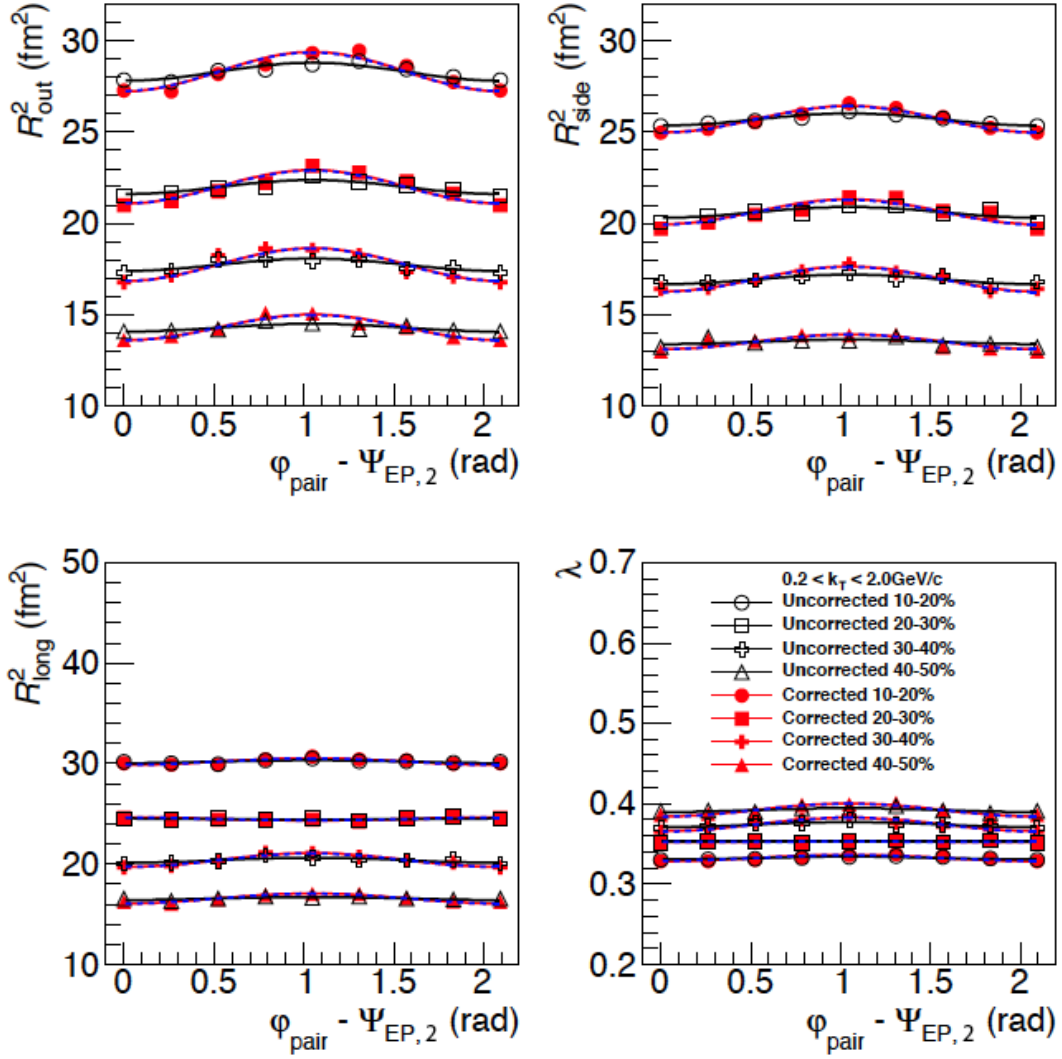


Figure 4.41: HBT radii of charged pions as a function of azimuthal pair angle. Comparison before and after the event plane resolution correction.

4.3.4 Systematic Uncertainty

In this analysis, there were multiple variables to consider for the systematic uncertainties. They are listed in Table 4.4. The variables are: different pair cuts, the $\Delta\eta$, $\Delta\phi^*$ cuts described in Table 4.3, the DCA cuts, mentioned in Table 4.2, q-fit ranges, which is the fit range used varied from 80 MeV to 140 MeV, pion charges (positive and negative pairs), the difference between positive and negative magnetic field, and event plane estimation using different detectors (difference between the TPC and the VZero event planes).

4.3.4.1 q-fit Range

Figure 4.42 shows the modulation for the three HBT radii using four different q-fit ranges. We have a clear saturation in the modulations starting from $q_{range} = 120$ MeV. For different centralities and k_T bins, we used different q-fit range as the radii modulation saturates at different q-fit ranges. A systematic study was done and included in the systematic table.

Table 4.4: Systematic Table

		0–5%			5–10%			10–20%		
	k_T bin	R_{out}	R_{side}	R_{long}	R_{out}	R_{side}	R_{long}	R_{out}	R_{side}	R_{long}
pair cut	0	0.1%	0.02%	1%	0.3%	0.5%	1%	1%	1%	1%
	1	4%	0.5%	1%	0.5%	2%	4%	1%	1%	1%
	2	5%	0.4%	1%	3%	0.6%	0.9%	3%	1%	1%
	3	5%	0.5%	1%	4%	0.9%	1%	4%	1%	1%
dca cut	0	0.1%	1%	1%	1%	0.9%	2%	1%	1%	1%
	1	2%	1%	2%	2%	0.4%	2%	2%	1%	2%
	2	3%	1%	3%	3%	0.2%	3%	3%	1%	2%
	3	3%	1%	3%	2%	0.2%	2%	2%	1%	2%
q range	0	1%	1%	1%	0.8%	1%	1%	1%	1%	1%
	1	2%	1%	2%	0.8%	2%	1%	1%	1%	1%
	2	1%	1%	1%	0.3%	1%	1%	1%	2%	2%
	3	1%	1%	1%	0.5%	1%	1%	1%	2%	2.5%
charge	0	0.2%	1%	1%	1%	2%	1%	1%	2%	1%
	1	0.5%	1%	1%	1%	1%	1%	1%	1%	1%
	2	1%	2%	2%	2%	4%	4%	3%	1%	2%
	3	1%	1%	1%	1%	2%	3%	1%	1%	1%
B field	0	2%	1%	5%	1%	2%	2%	1%	1%	2%
	1	2%	2%	2%	1%	3%	1%	1%	1%	4%
	2	2%	2%	2%	2%	1%	2%	1%	3%	1%
	3	2%	2%	2%	1%	2%	2%	1%	2%	1%
Event Plane	0	0.5%	2%	2%	1%	1%	0.5%	1%	1%	2%
	1	1%	2%	5%	0.6%	2%	1%	1%	2%	1%
	2	1.5%	1%	2%	3%	1%	1%	1%	2%	1%
	3	2%	1%	4%	1%	2%	1%	2%	1%	1%
Total	0	2.3%	2.8%	5.7%	2.3%	3.3%	3.4%	2.4%	3.0%	3.5%
	1	4.9%	3.4%	5.9%	3.3%	4.3%	5.2%	3.0%	3.0%	4.9%
	2	6.5%	3.3%	4.8%	6%	4.3%	5.6%	5.5%	4.5%	3.9%
	3	6.6%	2.9%	5.7%	4.9%	3.6%	4.8%	5.2%	3.5%	3.8%

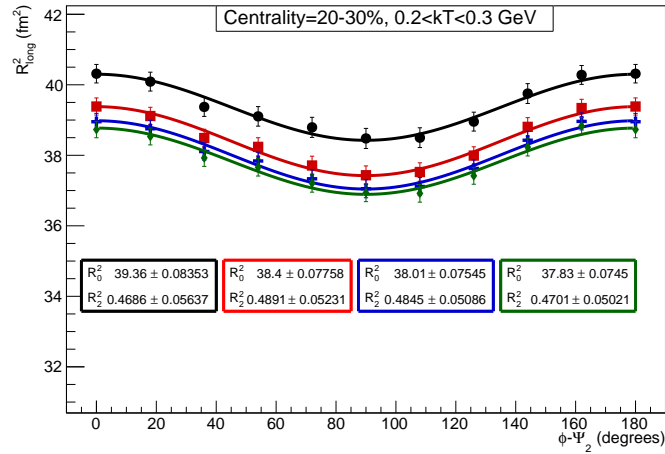
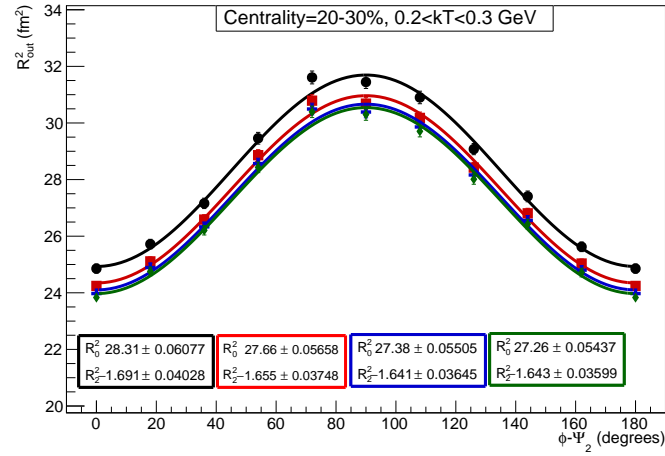
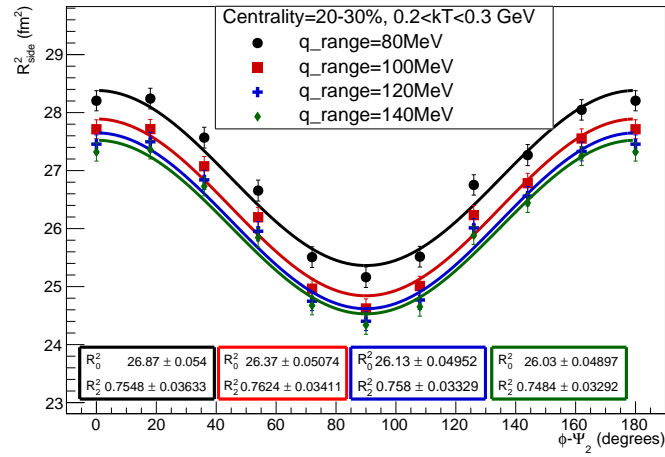


Figure 4.42: Radii modulations dependence on the q-fit ranges.

Table 4.5: Systematic Table

		20–30%			30–40%			40–50%		
	k_T bin	R_{out}	R_{side}	R_{long}	R_{out}	R_{side}	R_{long}	R_{out}	R_{side}	R_{long}
pair cut	0	1%	1%	1%	1%	1%	1%	2%	2%	2%
	1	1%	1%	1%	1%	2%	2%	1%	2%	2%
	2	3%	1%	1%	2%	2%	2%	1%	2%	1%
	3	4%	1%	1%	3%	2%	2%	1%	1%	3%
dca cut	0	1%	1%	2%	1%	1%	1%	1%	1%	1%
	1	2%	1%	2%	3%	1%	2%	2%	2%	1%
	2	3%	1%	2%	3%	1%	1%	4%	0.2%	2%
	3	3%	1%	2%	2.5%	1%	1%	3%	1%	2%
q range	0	1%	2%	3%	3%	3%	4%	5%	5%	6%
	1	1%	3%	3%	3%	5%	5%	4%	6%	8%
	2	0.9%	4%	3%	4%	5%	6%	5%	6%	8%
	3	1%	3%	3.5%	4%	5%	5%	4%	5%	6%
charge	0	1%	3%	1%	2%	0.2%	1%	2%	1%	1%
	1	2%	2%	2.5%	1%	1%	1%	1%	1%	1%
	2	1%	2%	1.5%	1%	3%	5%	4%	3%	1%
	3	2%	4%	1.5%	1%	4%	1%	2%	4%	1%
B field	0	2%	1%	1.5%	3%	0.5%	0.5%	1%	3%	2%
	1	2%	2%	1%	4%	2%	2%	1%	4%	2%
	2	2%	4%	2%	4%	0.2%	1%	2%	5%	4%
	3	2%	2%	1%	3%	1%	1%	3%	5%	2%
Event Plane	0	2%	1%	1%	4%	1%	1%	2%	1%	2%
	1	1%	1%	3%	2%	2%	2%	2%	2%	3%
	2	2%	2%	1%	1%	2%	4%	1%	1%	3%
	3	2%	1%	4%	4%	1%	0.1%	5%	2%	5%
Total	0	3.5%	4.1%	4.3%	6.3%	3.5%	4.5%	6.2%	6.4%	7.1%
	1	3.9%	4.5%	5.5%	6.3%	6.2%	6.5%	5.2%	8.1%	9.1%
	2	5.3%	6.5%	4.6%	6.9%	6.6%	9.1%	7.9%	8.7%	9.7%
	3	6.2%	5.7%	6.0%	7.6%	6.9%	5.7%	8.0%	8.5%	8.9%

4.4 Azimuthal HBT for Third Harmonic Event Plane

The measurements of HBT radii with respect to the second harmonic event plane angle (Ψ_2) in the previous sections provided an information on the final shape of the system, which is found to become more spherical compared to the initial state due to stronger in-plane expansion [55]. In contrast, model studies have shown that the azimuthal dependence of the HBT radii relative to the third harmonic event plane angle (Ψ_3) can originate from the anisotropies in collective velocity gradients or the initial spatial anisotropy (triangular) [6,33,34]. The signs of the HBT radii relative to the third harmonic event plane angle oscillations constrain the origin of these oscillation [34]. The analysis in this section presented at the Quark matter 2017 conference where the conference preceding can be found in [56]

4.4.1 Overview

We had performed the azimuthal HBT analysis with respect to the second harmonic event plane. This analysis is very similar to what we had done for the second harmonic. We have used the same data set, triggers, track cuts, and pair cuts. Also we have used the TPC detector for event plane determination. We did check for any difference in the results if we use the VZERO detector for event plane determination. The difference in the two results was included in the systematics.

4.4.2 Event Plane

The TPC detector was used for event plane determination. Fig.4.43 shows the event plane resolution for the third harmonic event plane using two sub-event method. For two sub-event method, we split the events into two sub-events in eta region.

4.4.2.1 Binning

The event plane is first determined, then HBT analysis is performed in 10 bins of the pair emission angle with respect to the reaction plane: $-6^\circ, 6^\circ, 18^\circ, 30^\circ, 42^\circ, 54^\circ, 66^\circ, 78^\circ, 90^\circ, 102^\circ, 114^\circ, 126^\circ$. There are six bins of centrality: $0 - 5\%, 5 - 10\%, 10 - 20\%, 20 - 30\%, 30 - 40\%$, and $40 - 50\%$. There are also 4 k_T bin ranges ($0.2-0.3\text{GeV}/c, 0.3-0.4\text{GeV}/c, 0.4-0.5\text{GeV}/c, 0.5-0.7\text{GeV}/c$). In case of an anisotropic source, the transverse radii oscillate relative to

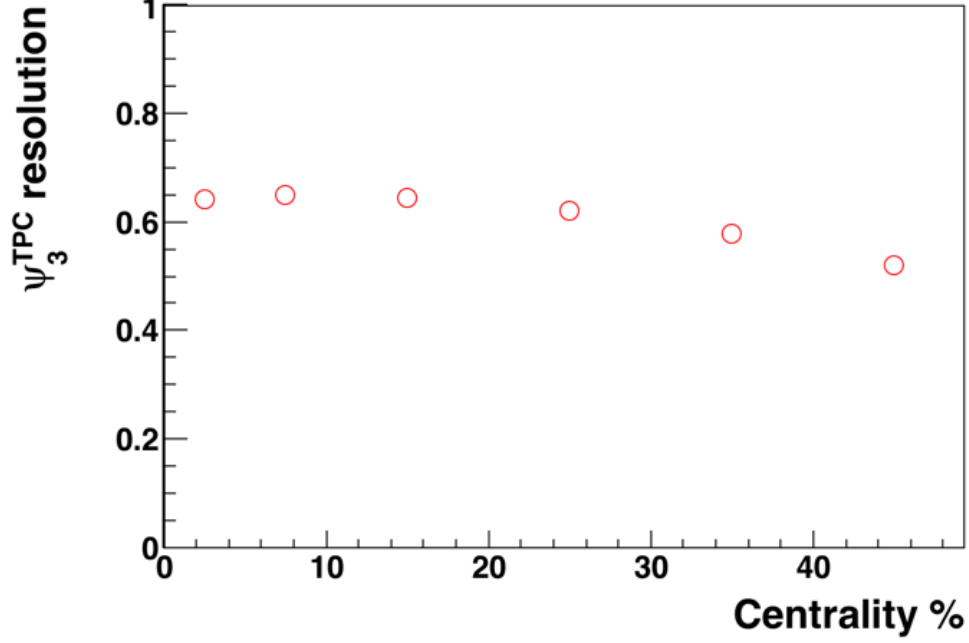


Figure 4.43: TPC third harmonic event plane resolution using two-subevent method

the pair emission angle. To investigate the angular dependence, we fit the radii with the following formulas (for $n = 3$) [26]:

$$\begin{aligned}
 R_{out}^2(\varphi_{pair} - \Psi_{EP,n}) &= R_{out,0}^2 + 2R_{out,n}^2 \cos(n(\varphi_{pair} - \Psi_{EP,n})) \\
 R_{side}^2(\varphi_{pair} - \Psi_{EP,n}) &= R_{side,0}^2 + 2R_{side,n}^2 \cos(n(\varphi_{pair} - \Psi_{EP,n})) \\
 R_{long}^2(\varphi_{pair} - \Psi_{EP,n}) &= R_{long,0}^2 + 2R_{long,n}^2 \cos(n(\varphi_{pair} - \Psi_{EP,n})) \\
 R_{outside}^2(\varphi_{pair} - \Psi_{EP,n}) &= 2R_{outside,n}^2 \sin(n(\varphi_{pair} - \Psi_{EP,n}))
 \end{aligned} \tag{4.19}$$

4.4.3 Results

4.4.3.1 Centrality dependence

Figure 4.44 shows the radii oscillations in one k_T range $0.2 < k_T < 0.3 \text{ GeV}/c$ for six centrality ranges. R_{out} and R_{side} radii show a clear radii oscillation. R_{long} oscillations is consistent with zero while R_{os} has small oscillation. As for second harmonic results the HBT radii (average radii) decrease from central to peripheral events.

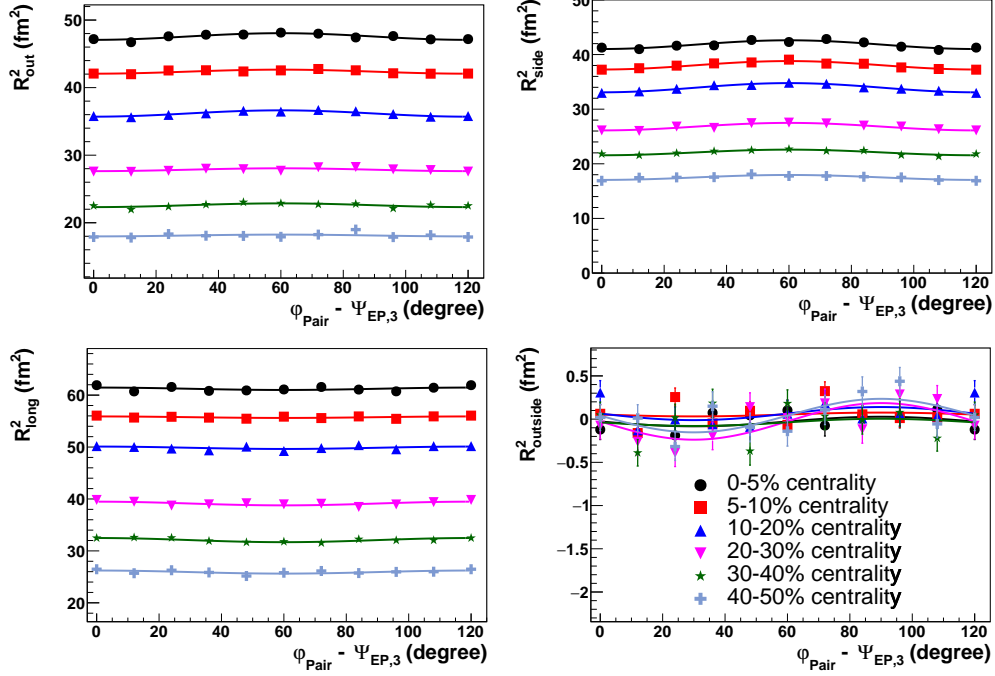


Figure 4.44: HBT radii oscillations in one k_T range $0.2 < k_T < 0.3$ for six centrality ranges.

4.4.3.2 k_T dependence

The k_T dependence at the centrality of 10–20% is shown in figure 4.45. As k_T increases, the radii decrease except R_{os} which doesn't show a k_T dependence.

4.4.3.3 Average Radii

The lines in figure 4.44 and figure 4.45 represent the fit to equation 4.19. Figure 4.46 shows the average radii from the third harmonic compared to the average radii from the second harmonic. The average radii don't depend on the event plane. As expected, figure show that the average radii obtained from the second harmonic (showed before) agree with the average radii from the third harmonic event plane.

4.4.4 Amplitudes of Oscillations

Figure 4.47 shows the oscillation parameters $R_{out,3}^2$, $R_{side,3}^2$, $R_{long,3}^2$, and $R_{os,3}^2$ for different centralities and k_T ranges. It is seen that $R_{out,3}^2$ and $R_{side,3}^2$ are negative for all centralities and k_T ranges within systematics. The same sign of radii oscillation parameters were observed in the toy model [34] for the case where these oscillations are mostly originated from the

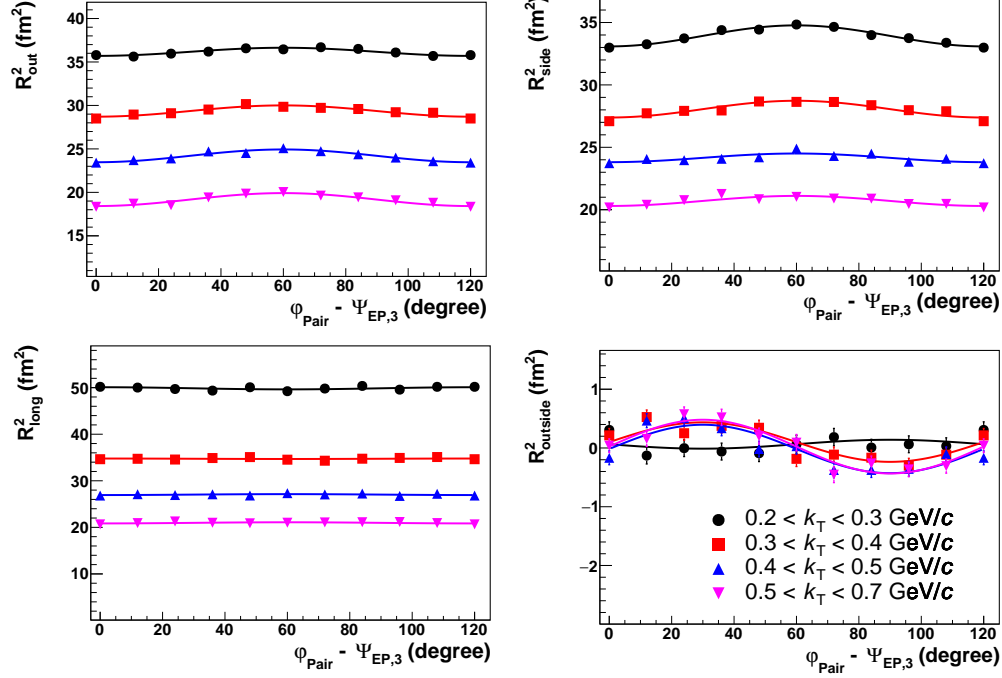


Figure 4.45: HBT radii oscillations for one centrality range in four k_T ranges.

triangular flow and not from the triangular shape of the source. $R_{\text{long},3}^2$ is consistent with zero within systematics while $R_{\text{os},3}^2$ is positive for all centralities and k_T ranges within systematics except for the k_T range 0.2–0.3 GeV/ c . All the radii oscillations exhibit small centrality and k_T dependence.

Figure 4.5.2 shows the relative amplitudes of radius oscillations $R_{\text{out},3}^2/R_{\text{side},0}^2$, $R_{\text{side},3}^2/R_{\text{side},0}^2$, and $R_{\text{os},3}^2/R_{\text{side},0}^2$. The relative amplitudes $R_{\text{out},3}^2/R_{\text{side},0}^2$ and $R_{\text{side},3}^2/R_{\text{side},0}^2$ have negative values for all centralities and k_T ranges. We compare our results with the 3+1D hydrodynamic calculations [6], where the relative amplitudes $R_{\text{side},3}^2/R_{\text{side},0}^2$ agree quantitatively, and the relative amplitudes $R_{\text{out},3}^2/R_{\text{side},0}^2$ and $R_{\text{os},2}^2/R_{\text{side},0}^2$ agree qualitatively with the 3+1D hydrodynamical calculations [6]. The relative amplitudes of the third harmonic results exhibit weak centrality and k_T dependence. According to the 3+1D hydrodynamical calculations, the negative signs of $R_{\text{side},3}^2$ and $R_{\text{out},3}^2$ parameters are an indication that the initial triangularity has been washed-out or even reversed due to the triangular flow.

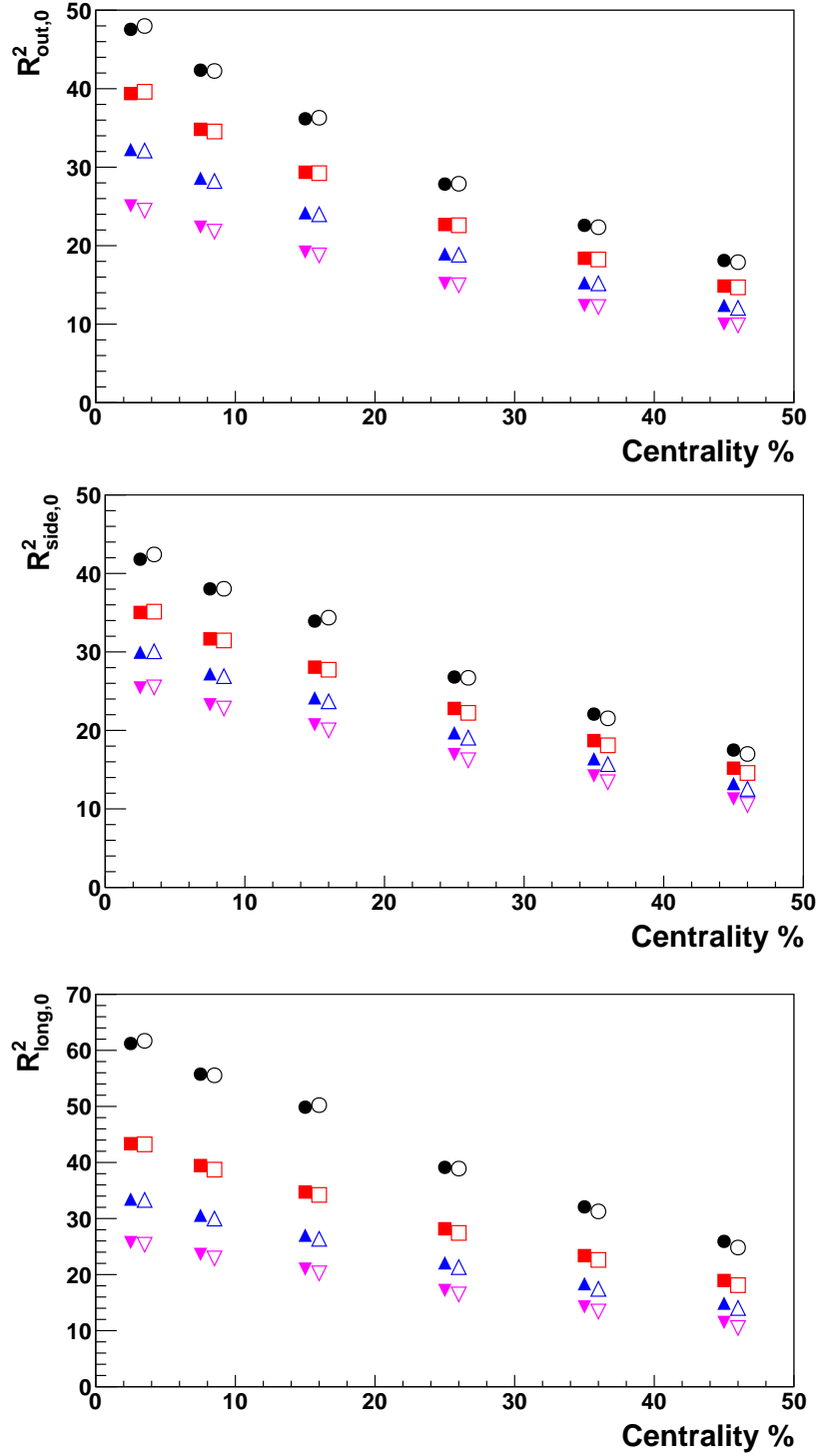


Figure 4.46: Average radii R_0^2 for four k_T ranges: $0.2 < k_T < 0.3$ GeV/c (black markers), $0.3 < k_T < 0.4$ GeV/c (red markers), $0.4 < k_T < 0.5$ GeV/c (blue markers), $0.5 < k_T < 0.7$ GeV/c (magenta markers). Closed symbols for third harmonic event plane results while the open symbols are for second harmonic event plane results.

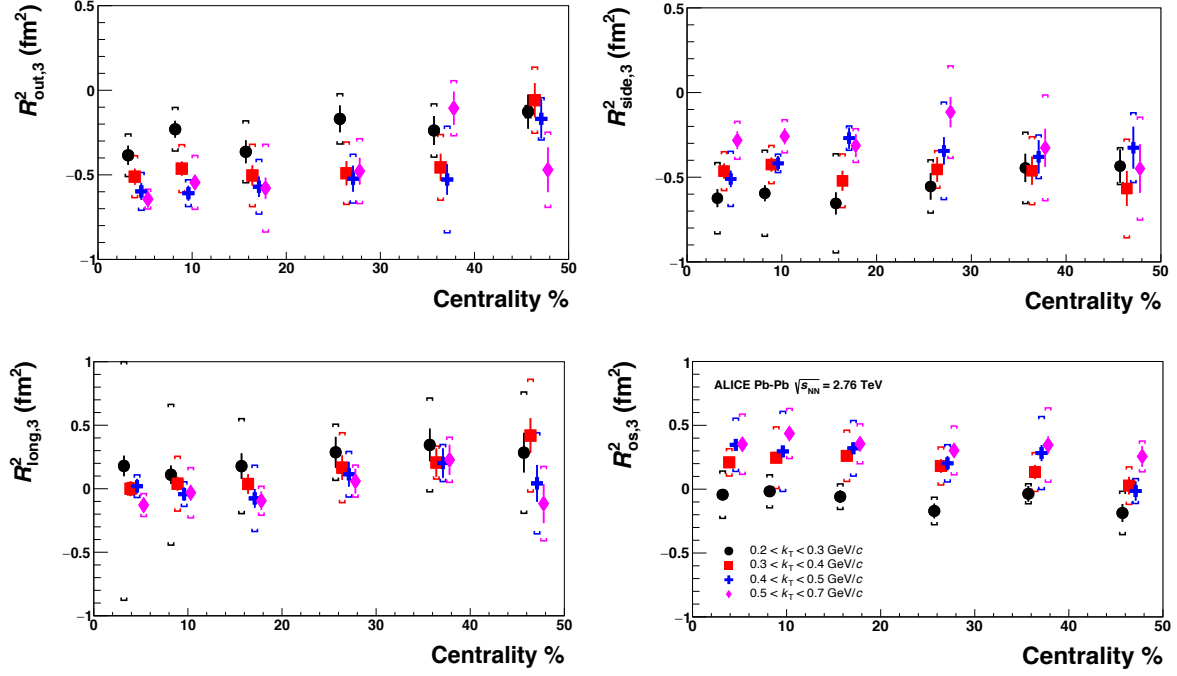
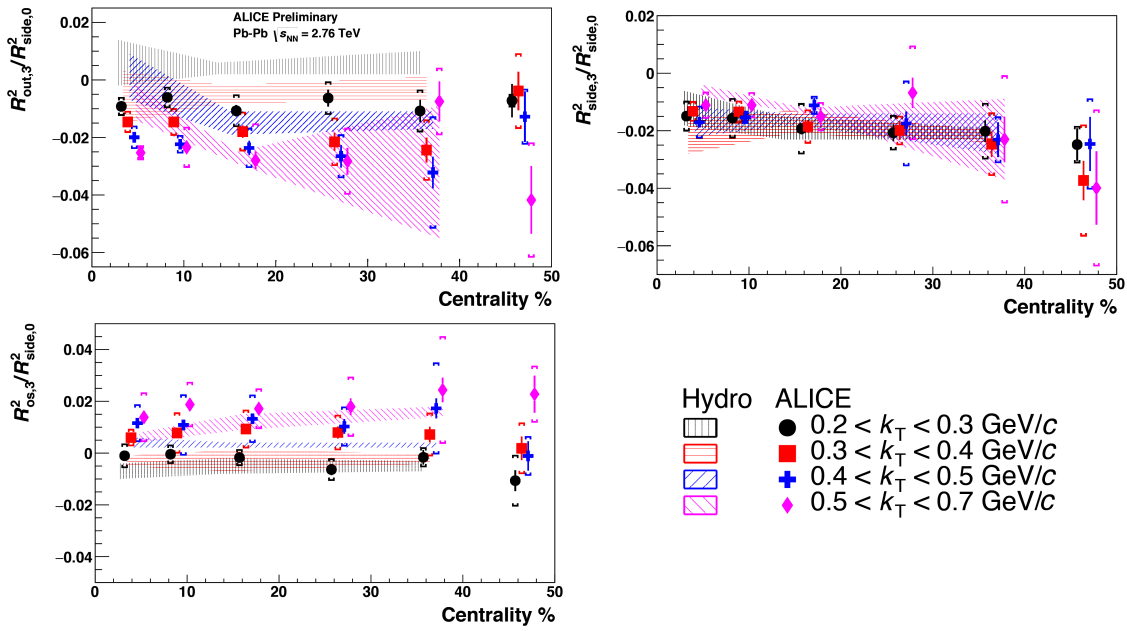


Figure 4.47: The amplitudes of radii oscillations $R_{out,3}^2$, $R_{side,3}^2$, $R_{long,3}^2$, and $R_{os,3}^2$ versus centrality for four k_T ranges. Square brackets indicate systematic errors.



[Ampli-
tudes of the relative radii oscillations $R_{out,3}^2/R_{side,0}^2$, $R_{side,3}^2/R_{side,0}^2$, and $R_{os,3}^2/R_{side,0}^2$ versus centrality for four k_T ranges. The shaded bands are the 3+1D hydrodynamical calculations and the width of the bands represent the uncertainties in the model calcula-

tions. Square brackets indicate systematic errors.]Amplitudes of the relative radii oscillations $R_{\text{out},3}^2/R_{\text{side},0}^2$, $R_{\text{side},3}^2/R_{\text{side},0}^2$, and $R_{\text{os},2}^2/R_{\text{side},0}^2$ versus centrality for four k_T ranges. The shaded bands are the 3+1D hydrodynamical calculations and the width of the bands represent the uncertainties in the model calculations. Square brackets indicate systematic errors.

4.4.5 Final Source Shape from Blast-Wave Model

To investigate more on the final source shape, we compare our results with the Blast-Wave model [10]. In this model, the spatial anisotropy of the pion source at freeze-out is parameterized by $R(\theta)$.

$$R(\theta) = R_0 \left(1 - \sum_{n=2}^{\infty} a_n \cos(n(\theta - \theta_n)) \right), \quad (4.20)$$

where θ_n 's denote the orientations of the n -th order event planes. The amplitudes a_n and the phases θ_n are model parameters [10]. The magnitude of the transverse velocity $(\rho)_{\text{profile}}$ is parametrized as:

$$\rho\left(\frac{r}{R(\theta)}, \theta_b\right) = \frac{r}{R(\theta)} \rho_0 \left(1 + \sum_{n=2}^{\infty} 2\rho_n \cos(n(\theta_b - \theta_n)) \right). \quad (4.21)$$

The results of this model used below were obtained assuming freeze-out temperature of 100 MeV, and maximum expansion velocity $\rho_0 = 0.8$, tuned to describe single particle spectra. Figure 4.48 shows the relative amplitudes of the radius oscillations $R_{\text{out},3}^2/R_{\text{out},0}^2$, and $R_{\text{side},3}^2/R_{\text{side},0}^2$ dependence on third-order anisotropies in space (a_3) and transverse flow (ρ_3). The Blast-Wave model calculations were done for pairs with $k_T = 0.6$ GeV and for the centrality range 5–10%. Dashed lines show the ALICE data for $R_{\text{out},3}^2/R_{\text{out},0}^2$ and $R_{\text{side},3}^2/R_{\text{side},0}^2$; the thickness of the lines indicate the uncertainties. The intersection of the two dashed lines indicate a_3 and ρ_3 parameters consistent with ALICE measurements. Figure 4.49 shows the final source anisotropy and transverse flow for different centrality ranges from matching the ALICE data with the Blast-Wave model calculations [10]. It shows that

the final source anisotropy is close to zero and may even become negative in some centrality ranges (30–40%, 40–50%). The negative values of the final source anisotropy would be then interpreted as that the triangular orientation at the initial state is reversed at freeze out.

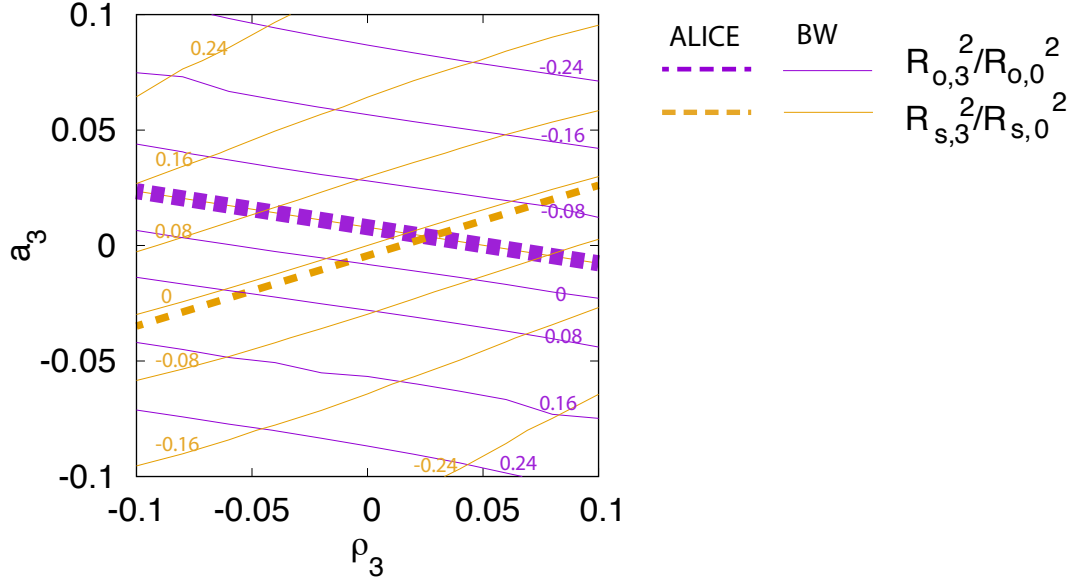


Figure 4.48: The relative amplitudes of the radius oscillations $R_{\text{out},3}^2/R_{\text{out},0}^2$, and $R_{\text{side},3}^2/R_{\text{side},0}^2$ dependence on third-order anisotropies in space (a_3) and transverse flow (ρ_3) for the centrality range 5–10% and $k_T = 0.6$ GeV from the Blast-Wave model [10]. The dashed lines are the ALICE data.

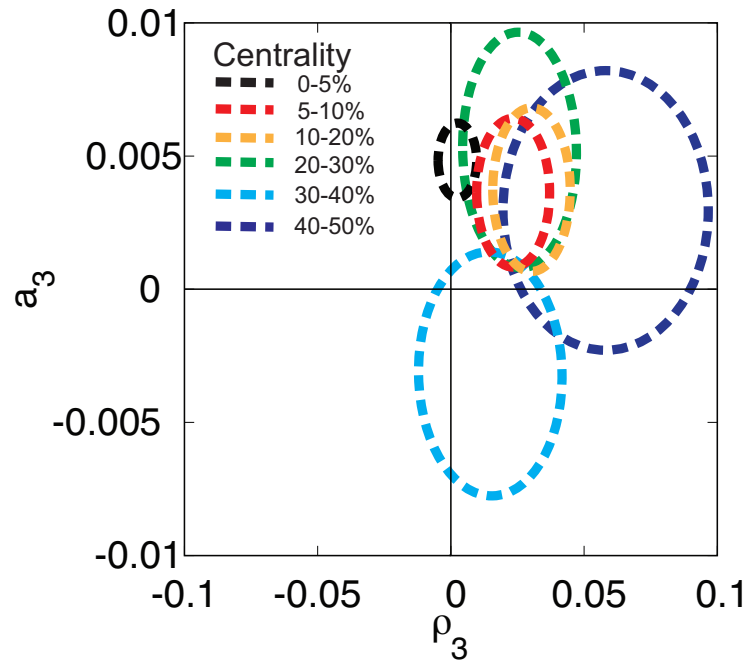


Figure 4.49: The predicted final source anisotropy a_3 and transverse flow (ρ_3) for different centrality ranges using the Blast-Wave model [10].

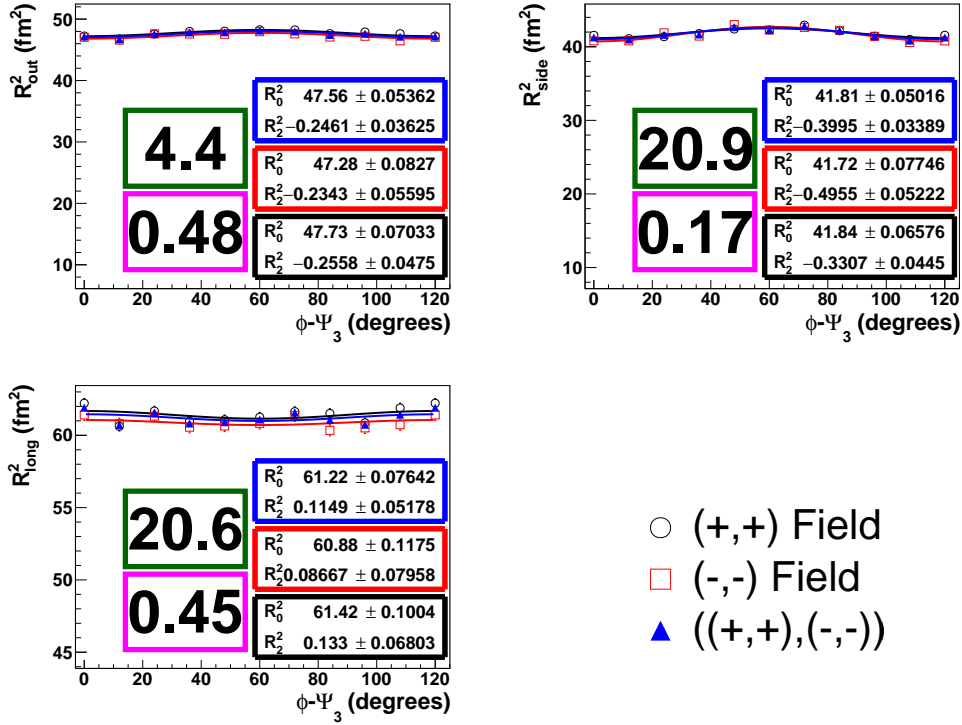


Figure 4.50: Systematic study for different field orientation data set. The green box represents the systematic percentage on the radii oscillation parameter while the magenta box represents the systematic percentage on the average radii parameter. Those results are for centrality class 0–5% and k_T range $0.2 < k_T < 0.3$ GeV/ c .

4.4.6 Systematic Studies

We did check for the systematic uncertainty coming from different pair cuts, magnetic field orientation, pair charges, detector used for event plane determination, and the fit ranges. Pair cuts studies have been reported in details in previous sections. We will present the systematic studies for magnetic field orientation, pair charges, event plane, and fit ranges.

4.4.6.1 \vec{B} orientation

Figure 4.50 shows the radii oscillation for the two field orientation (positive and negative) dataset. The systematic percentages were calculated from the average deviation of the two data sets from the combined results.

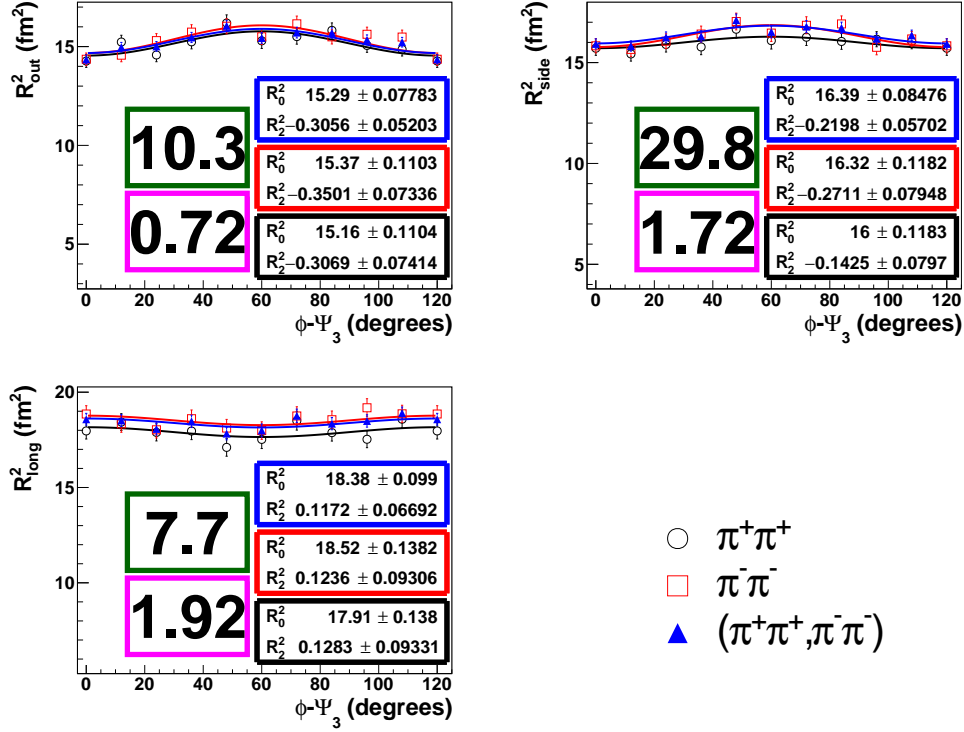


Figure 4.51: Systematic study for different pion pair charges. The green box represents the systematic percentage on the radii oscillation parameter while the magenta box represents the systematic percentage on the average radii parameter.

4.4.6.2 Charge

We analyzed positive and negative pions separately. The difference in the two results was included in the systematic uncertainty. Figure 4.51 shows an example of the difference in the results for centrality 30–40% and $0.4 \text{ GeV}/c < k_T < 0.5 \text{ GeV}/c$ results.

4.4.6.3 Fit range

For different centralities and k_T bins, we used different q -fit ranges because the radii oscillation will saturate at different q -fit ranges. A systematic study was done and included in the systematic errors. As an example, figure 4.52 shows three different q -fit ranges: 80, 100, and 120 MeV/c . Starting from 100 MeV/c , it is clear that we have a saturation. For higher centrality percentile the saturation will start from higher q -fit ranges as the Gaussian correlation function will be wider.

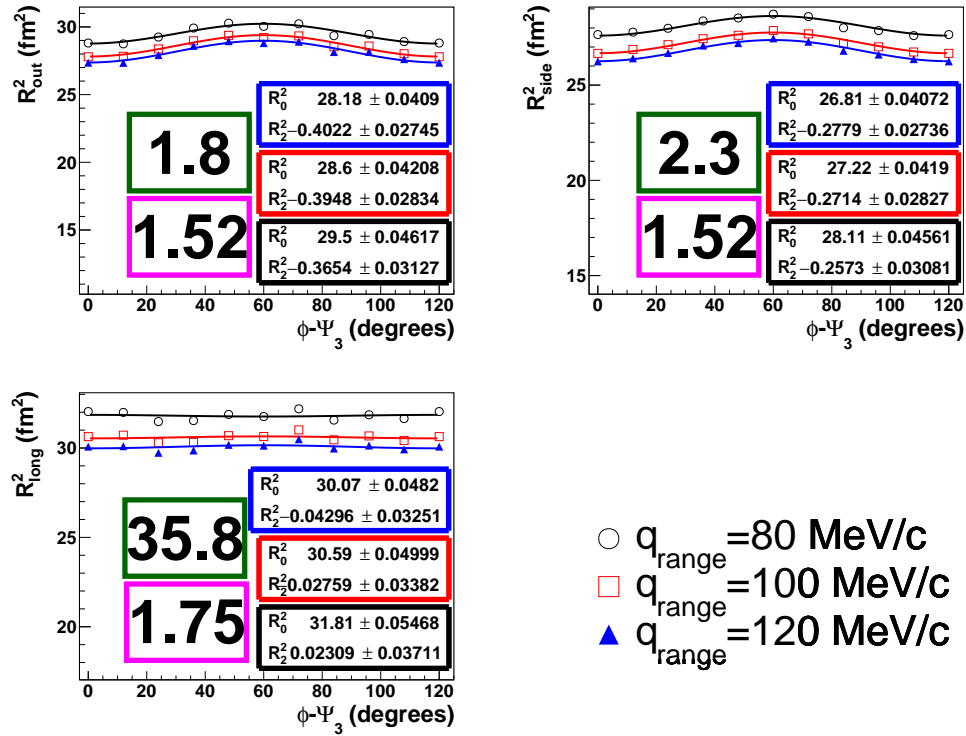


Figure 4.52: Systematic study for different fit ranges. The green box represents the systematic percentage on the radii oscillation parameter while the magenta box represents the systematic percentage on the average radii parameter.

4.4.6.4 Event plane

We used TPC detector for event plane determination. We also did the measurement using V0 detector for event plane determination. We will not show any plot because we did apply the event plane resolution correction on the oscillation parameter only. The difference in the oscillation parameter after applying event plane resolution correction was included in the systematics.

4.4.6.5 Systematics table

Below are the three tables 4.6, 4.7, and 4.8 for all the systematics done. The numbers in the tables are in percentages. For the even plane systematic studies, only modulation parameter were considered as the average radii is not affected by the event plane systematic studies.

			0-5%			5-10%		
			Rout	Rside	Rlong	Rout	Rside	Rlong
B field	0.0	R average	0.5	0.2	0.5	0.4	0.3	0.6
		R mod	4.4	20.9	20.6	26.7	28.9	21.6
	1.0	R average	0.3	0.1	0.3	0.4	0.1	0.2
		R mod	1.1	6.1	27464.0	19.9	8.5	203.4
	2.0	R average	0.2	0.3	0.5	0.3	0.5	0.2
		R mod	6.4	4.6	361.0	6.3	5.6	175.6
	3.0	R average	0.1	0.2	0.2	0.2	0.3	0.6
		R mod	1.8	1.8	9.3	17.8	8.3	526.3
Charge	0.0	R average	0.1	0.0	0.4	0.4	0.1	0.1
		R mod	20.1	9.6	40.4	18.6	2.0	132.5
	1.0	R average	0.1	0.1	0.3	0.4	0.4	0.6
		R mod	15.5	1.2	21019.4	20.6	5.3	351.4
	2.0	R average	0.3	0.1	0.5	0.5	0.5	0.4
		R mod	4.7	27.7	153.1	2.8	17.3	107.2
	3.0	R average	0.1	0.2	0.7	0.5	0.5	0.6
		R mod	2.6	32.3	67.5	3.8	6.0	322.0
Fit Range	0.0	R average	0.4	0.4	0.5	0.5	0.5	0.5
		R mod	20.0	12.6	586.9	28.5	11.9	483.2
		R average	0.8	0.8	0.9	1.1	1.1	1.2
		R mod	4.8	4.4	99.6	3.9	3.8	360.0
	2.0	R average	1.2	1.2	1.4	1.5	1.5	1.8
		R mod	4.5	4.4	194.0	1.8	2.3	35.8
	R average	1.9	1.9	2.2	2.2	2.3	2.7	
	R mod	0.7	0.2	7.6	1.3	4.0	9.2	
Pair cuts	0.0	R average	0.6	0.2	0.4	0.7	0.3	0.7
		R mod	10.0	18.0	23.0	32.0	26.0	32.4
	1.0	R average	0.5	0.2	0.3	0.6	0.3	0.1
		R mod	10.0	5.0	11.0	7.0	21.0	54.0
	2.0	R average	0.3	0.3	0.5	0.4	0.4	0.2
		R mod	12.0	8.0	83.0	9.0	11.0	90.0
3.0	R average	0.1	0.3	0.2	0.1	0.2	0.3	
	R mod	3.0	21.0	11.0	9.0	32.0	110.0	
Event Plane	0.0	R mod	12.0	11.0	18.0	15.0	13.0	21.0
	1.0	R mod	15.0	23.0	17.0	7.0	12.0	34.0
	2.0	R mod	11.0	12.0	13.0	6.0	16.0	21.0
	3.0	R mod	8.0	9.0	9.0	21.0	17.0	12.0
Total	0.2-0.3	R average	0.9	0.5	0.8	1.0	0.7	1.1
		R mod	32.7	33.7	589.4	55.9	42.7	503.0
	0.3-0.4	R average	1.0	0.8	1.1	1.4	1.2	1.4
		R mod	24.3	24.7	34584.6	30.6	26.5	546.4
	0.4-0.5	R average	1.3	1.3	1.6	1.7	1.7	1.8
		R mod	18.7	31.9	445.5	13.0	26.7	228.4
0.5-0.7	R average	1.9	1.9	2.3	2.2	2.4	2.8	
	R mod	9.1	39.6	70.0	29.2	37.9	626.9	

Table 4.6: Systematics table for centrality classes 0–5% and 5–10%.

Table 4.7: Systematics table for centrality classes 10–20% and 20–30%.

			10-20%			20-30%		
			Rout	Rside	Rlong	Rout	Rside	Rlong
B field	0.0	R average	0.7	0.5	0.8	0.2	0.6	0.3
		R mod	13.1	15.6	120.8	59.0	10.1	15.0
	1.0	R average	0.3	0.3	0.5	0.7	0.5	0.7
		R mod	28.1	12.3	46.0	16.7	2.0	85.9
	2.0	R average	0.2	0.6	0.5	0.7	0.7	0.4
		R mod	11.4	49.8	306.0	19.0	5.5	65.5
	3.0	R average	0.3	0.8	0.7	0.5	1.3	1.2
		R mod	17.0	16.5	23.1	25.5	202.0	32.8
Charge	0.0	R average	0.1	0.1	0.2	0.3	0.5	0.3
		R mod	29.6	14.4	97.2	5.0	1.9	41.5
	1.0	R average	0.4	0.3	273.0	0.4	0.4	0.2
		R mod	15.5	3.0	0.6	23.9	5.5	13.5
	2.0	R average	0.5	0.4	0.3	0.3	1.0	0.5
		R mod	15.9	61.0	74.8	2.7	18.9	99.2
	3.0	R average	0.7	0.5	0.5	0.9	1.2	1.1
		R mod	21.2	13.9	69.2	17.5	95.1	3.1
Fit Range	0.0	R average	0.3	0.9	0.3	0.5	0.4	0.4
		R mod	32.0	18.1	140.0	21.0	9.3	50.0
	1.0	R average	0.1	0.4	0.7	1.2	1.5	2.5
		R mod	9.2	11.1	70.0	15.0	6.1	134.0
	2.0	R average	0.9	1.3	1.5	1.1	1.5	1.9
		R mod	8.9	20.0	97.3	10.0	4.5	46.0
	3.0	R average	0.8	0.7	1.7	2.5	1.5	2.1
		R mod	26.5	4.1	90.0	13.0	17.0	2.2
Pair cuts	0.0	R average	0.7	0.6	0.5	0.4	0.5	0.5
		R mod	17.0	31.0	20.0	59.0	23.0	33.0
	1.0	R average	0.3	0.4	0.5	0.7	0.6	0.9
		R mod	12.0	21.0	21.0	13.0	21.0	14.0
	2.0	R average	0.3	0.6	0.6	0.6	0.7	0.7
		R mod	17.0	8.0	89.0	14.0	26.0	87.0
	3.0	R average	0.5	0.5	0.7	0.4	0.8	1.4
		R mod	11.0	13.0	21.0	19.0	76.0	54.0
Event Plane	0.0	R mod	13.0	16.0	21.0	17.0	9.0	23.0
	1.0	R mod	9.0	14.0	23.0	13.0	9.0	43.0
	2.0	R mod	7.0	18.0	32.0	10.0	8.0	32.0
	3.0	R mod	21.0	19.0	27.0	11.0	11.0	88.0
Total	0.2-0.3	R average	1.0	1.2	1.0	0.7	1.0	0.8
		R mod	50.3	44.7	210.9	87.8	28.3	77.9
	0.3-0.4	R average	0.6	0.7	273.0	1.6	1.7	2.8
		R mod	36.6	30.4	89.4	37.6	24.4	166.0
	0.4-0.5	R average	1.1	1.6	1.7	1.5	2.0	2.1
		R mod	28.3	83.6	343.0	27.6	33.9	157.6
0.5-0.7	R average	1.2	1.3	2.0	2.7	2.5	3.0	
	R mod	44.8	31.8	120.8	40.1	236.7	108.4	

			30-40%			40-50%		
			Rout	Rside	Rlong	Rout	Rside	Rlong
B field	0.0	R average	0.3	0.7	0.3	1.0	1.3	1.0
		R mod	32.0	23.2	32.1	5.8	7.9	17.6
	1.0	R average	1.1	1.3	1.1	1.3	1.6	0.6
		R mod	23.0	17.2	26.3	257.7	11.7	18.1
	2.0	R average	0.9	2.2	0.7	1.4	3.2	1.6
		R mod	13.0	23.2	5.1	60.6	62.8	114.0
	3.0	R average	0.4	3.1	1.7	1.6	4.8	4.4
		R mod	72.3	54.2	42.5	12.4	57.3	131.9
Charge	0.0	R average	0.6	0.7	0.4	1.1	1.1	0.6
		R mod	28.2	32.0	25.2	20.3	6.5	111.6
	1.0	R average	1.1	0.7	1.0	1.6	1.8	1.5
		R mod	10.1	18.7	22.5	207.5	33.9	98.6
	2.0	R average	0.7	1.7	1.9	1.1	3.0	1.8
		R mod	10.3	29.8	7.7	29.4	45.1	926.2
	3.0	R average	1.1	2.4	2.6	0.7	6.7	5.3
		R mod	120.5	62.7	35.1	39.1	11.8	191.2
Fit Range	0.0	R average	2.4	1.3	1.6	1.3	2.5	2.1
		R mod	44.0	12.0	90.0	12.0	5.0	120.0
	1.0	R average	1.2	0.7	1.1	0.8	2.3	1.3
		R mod	8.3	21.0	43.0	18.0	21.0	13.0
	2.0	R average	2.1	1.4	1.2	2.0	1.3	1.2
		R mod	54.0	32.0	67.0	15.0	8.8	32.0
	3.0	R average	1.0	0.7	1.1	2.2	2.1	1.7
		R mod	35.3	25.0	32.0	10.0	18.0	20.0
Pair cuts	0.0	R average	0.8	0.9	0.8	1.0	1.2	0.9
		R mod	16.0	19.0	34.0	6.0	13.0	9.0
	1.0	R average	1.5	1.4	1.3	1.5	1.5	1.7
		R mod	26.0	19.0	25.0	31.0	17.0	15.0
	2.0	R average	0.5	1.4	0.9	1.2	2.4	1.8
		R mod	12.0	23.0	15.0	23.0	52.0	110.0
	3.0	R average	0.5	2.3	1.5	1.2	3.2	2.1
		R mod	25.0	32.0	33.0	14.0	23.0	86.0
Event Plane	0.0	R mod	19.0	13.0	23.0	13.0	18.0	32.0
	1.0	R mod	21.0	21.0	19.0	17.0	25.0	31.0
	2.0	R mod	15.0	32.0	22.0	13.0	17.0	22.0
	3.0	R mod	43.0	25.0	32.0	16.0	17.0	33.0
Total	0.2-0.3	R average	2.6	1.8	1.9	2.2	3.3	2.6
		R mod	66.1	47.3	107.0	28.2	25.0	168.1
	0.3-0.4	R average	2.5	2.1	2.3	2.7	3.7	2.7
		R mod	42.6	43.5	63.5	333.2	51.4	106.8
	0.4-0.5	R average	2.5	3.4	2.5	2.9	5.1	3.2
		R mod	59.7	63.3	72.7	73.9	95.1	940.5
0.5-0.7	R average	1.6	4.6	3.6	3.1	9.1	7.4	
	R mod	153.2	95.6	78.6	47.3	67.6	250.7	

Table 4.8: Systematics table for centrality classes 30–40% and 40–50%.

4.5 Event Shape Engineering

Event shape engineering (ESE) is a technique proposed to select events corresponding to a particular shape. Azimuthally differential HBT combined with ESE allows for a detailed analysis of the relation between initial geometry, anisotropic flow and the deformation of source shape. In the event shape engineering analysis, events were selected based on the magnitude of the second (third) order flow vector q_2 (q_3) [57], the Forward Multiplicity detector (FMD) was used to select on the magnitude of the flow vectors ($-3.4 < \eta_{\text{FMD}} < -1.7$, $1.7 < \eta_{\text{FMD}} < 5$). We studied the effect of selecting the top 20% of the flow vector q_2 (q_3) on the magnitude of the flow v_2 (v_3). An enhancement of about 25% (15%) for v_2 (v_3) was observed for all centralities.

4.5.1 Effect of q_2 (q_3) selection on v_2 (v_3)

In order to investigate the effect of q_2 cut on v_2 , figure 4.53 shows the centrality dependence of $p_T v_2$ (top 20% q_2 cut) over v_2 (unbiased) with the charged particle ($\eta < 0.8$). boxes denotes the systematic uncertainties. v_2 is enhanced approximately 20% with q_2 cut. There is no or very small centrality dependence. v_2 is calculated with event plane method and both q vector selection and event plane is determined with FMD A+C. Event plane resolution of FMD A+C is calculated with 3-sub event method (FMD AC, TPC($-1.0 < \eta < -0.5$)) and TPC($0.5 < \eta < 1.0$)). This analysis is also applied for the third harmonic results. Figure 4.54 shows the centrality dependence of p_T integrated v_3 (top 20% q_3 cut) over v_3 (unbiased). Similar to the second order harmonic, v_3 is also 20% enhanced with large q_3 event shape cut in central collision. The v_3 ratio decreases from central to peripheral.

4.5.2 Relative Amplitude of HBT radii with Event Shape Engineering

Figure 4.55 shows the effect of large q_2 (q_3) selection on the relative amplitudes of the radii oscillations $R_{\text{out},2}^2/R_{\text{side},0}^2$ ($R_{\text{out},3}^2/R_{\text{side},0}^2$) and $R_{\text{side},2}^2/R_{\text{side},0}^2$ ($R_{\text{side},3}^2/R_{\text{side},0}^2$). The large q_2 selection significantly enhances the relative amplitudes of the radius oscillations $R_{\text{out},2}^2/R_{\text{side},0}^2$ and slightly enhanced $R_{\text{side},2}^2/R_{\text{side},0}^2$, possibly selecting more elliptic initial source. However, the large q_3 selection doesn't affect the relative amplitudes of the radius oscillations. More

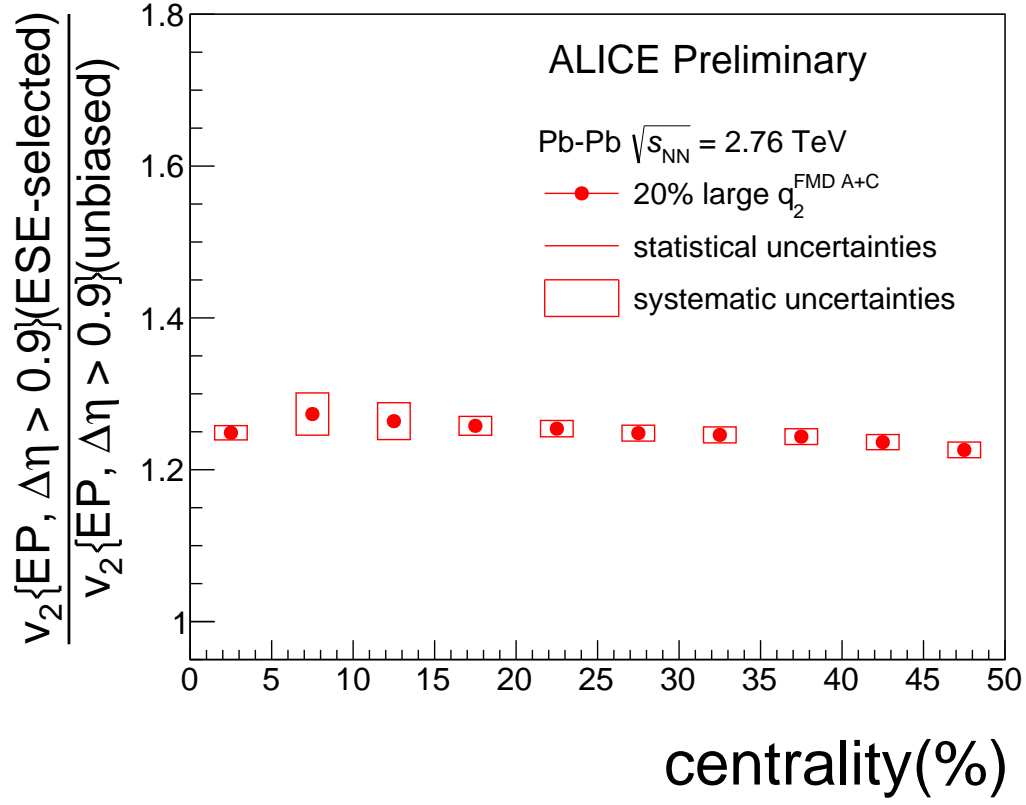


Figure 4.53: Centrality dependence of v_2 ratio

study can be done to check for low q_2 (q_3) selection on the HBT radii.

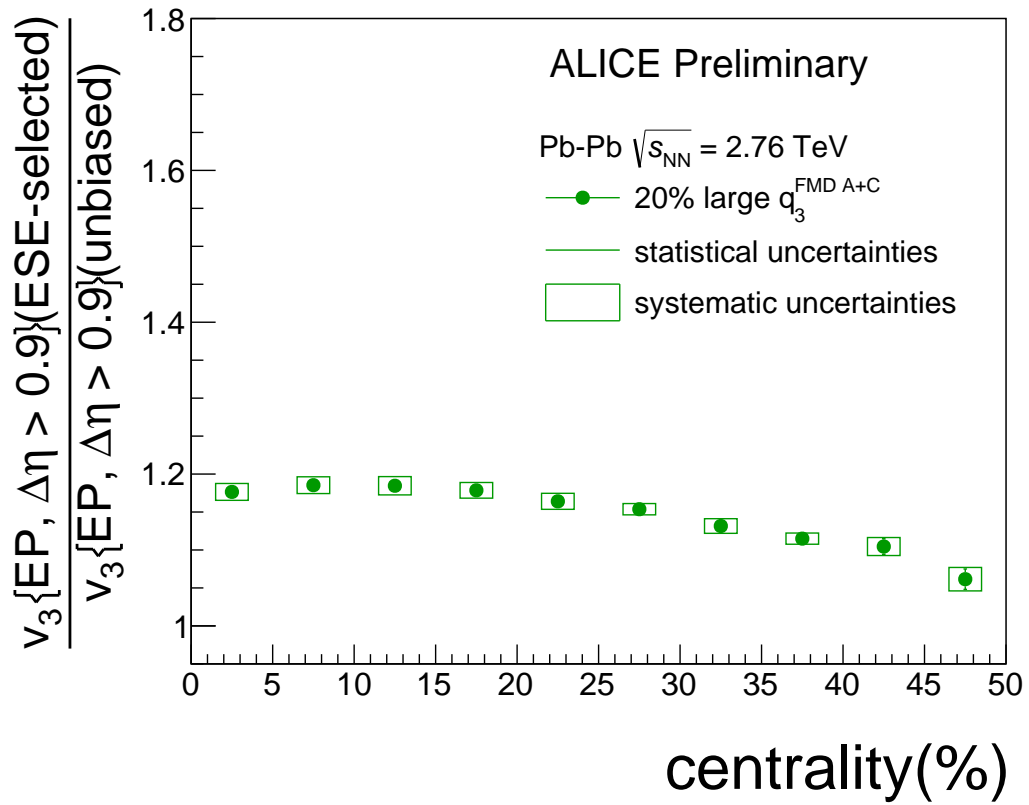


Figure 4.54: Centrality dependence of v_3 ratio

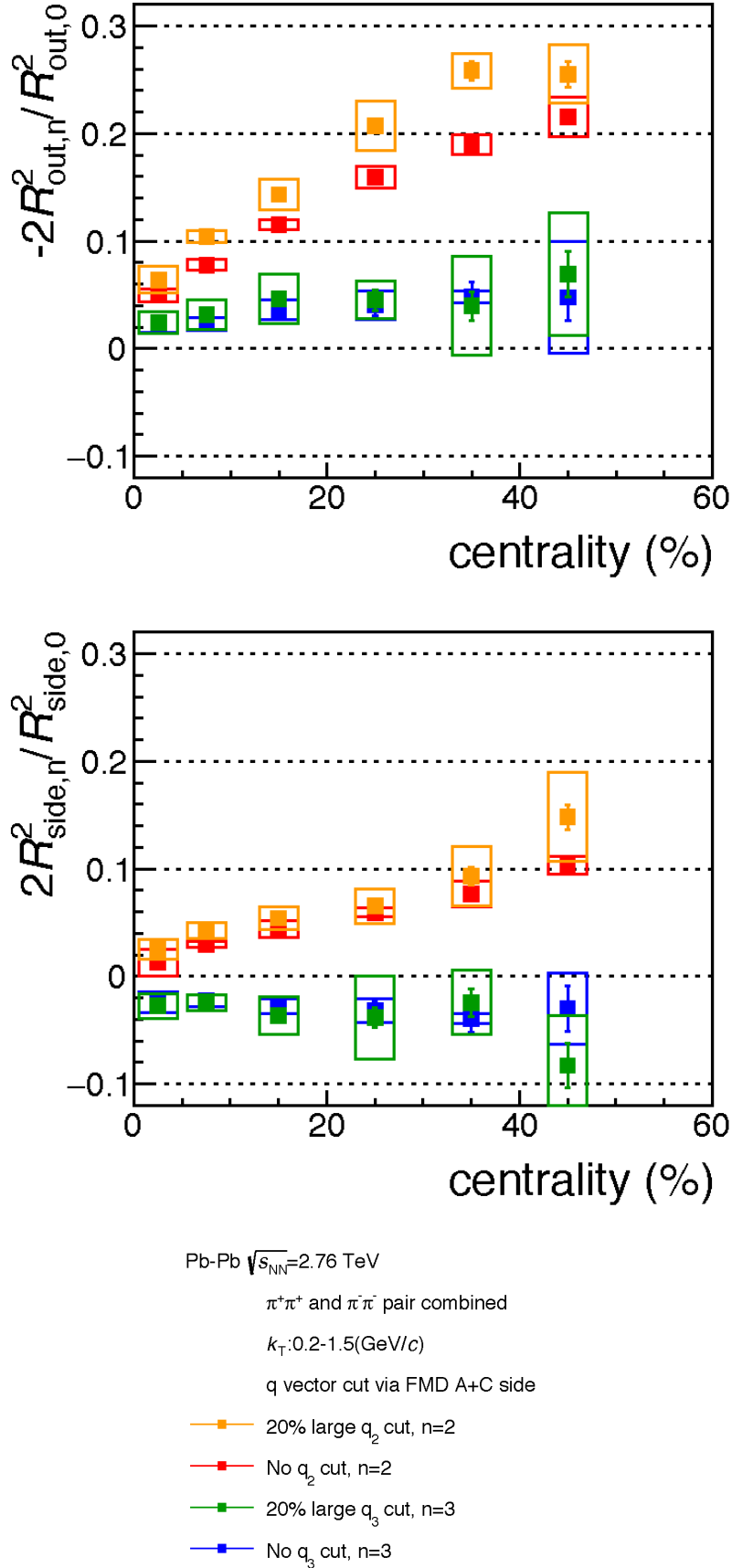


Figure 4.55: Amplitudes of the relative radius oscillations versus centrality with and without large q_2 (q_3) selection.

CHAPTER 5 CONCLUSION

In this thesis, we performed a measurement of two-pion azimuthally differential femtoscopy relative to the second and third harmonic event plane in Pb–Pb collisions at $\sqrt{s_{\text{NN}}} = 2.76$ TeV. This is the first measurement in ALICE collaboration. The measurements of the HBT radii relative to the second harmonic event plane angle (Ψ_2) provide an information on the final shape of the system, which is expected to become more spherical compared to the initial state due to stronger in-plane expansion [55]. The final-state source eccentricity, estimated via side-radius oscillations relative to the second harmonic event plane, is noticeably smaller than at lower collisions energies, but still exhibits an out-of-plane elongated source at freeze-out even after a stronger in-plane expansion. The results of these measurements have been published in the Physical Review Letters journal [55]. In addition, the results were highlighted in the CERN Courier April issue, 2017 [58]. We performed the measurements of the HBT radii relative to the second harmonic event plane angle (Ψ_2) for higher energy $\sqrt{s_{\text{NN}}} = 5.02$ TeV. The HBT radii for higher energy results didn't show any significant difference from the HBT results for Pb–Pb $\sqrt{s_{\text{NN}}} = 2.76$ TeV.

The negative signs of the relative amplitudes of radii oscillation, R_{out} and R_{side} , measured relative to the third harmonic event plane are an indication that the radii oscillations are mostly originate in the anisotropy of the velocity fields, and not from the spatial triangularity of the source. Matching the ALICE data with the Blast-Wave model calculations [10], shows the final source anisotropy is close to zero and may even become negative in some centrality ranges (30–40%, 40–50%). The negative values of the final source anisotropy would be then interpreted as that the triangular orientation at the initial state is reversed at freeze out.

The azimuthally differential HBT relative to the second and third harmonic event plane combined with ESE measurements were performed. The large q_2 selection has significant enhancement on the HBT radii relative to the second harmonic event plane, whereas large q_3 selection has no effect on the HBT radii relative to the third harmonic event plane.

BIBLIOGRAPHY

- [1] J. Alme *et al.*, “The ALICE TPC, a large 3-dimensional tracking device with fast readout for ultra-high multiplicity events,” *Nucl. Instrum. Meth.* **A622** (2010) 316–367, [arXiv:1001.1950](#) [[physics.ins-det](#)].
- [2] **ALICE** Collaboration, G. Dellacasa *et al.*, “ALICE technical design report of the inner tracking system (ITS),”.
- [3] **ALICE** Collaboration, E. Abbas *et al.*, “Performance of the ALICE VZERO system,” *JINST* **8** (2013) P10016, [arXiv:1306.3130](#) [[nucl-ex](#)].
- [4] M. A. Lisa, S. Pratt, R. Soltz, and U. Wiedemann, “Femtoscopy in relativistic heavy ion collisions,” *Ann. Rev. Nucl. Part. Sci.* **55** (2005) 357–402, [arXiv:nucl-ex/0505014](#) [[nucl-ex](#)].
- [5] V. R. Logginn, “Collective flow and azimuthally differential pion femtoscopy with the alice experiment at the lhc,”.
- [6] P. Bozek, “Azimuthally sensitive femtoscopy in event-by-event hydrodynamics,” *Phys. Rev.* **C89** (2014) 044904, [arXiv:1401.4894](#) [[nucl-th](#)].
- [7] **ALICE** Collaboration, J. Adam *et al.*, “Centrality dependence of pion freeze-out radii in Pb-Pb collisions at $\sqrt{s_{\text{NN}}} = 2.76$ TeV,” *Phys. Rev.* **C93** (2016) 024905, [arXiv:1507.06842](#) [[nucl-ex](#)].
- [8] S. Ghosh, S. K. Singh, S. Chatterjee, J. Alam, and S. Sarkar, “Initial conditions from the shadowed Glauber model for Pb + Pb collisions at $\sqrt{s_{\text{NN}}} = 2.76$ TeV,” *Phys. Rev.* **C93** (2016) 054904, [arXiv:1601.03971](#) [[nucl-th](#)].
- [9] **STAR** Collaboration, J. Adams *et al.*, “Pion interferometry in Au+Au collisions at $\sqrt{s_{\text{NN}}} = 200$ GeV,” *Phys. Rev.* **C71** (2005) 044906, [arXiv:nucl-ex/0411036](#) [[nucl-ex](#)].

- [10] J. Cimerman, B. Tomasik, M. Csanad, and S. Lokos, “Higher-order anisotropies in the Blast-Wave Model - disentangling flow and density field anisotropies,” [arXiv:1702.01735](https://arxiv.org/abs/1702.01735) [nucl-th].
- [11] U. W. Heinz, “RHIC serves the perfect fluid’: Hydrodynamic flow of the QGP,” in *Proceedings, Workshop on Extreme QCD, 2005*, pp. 3–12. 2005. [arXiv:nuc1-th/0512051](https://arxiv.org/abs/nuc1-th/0512051) [nucl-th].
- [12] L. McLerran, “The physics of the quark-gluon plasma,” *Rev. Mod. Phys.* **58** (Oct, 1986) 1021–1064. <https://link.aps.org/doi/10.1103/RevModPhys.58.1021>.
- [13] S. Collaboration, “Pion interferometry in au+au collisions at $\sqrt{s_{NN}} = 200$ GeV,” *Phys. Rev. C* **71** (Apr, 2005) 044906. <https://link.aps.org/doi/10.1103/PhysRevC.71.044906>.
- [14] F. Karsch and E. Laermann, “Thermodynamics and in medium hadron properties from lattice QCD,” [arXiv:hep-lat/0305025](https://arxiv.org/abs/hep-lat/0305025) [hep-lat].
- [15] G. H. Corral, “Relativistic heavy-ion physics,” in *High-energy physics. Proceedings, 5th CERN-Latin-American School, Recinto Quirama, Colombia, March 15-28, 2009*. 2010. [arXiv:1010.3164](https://arxiv.org/abs/1010.3164) [nucl-th]. <https://inspirehep.net/record/872952/files/arXiv:1010.3164.pdf>.
- [16] K. Werner, I. Karpenko, T. Pierog, M. Bleicher, and K. Mikhailov, “Event-by-event simulation of the three-dimensional hydrodynamic evolution from flux tube initial conditions in ultrarelativistic heavy ion collisions,” *Phys. Rev. C* **82** (Oct, 2010) 044904. <https://link.aps.org/doi/10.1103/PhysRevC.82.044904>.
- [17] I. A. Karpenko, Y. M. Sinyukov, and K. Werner, “Uniform description of bulk observables in the hydrokinetic model of $a + a$ collisions at the bnl relativistic heavy ion collider and the cern large hadron collider,” *Phys. Rev. C* **87** (Feb, 2013) 024914. <https://link.aps.org/doi/10.1103/PhysRevC.87.024914>.

- [18] P. Bozek and I. Wyskiel-Piekarska, “Particle spectra in Pb-Pb collisions at $\sqrt{s_{NN}} = 2.76\text{TeV}$,” *Phys.Rev.C* **85**(2012)064915, *arXiv* : 1203.6513[*nucl – th*].
- [19] G. Goldhaber, S. Goldhaber, W. Lee, and A. Pais, “Influence of Bose-Einstein statistics on the anti-proton proton annihilation process,” *Phys. Rev.* **120** (1960) 300–312.
- [20] G. I. Kopylov and M. I. Podgoretsky, “Correlations of identical particles emitted by highly excited nuclei,” *Sov. J. Nucl. Phys.* **15** (1972) 219–223.
- [21] G. I. Kopylov and M. I. Podgoretsky, “Multiple production and interference of particles emitted by moving sources,” *Sov. J. Nucl. Phys.* **18** (1974) 336–341.
- [22] G. Kopylov, “Like particle correlations as a tool to study the multiple production mechanism,” *Physics Letters B* **50** (1974) 472 – 474.
- [23] S. Pratt, “Pion interferometry of Quark-Gluon Plasma,” *Phys. Rev.* **D33** (1986) 1314–1327.
- [24] G. Bertsch, M. Gong, and M. Tohyama, “Pion interferometry in ultrarelativistic heavy-ion collisions,” *Phys. Rev.* **C37** (1988) 1896–1900.
- [25] **ALICE** Collaboration, K. Aamodt *et al.*, “Centrality dependence of the charged-particle multiplicity density at mid-rapidity in Pb-Pb collisions at $\sqrt{s_{NN}} = 2.76\text{ TeV}$,” *Phys. Rev. Lett.* **106** (2011) 032301, *arXiv*:1012.1657 [*nucl-ex*].
- [26] S. A. Voloshin and W. E. Cleland, “HBT analysis of anisotropic transverse flow,” *Phys. Rev.* **C53** (1996) 896–900, *arXiv*:nucl-th/9509025 [*nucl-th*].
- [27] S. A. Voloshin and W. E. Cleland, “Anisotropic transverse flow and the HBT correlation function,” *Phys. Rev.* **C54** (1996) 3212–3217, *arXiv*:nucl-th/9606033 [*nucl-th*].

- [28] **E877** Collaboration, D. Miskowiec, “Pion-pion correlations in Au + Au collisions at AGS energy,” *Nucl. Phys.* **A590** (1995) 473C–476C.
- [29] **E877** Collaboration, J. Barrette *et al.*, “Observation of anisotropic event shapes and transverse flow in Au + Au collisions at AGS energy,” *Phys. Rev. Lett.* **73** (1994) 2532–2535, arXiv:hep-ex/9405003 [hep-ex].
- [30] **E877** Collaboration, J. Barrette *et al.*, “Energy and charged particle flow in a 10.8A GeV/c Au + Au collisions,” *Phys. Rev.* **C55** (1997) 1420–1430, arXiv:nucl-ex/9610006 [nucl-ex].
- [31] **E895** Collaboration, M. A. Lisa *et al.*, “Azimuthal dependence of pion interferometry at the AGS,” *Phys. Lett.* **B496** (2000) 1–8, arXiv:nucl-ex/0007022 [nucl-ex].
- [32] M. A. Lisa, U. W. Heinz, and U. A. Wiedemann, “Tilted pion sources from azimuthally sensitive HBT interferometry,” *Phys. Lett.* **B489** (2000) 287–292, arXiv:nucl-th/0003022 [nucl-th].
- [33] S. A. Voloshin, “Femtoscopy of the system shape fluctuations in heavy ion collisions,” *J. Phys.* **G38** (2011) 124097, arXiv:1106.5830 [nucl-th].
- [34] C. J. Plumberg, C. Shen, and U. W. Heinz, “Hanbury-Brown Twiss interferometry relative to the triangular flow plane in heavy-ion collisions,” *Phys. Rev.* **C88** (2013) 044914, arXiv:1306.1485 [nucl-th].
- [35] **PHENIX** Collaboration, A. Adare *et al.*, “Azimuthal-angle dependence of charged-pion-interferometry measurements with respect to second- and third-order event planes in Au+Au collisions at $\sqrt{s_{\text{NN}}} = 200$ GeV,” *Phys. Rev. Lett.* **112** (2014) 222301, arXiv:1401.7680 [nucl-ex].
- [36] **STAR** Collaboration, L. Adamczyk *et al.*, “Beam-energy-dependent two-pion interferometry and the freeze-out eccentricity of pions measured in heavy ion collisions at the STAR detector,” *Phys. Rev.* **C92** (2015) 014904, arXiv:1403.4972 [nucl-ex].

- [37] C. Shen and U. Heinz, “Viscous Flow in Heavy-Ion Collisions from RHIC to LHC,” *Nucl. Phys.* **A904-905** (2013) 361c–364c, [arXiv:1210.2074](https://arxiv.org/abs/1210.2074) [nucl-th].
- [38] M. A. Lisa, E. Frodermann, G. Graef, M. Mitrovski, E. Mount, H. Petersen, and M. Bleicher, “Shape analysis of strongly-interacting systems: the heavy ion case,” *New J. Phys.* **13** (2011) 065006, [arXiv:1104.5267](https://arxiv.org/abs/1104.5267) [nucl-th].
- [39] **STAR** Collaboration, J. Adams *et al.*, “Azimuthally sensitive HBT in Au + Au collisions at $\sqrt{s_{NN}} = 200$ GeV,” *Phys. Rev. Lett.* **93** (2004) 012301, [arXiv:nuc1-ex/0312009](https://arxiv.org/abs/nuc1-ex/0312009) [nucl-ex].
- [40] L. Evans and P. Bryant, “Lhc machine,” *Journal of Instrumentation* **3** no. 08, (2008) S08001. <http://stacks.iop.org/1748-0221/3/i=08/a=S08001>.
- [41] **ALICE** Collaboration, K. Aamodt *et al.*, “The ALICE experiment at the CERN LHC,” *JINST* **3** (2008) S08002.
- [42] **ALICE** Collaboration, P. Cortese, “ALICE transition-radiation detector,”.
- [43] R. Brun and F. Rademakers, “Root an object oriented data analysis framework,” *Nuclear Instruments and Methods in Physics Research Section A: Accelerators, Spectrometers, Detectors and Associated Equipment* **389** no. 1, (1997) 81 – 86. <http://www.sciencedirect.com/science/article/pii/S016890029700048X>. New Computing Techniques in Physics Research V.
- [44] R. HANBURY BROWN and R. Q. TWISS, “A test of a new type of stellar interferometer on sirius,” *Nature* **178** no. 4541, (11, 1956) 1046–1048. <http://dx.doi.org/10.1038/1781046a0>.
- [45] M. Bowler, “Extended Sources, Final State Interactions and Bose-Einstein Correlations,” *Z.Phys.* **C39** (1988) 81.
- [46] Y. Sinyukov, R. Lednicky, S. Akkelin, J. Pluta, and B. Erazmus, “Coulomb corrections for interferometry analysis of expanding hadron systems,” *Phys.Lett.* **B432** (1998) 248–257.

- [47] Y. Sinyukov, R. Lednicky, S. Akkelin, J. Pluta, and B. Erazmus, “Coulomb corrections for interferometry analysis of expanding hadron systems,” *Physics Letters B* **432** no. 3, (1998) 248 – 257.
<http://www.sciencedirect.com/science/article/pii/S0370269398006534>.
- [48] **STAR** Collaboration, M. A. Lisa, “Azimuthally sensitive interferometry and the source lifetime at RHIC,” *Acta Phys. Polon.* **B35** (2004) 37–46,
[arXiv:nuc1-ex/0312012](https://arxiv.org/abs/nuc1-ex/0312012) [nuc1-ex].
- [49] A. M. Poskanzer and S. A. Voloshin, “Methods for analyzing anisotropic flow in relativistic nuclear collisions,” *Phys. Rev.* **C58** (1998) 1671–1678,
[arXiv:nuc1-ex/9805001](https://arxiv.org/abs/nuc1-ex/9805001) [nuc1-ex].
- [50] S. A. Voloshin, A. M. Poskanzer, and R. Snellings, “Collective phenomena in non-central nuclear collisions,” [arXiv:0809.2949](https://arxiv.org/abs/0809.2949) [nuc1-ex].
- [51] S. A. Voloshin, “Collective phenomena in ultra-relativistic nuclear collisions: anisotropic flow and more,” *Prog. Part. Nucl. Phys.* **67** (2012) 541–546,
[arXiv:1111.7241](https://arxiv.org/abs/1111.7241) [nuc1-ex].
- [52] F. Retiere and M. A. Lisa, “Observable implications of geometrical and dynamical aspects of freeze out in heavy ion collisions,” *Phys. Rev.* **C70** (2004) 044907,
[arXiv:nuc1-th/0312024](https://arxiv.org/abs/nuc1-th/0312024) [nuc1-th].
- [53] **PHENIX** Collaboration, A. Adare *et al.*, “Systematic study of charged-pion and kaon femtoscopy in Au + Au collisions at $\sqrt{s_{NN}} = 200$ GeV,” *Phys. Rev.* **C92** (2015) 034914, [arXiv:1504.05168](https://arxiv.org/abs/1504.05168) [nuc1-ex].
- [54] M. G. Bowler, “Bose-Einstein correlations in quark initiated jets,” *Part. World* **2** (1991) 1–6.
- [55] **ALICE** Collaboration, D. Adamova *et al.*, “Azimuthally differential pion femtoscopy in Pb-Pb collisions at $\sqrt{s_{NN}} = 2.76$ TeV,” [arXiv:1702.01612](https://arxiv.org/abs/1702.01612) [nuc1-ex].

- [56] **ALICE** Collaboration, M. Saleh, “Azimuthally differential pion femtoscopy relative to the second and third harmonic in Pb-Pb 2.76 TeV collision from ALICE,” *Nucl. Phys.* **A967** (2017) 468–471, [arXiv:1704.06206 \[hep-ex\]](#).
- [57] J. Schukraft, A. Timmins, and S. A. Voloshin, “Ultra-relativistic nuclear collisions: event shape engineering,” *Phys. Lett.* **B719** (2013) 394–398, [arXiv:1208.4563 \[nucl-ex\]](#).
- [58] **ALICE** Collaboration, M. Saleh, “CERN Courier,”
<http://cerncourier.com/cws/article/cern/68120>.
- [59] **STAR** Collaboration, J. Adams *et al.*, “Experimental and theoretical challenges in the search for the quark gluon plasma: The STAR Collaboration’s critical assessment of the evidence from RHIC collisions,” *Nucl. Phys.* **A757** (2005) 102–183, [arXiv:nucl-ex/0501009 \[nucl-ex\]](#).

ABSTRACT

**AZIMUTHALLY-DIFFERENTIAL PION FEMTOSCOPY RELATIVE
TO THE SECOND AND THIRD HARMONICS IN Pb–Pb COLLISIONS**

by

MOHAMMAD SALEH

December 2017

Advisor: Dr. Sergie Voloshin

Major: Physics

Degree: Doctor of Philosophy

Heavy-ion collisions at LHC energies create a hot and dense medium of deconfined quarks and gluons, known as the quark-gluon plasma (QGP) [59]. The QGP fireball first expands, cools and then freezes out into a collection of final-state hadrons. Correlations between the free particles carry information about the space-time extent of the emitting source, and are imprinted on the final-state spectra due to a quantum-mechanical interference effect [19]. The correlation of two identical particles at small relative momentum, commonly known as intensity, or Hanbury Brown-Twiss (HBT), interferometry, is an effective tool to study the space-time structure of the emitting source in relativistic heavy-ion collisions [24]. Due to the position-momentum correlations in particle emission, the HBT radii become sensitive to the collective velocity fields, from which information about the dynamics of the system evolution can be extracted. The spatial anisotropies in the initial state are converted, via pressure gradients and interactions between constituents, to momentum anisotropies, leading to anisotropic particle flow. Anisotropic flow is usually characterized by the Fourier decomposition of the particle azimuthal distribution and quantified by the flow harmonic strength v_n and the event plane angle (Ψ_n) [49]. Elliptic flow is defined by the second flow harmonic strength ($n = 2$), whereas triangular flow is defined by the third flow harmonic strength ($n = 3$) [49].

Azimuthally-differential femtoscopic measurements can be performed relative to the di-

rection of different harmonic event planes [26]. The harmonic event planes are determined using the event plane method [49]. The measurements of HBT radii with respect to the first harmonic (directed) flow at the AGS [31] revealed that the source was tilted relative to the beam direction [32]. In particular, measurements of the HBT radii relative to the second harmonic event plane angle (Ψ_2) provide information on the final shape of the system, which is expected to become more spherical compared to the initial state due to stronger in-plane expansion [55]. In contrast, hydrodynamics model studies have shown that the azimuthal dependence of the HBT radii relative to the third harmonic event plane angle (Ψ_3) can originate from the anisotropies in collective velocity gradients or the initial spatial anisotropy (triangular) [34]. The signs of the HBT radii relative to the third harmonic event plane angle oscillations constrain the origin of these oscillation [34].

AUTOBIOGRAPHICAL STATEMENT**MOHAMMAD SALEH:****EDUCATION:**

Bachelor of Science in Physics, Lebanese University; 2008-2011

M.S., Ph.D. in Physics, Wayne State University; 2012-2017

PUBLICATIONS:*Azimuthally Differential Pion Femtoscopy in Pb-Pb Collisions at $\sqrt{s_{\text{NN}}} = 2.76$ TeV.* Phys. Rev. Lett. 118, 222301 (2017).*Azimuthally differential pion femtoscopy relative to the second and third harmonic in PbPb 2.76 TeV collision from ALICE.*

Nuclear Physics A 967 (2017) 468471.

In the Spring of 1990, I was born to a family of three girls. In June of 2008, I received one of the highest scores in the state Baccalaureate exam. I graduated with my Bachelors of Science in Physics from the Lebanese university (Beirut, Lebanon) in 2011. After my graduation, I got married and moved to the U.S with my wife to further exceed in my education. I was admitted to Wayne State University in 2012 to continue my education. Five years later I received my M.S and PhD in Physics.